UNIVERSIDADE D
COIMBRA

Margarida Dimas Santiago

Evolution and dynamics of solar H-alpha filaments and their relation with Space Weather events

Dissertação no âmbito do Mestrado em Astrofísica e Instrumentação para o Espaço orientada pelo Doutor Ricardo Jorge Maranhas Gafeira e apresentada ao Departamento de Física da Faculdade de Ciências e Tecnologia da Universidade de Coimbra.

setembro de 2022

UNIVERSIDADE D
COIMBRA

Evolution and dynamics of solar H-alpha filaments and their relation with Space Weather events

AUTHOR: Margarida Santiago

SUPERVISOR: Dr. Ricardo Gafeira

A thesis in Astrophysics and Space Instrumentation submitted for the degree of Master of Science

FACULDADE DE CIÊNCIAS E TECNOLOGIA
UNIVERSIDADE D COIMBRA

29th September 2022

Abstract

Due to its proximity, the Sun is the only star whose atmosphere we can spatially resolve, allowing the observation of various dynamical structures driven by the interaction of magnetic field, radiation and plasma. Studying these structures is essential to better understand the physical processes in the solar atmosphere. A deeper understanding of these phenomena is essential from an astrophysical point of view, but it is of the utmost importance due to their influence on the Earth. Phenomena like coronal mass ejections (CMEs) and flares affect the Earth's environment, technological systems in space and on the ground. One of the structures we can observe at chromospheric and coronal heights are the solar filaments that strongly correlate with CMEs. They are made of cool and dense plasma sustained by magnetic fields. As of today, the actual magnetic field configuration is still under debate. This Master thesis aims to study the evolution and dynamics of solar filaments and correlate the observed behaviour with Space Weather (SW) events like CMEs and flares. We will use already published data sets of H-alpha filament data and SW events. Aspects like their morphological properties and oscillatory behaviour will be analysed, interpreted and later correlated to the identified eruptive event.

Resumo

Dada a sua proximidade, o Sol é a única estrela que nos permite ter resolução espacial suficiente da sua atmosfera para observarmos várias estruturas dinâmicas que são resultado da interação do campo magnético, radiação e plasma. Estudar estas estruturas é essencial para perceber os processos físicos que ocorrem na atmosfera solar. De um ponto de vista puramente teórico é fundamental aprofundar o conhecimento sobre estes fenómenos, mas é ainda de extrema importância tendo em conta a sua influência na Terra. Fenómenos como ejeções de massa coronal (CMEs) e erupções solares afetam o ambiente terrestre, sistemas tecnológicos no espaço e na Terra. Uma das estruturas que podemos observar à altura da cromosfera e da coroa são os filamentos solares que estão fortemente correlacionados com as CMEs. Os filamentos são constituídos por plasma denso e frio que se encontra suspenso por campos magnéticos. Atualmente, a estrutura da configuração magnética que os sustém ainda está sob debate. Esta dissertação de Mestrado tem como objetivo estudar a evolução e dinâmica de filamentos solares e correlacionar o comportamento observado com eventos de Meteorologia Espacial (SW) tais como CMEs e erupções solares. Iremos utilizar conjuntos de dados de filamentos H-alpha e eventos de Meteorologia Espacial já publicados. Aspetos como a morfologia e comportamento oscilatório dos filamentos serão analisados, interpretados e finalmente correlacionados com o evento eruptivo identificado.

Agradecimentos

Em primeiro lugar, quero agradecer ao meu orientador Dr. Ricardo Gafeira pela disponibilidade para orientar o meu trabalho, por me ter dado a conhecer este tema e por toda a ajuda e atenção que me dedicou durante este ano.

Aos meus pais, Luísa e Joaquim, e irmão, Henrique, pelo amor, apoio, e força que me deram ao longo destes anos. Muito obrigada pelas pessoas excecionais que são e por tudo o que têm feito por mim com o esforço do vosso trabalho. Obrigada, também, pelo incrível exemplo de empenho e perseverança.

Ao André, pela incrível pessoa que é, por todo o amor, paciência, motivação e apoio incondicional. Que absoluto privilégio é ter-te na minha vida.

Às minhas avós, Maria e Josefa, e aos meus avôs, Manuel e Joaquim. Às minhas tias Dida, Belinha e à madrinha Mariana, por todo o carinho e encorajamento. Aos meus tios, primos e restante família, pelas boas memórias que me têm proporcionado.

Aos meus amigos e amigas que fiz durante estes anos de faculdade, em especial, à Jéssica, Laura, Gil, Felipe, Sagar, Joana Alarcão, Marcos, Rita Roque, Mafalda, Miguel Murça, João Rocha, Alexandre, Guilherme, Miguel Ramos, Catarina Carvalho, Ivo, Toni, Luís, Diogo, Cláudia, Joana Mingacho, Catarina Carvalho (irmã da Cláudia), Gustavo, Mariana Reis, Inês Bem-Haja, Mariana Araújo, Ana Machado, Maria Martins, Disa, Afra e tantos outros, pelos inesquecíveis momentos que partilhámos, pelas conversas enriquecedoras, pelos livros emprestados e pelos filmes discutidos. Por me ensinarem a ver o mundo através dos seus olhos – e que mundo bonito que eu vi.

Aos meus amigos louletanos de longa data, Joana, João, Ana Teresa, Sofia, Sergiu, Januário, Catarina, Daniela e Marisa por todos os momentos que desfrutámos juntos e pelas pessoas incríveis que são.

Aos meus amigos da imaginada Tuna Académica de Física (TAF), Vítor,

Miguel Carvalho, Miguel Gomes, João Aveiro, Ana, Tânia, Eduardo, André Silva, Filipe, Daniel, Nuno Branco, João Oliveira, Pedro e Nuno Campos, pelo companheirismo nos bons e maus momentos, e pelo apurado sentido de humor que tantas vezes melhorou os meus dias.

A todos os meus colegas que me acompanharam e me ajudaram sempre que precisei.

A todos os meus professores e professoras, que me acompanharam em todas as fases do meu percurso académico, e que me motivaram a seguir os meus sonhos. Obrigada pela poesia, matemática, ciência, filosofia, música, literatura. Por me terem ensinado que o conhecimento e o pensamento crítico são a nossa maior arma, e, acima de tudo, um enorme prazer.

Resta-me deixar um sincero agradecimento a todas as pessoas que deixaram uma marca positiva na minha vida, e a todas as pessoas cujo trabalho diário resultou numa sociedade em que eu pudesse estudar.

Contents

Chapter 1

Introduction

> The Utopians fail to understand why anyone should be so fascinated by the dull gleam of a tiny bit of stone, when he has all the stars in the sky to look at.
>
> *Utopia*, Thomas More (1516)

The Sun is the closest star to our planet. This allows us to observe its atmosphere with a very high spatial resolution, something that is not possible in more distant stars, enabling a better understanding of all the physical processes that occur in the Sun, such as solar flares, coronal mass ejections (CMEs), filaments, sunspots, etc.

This study is interesting in itself, from an astrophysical point of view. However, another great motivation to study these phenomena is that these events emit large amounts of charged particles that are carried away and interact with Earth's magnetic field, causing many effects with practical consequences for life on Earth. The branch of physics that studies these interactions is called Space Weather (SW).

This interaction is responsible, for instance, for a well known and beautiful display of lights at high altitudes, the auroras. However, it also provides different and very serious threats to our modern world [BG10; Gos93]. To mention a few examples, it has impact on aviation, global navigation satellite systems, power grids, technological systems (both in space and on the ground), and also in the health of astronauts in the International Space Station or on other missions. Intense solar activity may, for instance, cause massive damage

on satellites and electrical transmission lines, triggering long-lasting power outages and communications failures, with huge economic impacts.

To better understand in what conditions these physical processes occur, we will focus our study on the evolution and dynamics of solar filaments, which are dense and cold structures of plasma suspended in the solar atmosphere via magnetic fields, and correlate aspects of their morphology with the occurrence of eruptive events, mainly solar flares.

In this chapter, we will provide a quick overview of solar structure, and of solar phenomena including filaments, sunspots, CMEs, and solar flares.

1.1 Solar interior

The Sun is composed of plasma, an ionized and magnetized gas, and is divided in layers with different densities and temperatures. The behaviour of the plasma and the mechanisms for energy transportation depend on the conditions of each layer, but the material is the same throughout.

Not all layers of the Sun rotate as a rigid body; this is the concept of differential rotation that is characteristic of the convection zone outwards. It also displays meridional circulation, in which the flow of plasma occurs along the meridians.

The Sun's magnetic field and its interaction with the plasma results in complex dynamics, in which the coupling between the two is extremely strong.

In Figure 1.1 we have a schematic of the layers of the Sun, from the core to the atmosphere, and of various phenomena like sunspots, granules, prominences, flares and solar wind. All these complex phenomena are consequences of the solar magnetic field. They are also observed to follow a cycle of about 11 years, the solar cycle. We will explain this in greater detail in the following pages.

Core

Starting from the inside, we find the solar core, with radius $\approx 0.2\,R_\odot$, where $R_\odot$ is the solar radius, which is the source of energy in the Sun. This is the region where energy is released in nuclear reactions, mainly in proton-proton chain reactions (Figure 1.2), causing extreme temperatures of about $15 \times 10^6\,\mathrm{K}$ and a high density of $150\,\mathrm{g/cm^3}$.

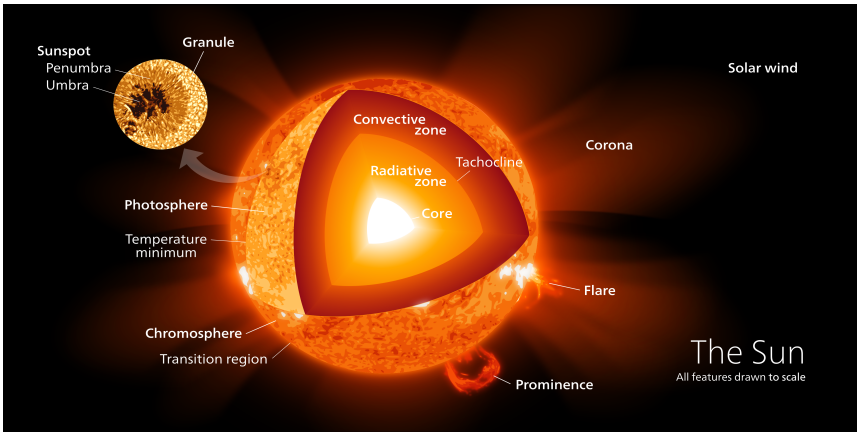

Figure 1.1: Schematic of solar structure. It is possible to see the different layers, and also several of the phenomena that take place in the Sun [Wik12].

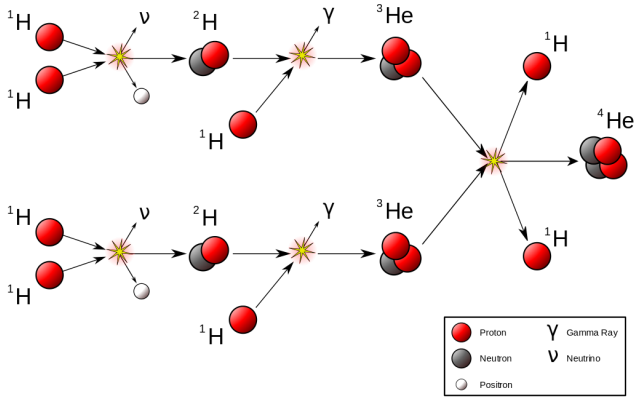

Figure 1.2: Proton-proton chain reaction [Wik16].

Radiative zone

In the radiative zone, energy is transported through radiative propagation. The photons released in the core travel through this layer, then through the convection zone, until they leave the Sun. Temperature and density are still very high in the radiative zone. For this reason, the photons' mean free path is very small, in the order of 10^{-3} m, which means that the average time for photons to leave the Sun is in the order of a hundred thousand years.

Convection Zone

In the convection zone, energy is mainly transported through convective motion of the plasma, the most efficient process in this zone. It is here that the condition for the existence of convection, the Schwarzschild criterion, is reached:

$$\nabla - \nabla_a > 0 \tag{1.1}$$

where $\nabla = \frac{\mathrm{d} \ln T}{\mathrm{d} \ln P}$, and ∇_a is the adiabatic gradient.

Note that in this layer some energy is also transported through radiative propagation, but convection is the most efficient energy transportation mechanism.

Between the radiation and convection zones exist two regions that are important to mention: the tachocline and the overshoot zone.

Tachocline and differential rotation

The tachocline (Figure 1.3) is the rotational shear layer that separates the Sun between a zone where it rotates as a rigid body – radiative zone – and where it displays differential rotation – the convection zone.

Unlike planet Earth, where every latitude rotates with the same angular velocity, the same does not happen in the convection zone in the Sun. The equator takes about 25 days to make a complete rotation. At higher latitudes, the angular velocity is progressively smaller, causing those regions to take up

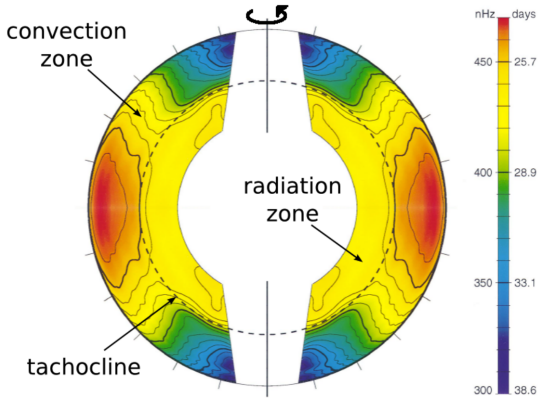

Figure 1.3: The tachocline is the interface represented by the dashed black line. Above the tachocline, the Sun has differential rotation.

to 38.6 days to complete a full rotation. The radiation zone rotates as a rigid body with a period of ≈ 27 days.

Overshoot layer

At the bottom of the convection zone, the overshoot layer (Figure 1.4) is a transition zone in which a semi-convection regime operates. In this region, some of the plasma from the convection zone enters some distance into the radiative zone due to its inertia. As the plasma is reheated, it rises again due to the buoyancy force. At the top of the convection zone, granulation and supergranulation are a consequence of the convective motions along with overshooting towards the upper layers of the atmosphere [Sti02].

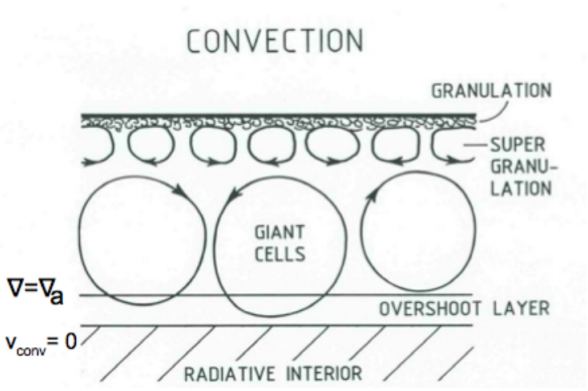

Figure 1.4: Representation of the transition zone between the radiative zone and the convection zone, where a semi-convection regime exists in the overshoot layer.

1.2 Solar atmosphere

The outer layer of the Sun is its atmosphere which consists of the photosphere, chromosphere and corona.

Photosphere

The photosphere is defined as the surface where the optical depth $\tau(r_s) = 2/3$ [Sti02]. Optical depth, τ, is described by:

$$\tau = \ln\left(\frac{\Phi_e^i}{\Phi_e^t}\right) = -\ln T \tag{1.2}$$

where Φ_e^i is the radiant flux received by the material, Φ_e^t is the radiant flux transmitted by the material and T is the transmittance of the material. The optical depth measures how far the light can penetrate into a partially transparent medium, e.g. the atmosphere of a star, before being scattered or absorbed.

The photosphere is a very thin layer with about 100 km in thickness, with an average effective temperature of $T = 5777\,\mathrm{K}$.

Overshooting also exists at the surface of the Sun. In Figure 1.5 it is possible to see the granulation patterns at the surface, which are a consequence of the convective motions underneath.

Chromosphere

The chromosphere is a relatively thin zone of ≈ 3000 to 5000 km between the photosphere and the corona, where there occurs a slight increase in temperature and an exponential decrease in plasma density (Figure 1.6). In the transition zone between the chromosphere and the next and last layer, the corona, there is a massive spike in temperature and a sharp decrease in density.

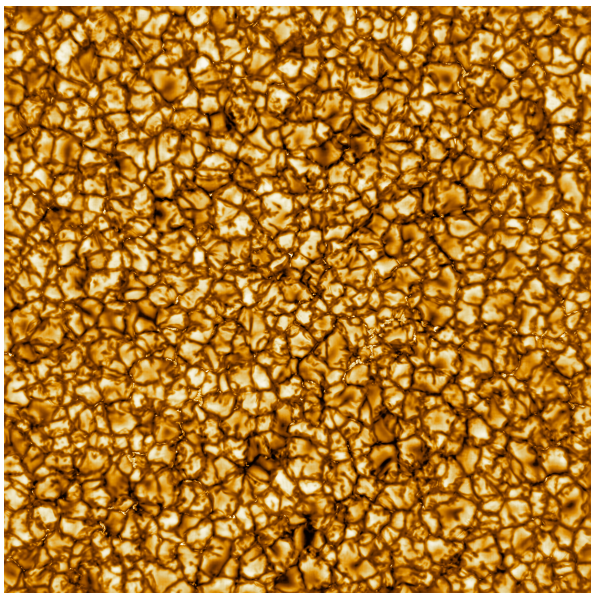

Figure 1.5: Granulation pattern in the Sun [Rim+20].

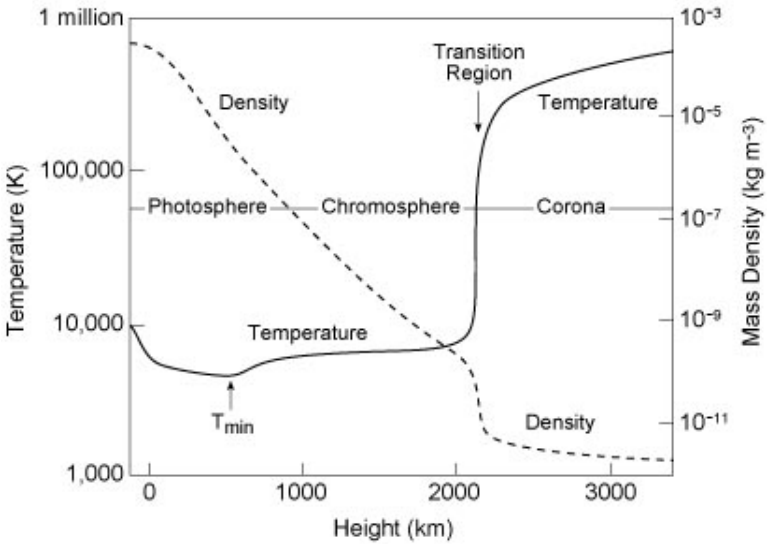

Figure 1.6: A schematic of the mean variation of temperature and density with height in the solar atmosphere according to the VAL (Vernazza-Avrett-Loeset) model [Lan10].

Corona

Finally, we reach the corona, the outer layer of the solar atmosphere. This region can extend millions of kilometres into space; in fact it does not have a well defined border since flux ropes can extend towards the interplanetary space, and by definition they still belong to the Sun. The temperature is extremely high, in the order of $T \sim 10^6\,\mathrm{K}$, but the density is very low, $\approx 10^{-12}$ times as dense as the photosphere.

Without knowing the information above, it would be sensible to assume that the chromosphere and corona would be cooler than the photosphere, since they are farther away from the centre of the Sun, but it is not the case. The energy dissipation mechanisms of magnetohydrodynamic (MHD) waves which allow for this chromospheric coronal heating are still an open problem.

Phenomena like coronal mass ejections (CMEs) and flares occur in the corona.

- **CMEs** (Figure 1.7) are eruptions of large quantities of plasma into space. The ejected material moves across the solar corona with a velocity range of 10^5 – $10^6\,\mathrm{m\,s^{-1}}$ [Sti02], and according to the same reference, CMEs contribute as much as 10% to the whole mass loss by the solar wind.

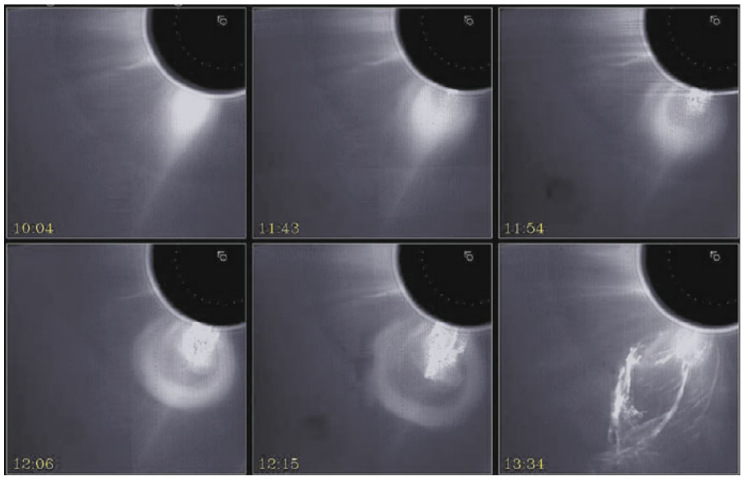

Figure 1.7: Development of a coronal mass ejection [Hig89].

- **Flares** (Figure 1.8) are very intense and sudden emissions of electromagnetic radiation, in the order of 10^{20} J. They are often accompanied by coronal mass ejections but not always. There is evidence that changes in the magnetic field occur during flares [Sti02]. In Figure 1.9, the Sweet-Parker model of the development of a solar flare is explained.

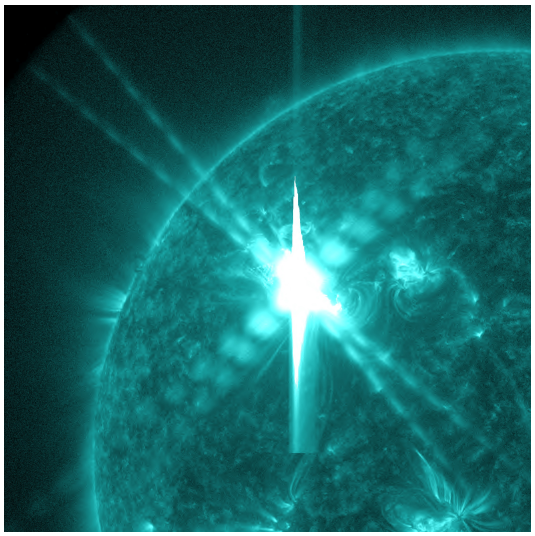

Figure 1.8: Solar flare [NAS12].

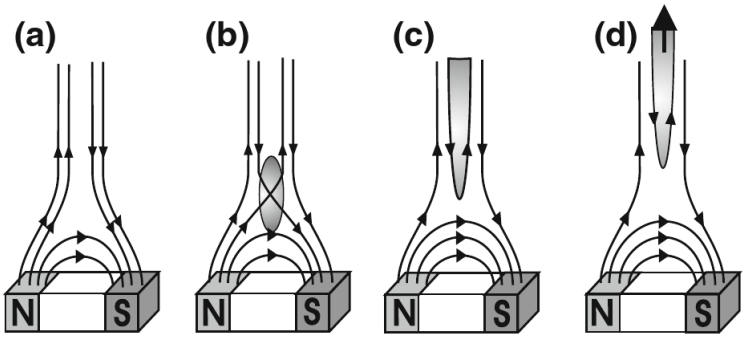

Figure 1.9: Development of a solar flare in the Sweet-Parker model: (a) the dipolar field of a coronal loop connects to the interplanetary magnetic field; (b) reconnection of the antiparallel field line causes the stress of the field to release; (c), (d) the relaxing magnetic field accelerates the trapped plasma.

Solar Cycle

The activity in the Sun, in terms of the phenomena that we can observe at the surface, such as prominences, faculae, coronal mass ejections, flares, and sunspots in the solar disk, follows a cycle of approximately 11 years.

The most common way to track this cycle is to focus on the occurrence and dynamics of sunspots.

Sunspots are dark regions on the photosphere that consist of strong concentrations of magnetic fields on the solar surface. The centre of the sunspot, the umbra, displays a very intense magnetic field, perpendicular to the surface, of 3000 G, and has a cooler temperature of $T = 4000\,\mathrm{K}$ when compared with the surrounding region, i.e. the quiet Sun (see Figure 1.10). The penumbra is the slightly brighter region surrounding the umbra with a weaker magnetic field.

The dark appearance of sunspots is due to a strong magnetic field inhibiting convection motions of the plasma; thus when observing the sunspots, we see plasma at lower temperatures, which appears darker when compared with the surrounding plasma.

Typically, sunspots are confined to an equatorial belt of latitudes between $-30°$ and $+30°$ [SIS06].

At the beginning of a new solar cycle, sunspots form at higher latitudes. As the cycle reaches a maximum (intense magnetic activity at the surface), they appear progressively closer to the equator, reaching latitudes of about $\pm 5°$.

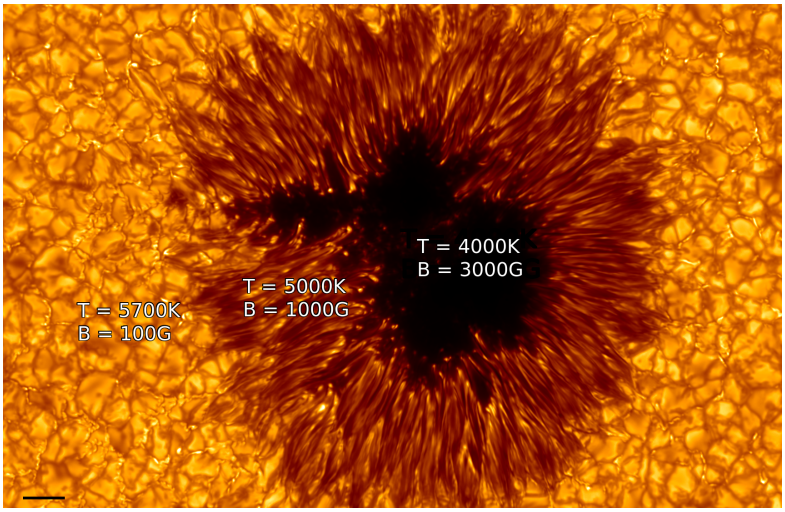

Figure 1.10: Temperature and magnetic field intensity in a sunspot's umbra, penumbra, and in the quiet sun, for comparison.

As the cycle reaches a minimum, they disappear from the lower latitudes and reappear at higher locations. This cyclic behaviour of sunspots gives rise to a "butterfly" pattern that can be seen in Figure 1.11, which was first discovered by Edward Maunder in 1904.

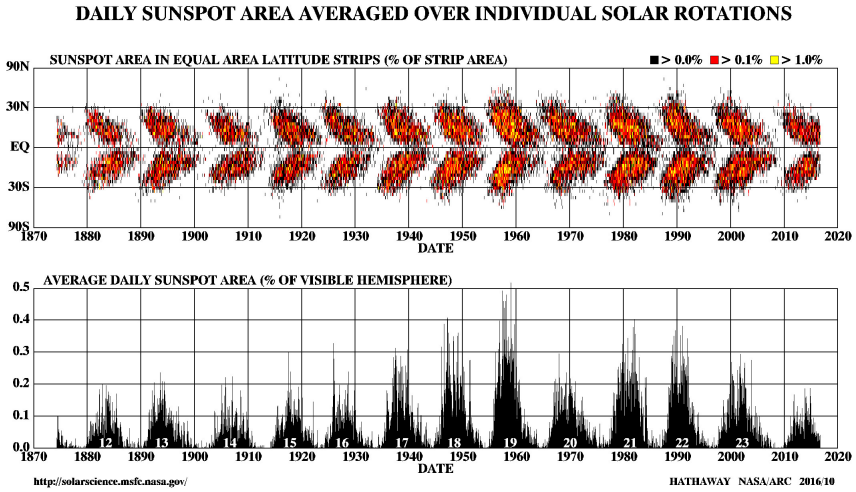

Figure 1.11: (Top) Butterfly diagram. Sunspots appear at higher latitudes and migrate towards the equator with time. (Bottom) Average daily sunspot area in % of visible hemisphere [NAS09]

In 1919, Hale et al. [Hal+19] formulated the following polarity rules, which have been confirmed by observation:

1. The magnetic polarity of the leader and follower spots, that always appears in bipolar groups, remains the same in each hemisphere over each 11-year cycle;

2. The bipolar groups in the two hemispheres have opposite magnetic orientation;

3. The magnetic polarity of bipolar groups reverses from one cycle to the next.

All the above rules can be observed in Figure 1.12.

Due to the dark appearance of sunspots, it would be reasonable to assume that at the solar maximum, when the number of sunspots is largest, there would be a reduction of the total irradiance of the Sun, but this is not observed. Sunspots are frequently associated with faculae (very bright regions in the Sun with areas much larger than sunspots). When the sunspots' magnetic field eventually decays, it gives rise to smaller scale magnetic structures, which contribute to the increase of the area of the faculae. The facular regions' brightness ends up compensating for the sunspots' darkness, causing the Sun to be the brightest when it reaches maximum activity.

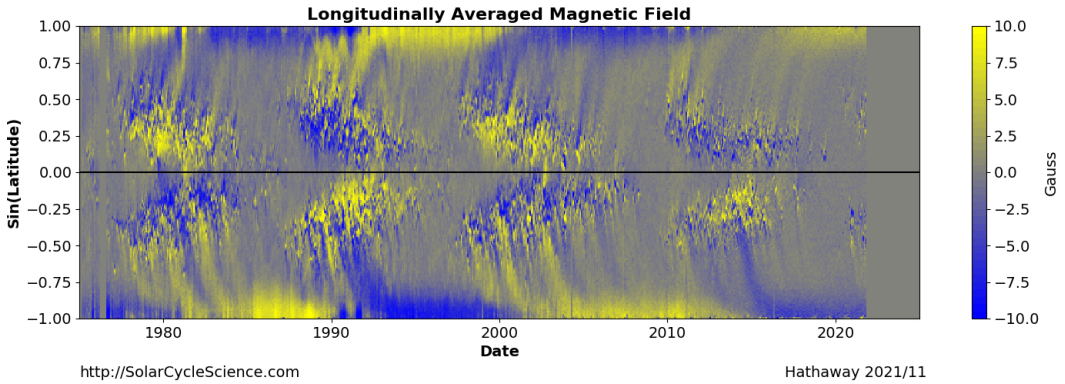

Figure 1.12: Magnetic butterfly diagram: surface magnetic field, longitudinally averaged. The poles display opposite polarities that reverse after each cycle [Hat21]

Zeeman effect on Sunspots

In 1908, Hale measured for the first time the magnetic field in sunspots. He obtained the electromagnetic spectrum of sunspots and saw that the energy levels of the atoms split into different levels (Figure 1.13). That is the imprint of Zeeman effect and proves that sunspots have an intense magnetic field.

1.3 Filaments

Basic properties

Filaments, or prominences (Figure 1.14), are structures of relatively cool ($T \sim 10^4\,\mathrm{K}$) and very dense ($10^9 - 10^{11}\ \mathrm{cm}^{-3}$) plasma that is suspended against gravity, between $10^4\,\mathrm{km}$ and $10^5\,\mathrm{km}$ above the photosphere [SIS06].

In the solar disk, it is possible to observe filaments as long dark structures, which are seen in absorption strong spectral lines using an (Hα) 656.28 nm filter (Figure 1.17). They are optically thick because of their high density, which means they absorb radiation from the surface. This is why they seem dark when observed on the solar disk.

When seen above the solar limb, filaments are called "prominences", and they appear bright in contrast with the dark outer space.

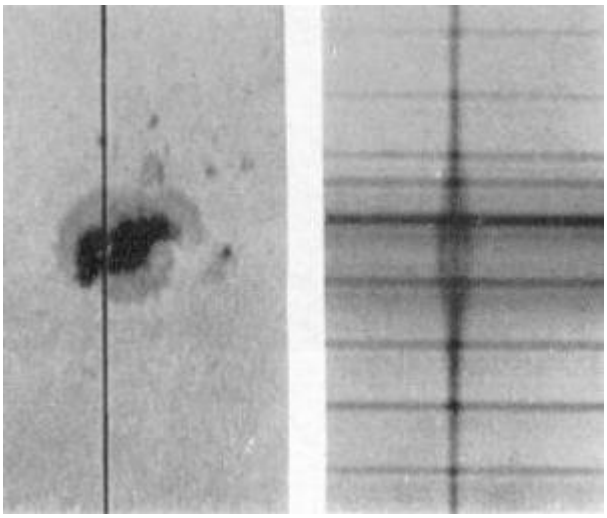

Figure 1.13: Zeeman effect caused by the intense magnetic fields of sunspots. The spectrum of the vertical black line is shown on the right. Intense magnetic field causes the splitting of the spectral lines of the line [NAS19].

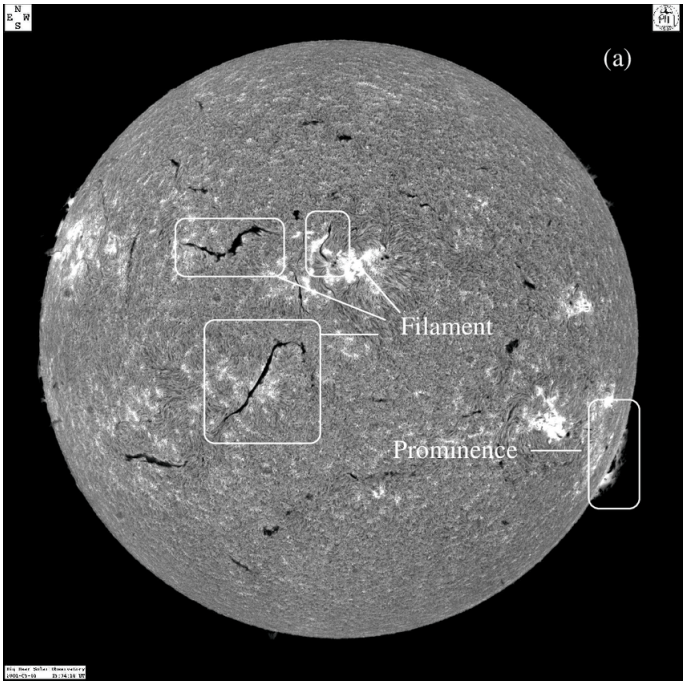

Figure 1.14: Filaments and prominences observed in Hα [BBS07].

Filaments exist directly above large scale polarity inversion lines (PILs), in the order of 10–100 Mm, which are neutral lines that separate zones in the photosphere where the radial component of the magnetic field, B_r, changes sign (Figure 1.15).

Morphologically, filaments have a spine, barbs and two legs (endings). The spine is the main component horizontally placed along the top of the filament and the barbs are lateral extensions that protrude at an acute angle from the filament. Barbs can have a right or left inclination, which in most cases is related to whether the filament is dextral or sinistral, respectively [Mar98]. An example can be seen in Figure 1.16.

The direction of the barbs generally allows us to guess the magnetic helicity of the filament. To avoid subjective judgements, since filaments also have abnormal barbs (which do not align as expected), Pevtsov, Balasubramaniam and Rogers [PBR03] suggested computing a fractional chirality as a weighted difference between normal and anomalous barbs.

Pevtsov, Balasubramaniam and Rogers [PBR03] also observed that the majority of filaments' chirality in the Northern hemisphere is dextral while in the Southern hemisphere is sinistral, which is in accordance with the fact

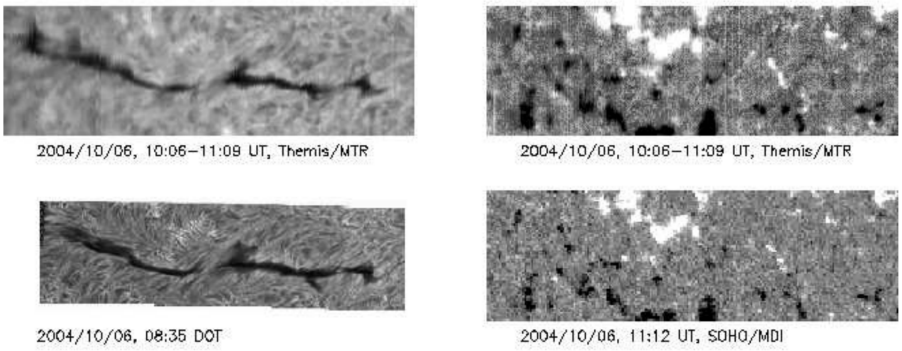

Figure 1.15: Hα filament observed on the 6th of October 2004 from Dudík et al. [Dud+08]. On the left the filament and on the right the magnetograms. It is possible to see how filaments are located in zones where the radial component of the magnetic field, B_r, changes sign. Both magnetograms saturate at ± 40 G. The white/black regions in the magnetogams correspond to positive/negative B_r, respectively

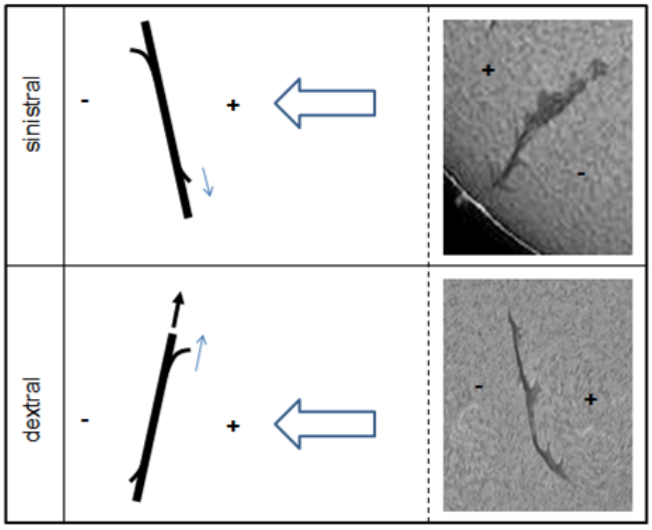

Figure 1.16: Dextral/sinistral filaments with right/left oriented barbs [GON13].

the solar magnetic fields have negative magnetic helicity in the north and positive helicity in the south. This hemispheric helicity rule is also followed by large-scale magnetic fields.

Filaments can also be classified according to the region of the Sun where they exist [VE15].

- Active region (AR) filaments exist in low latitudes, coinciding with regions of very intense magnetic activity, associated with sunspots and plages. In Figure 1.18, it is possible to see bundles of thin threads horizontally aligned with respect to each other. Together, the groups can show up-ward or down-ward curvature. These plasma flows have horizontal velocities of $10\,\mathrm{km\,s^{-1}}$ [Oka+07] and perpendicular flows, possibly associated with eruptive motions, of $70\,\mathrm{km\,s^{-1}}$ [KTd03].

- Intermediate (IT) filaments form between active regions and decaying unipolar plages [Mac+10]. These structures are more stable and larger than AR filaments. IT filaments have a decay time in the order of a few days, while time spawns in-between eruptions in AR filaments of a few hours [Ber13].

- Quiescent (QS) originate far from active zones, in the quiet sun, which grants them higher stability; their life time is usually of a few weeks. They are usually found at high latitudes $> 50°$ and are the tallest since they can extend 35 Mm over the limb.

Previous observation has shown up-flow velocities of plasma in the thin threads of about $20\,\mathrm{km\,s^{-1}}$ while the down-flow velocities were about $10\,\mathrm{km\,s^{-1}}$

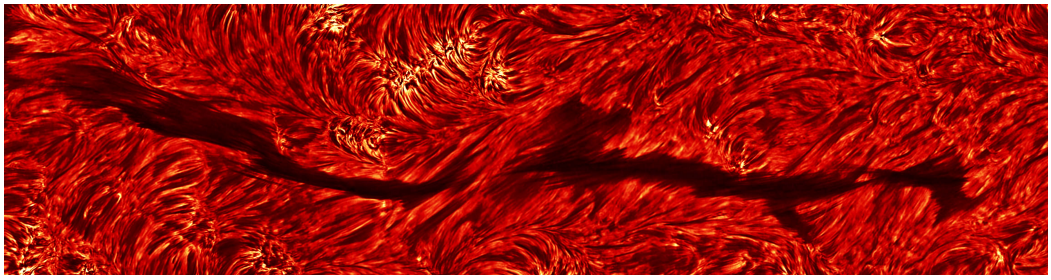

Figure 1.17: Hα image with a clear view of the filament's spine, two barbs and fibrils aligned with the sheared magnetic field in respect to the spine long axis [Par14]

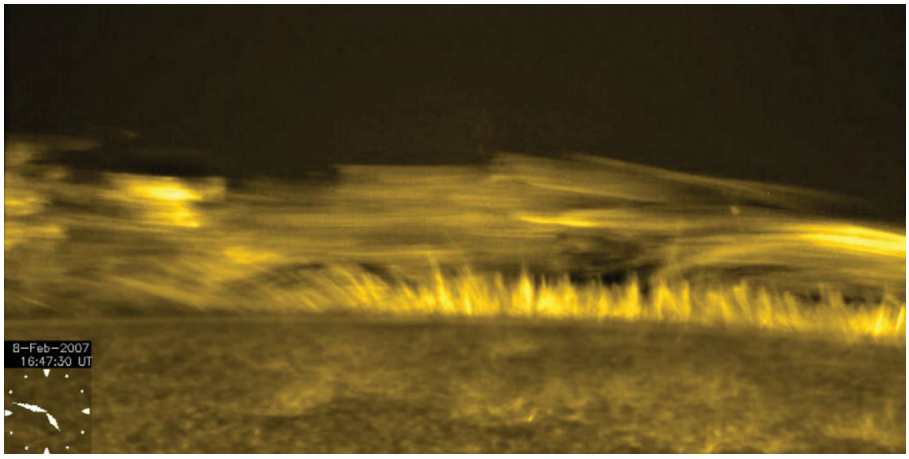

Figure 1.18: Active region prominence seen against the limb. Bundles of thin threads with lengths 5–30 Mm and thickness of 350–650 km [Oka+07].

[Mac+10]. The fact that plasma from these threads does not display free-fall indicates that filaments are being supported against gravity through some mechanism [PE00].

To understand how the filaments are formed and suspended in the solar atmosphere we will start with the equation of energy for the optically thin corona [Pri14]:

$$\frac{\rho^\gamma}{\gamma - 1} \frac{\mathrm{d}\left(\frac{p}{\rho^\gamma}\right)}{\mathrm{d}t} = -\nabla(k \cdot \nabla T) - \rho^2 Q(T) + \frac{j^2}{\sigma} + h\rho \tag{1.3}$$

with γ being the adiabatic index, ρ the plasma density, p the hydrostatic pressure, k the thermal conductivity coefficient, $Q(T)$ the optically thin radiative loss function, j the electric current, σ the electrical conductivity and h the coronal heating rate per unit mass.

Equation 1.3 describes how the changes in entropy on the plasma are caused by thermal conduction, optically thin radiation, ohmic heating and a small-scale heating term proportional to density.

In the corona, the optically thin radiative function has this form (with $\chi = 10^{-32}$):

$$Q(T) = \chi T^{-1/2} \ \mathrm{W\,m^3} \tag{1.4}$$

which is valid for the part of the atmosphere where $2 \times 10^4 < T < 10^7$ K, but in the further discussion we will assume this function to be constant for simplicity.

Let us consider hot coronal plasma with temperature T_0 and density ρ_0 under an equilibrium between radiation ($\tilde{Q}^2\rho^2 = Q^2 n_e$) and heating $H\rho$ per unit volume described by:

$$0 = Q\rho_0^2 - H\rho_0 \tag{1.5}$$

Consider now equilibrium at constant pressure, which holds because the time-scale of the perturbations is greater than the speed of sound, with some perturbations:

$$C_P \frac{\partial T}{\partial t} = H - \rho\tilde{Q} + \frac{k_\parallel}{\rho}\frac{\partial^2 T}{\partial s^2} \tag{1.6}$$

where the last term is the effect of heat conduction at a distance s along the magnetic field, and the parallel subscript of k refers to the value of k along the magnetic field.

We now introduce the variations $T = T_0 + T_1$ and $\rho = \rho_0 + \rho_1$. Assuming as well an ideal gas

$$\rho = \frac{mp}{k_B T} \tag{1.7}$$

we reach:

$$C_P \frac{\partial T_1}{\partial t} = \frac{\rho_0 \tilde{Q} T_1}{T_0} + \frac{k_\parallel}{\rho_0}\frac{\partial^2 T_1}{\partial s^2} \tag{1.8}$$

Assuming that the perturbations disappear at the end of the coronal loop of length L, and that T_1 is proportional to $e^{wt+2\pi i\frac{s}{L}}$, this guarantees that the temperature at the ends of the filament is equal to that of the corona. This gives the growth rate:

$$w = \frac{\rho_0 Q}{T_0 C_P} - \frac{k}{\rho_0}\frac{4\pi^2}{L^2 C_P} \tag{1.9}$$

In the absence of conduction (where $w > 0$), plasma is thermally unstable, and this allows us to calculate the maximum length of the filament before the plasma in it loses its thermal stability:

$$L < L_m \equiv 2\pi\left[\frac{k_\parallel T_0}{Q\rho_0^2}\right]^{1/2} \tag{1.10}$$

If L_m is exceeded, the plasma will no longer be thermally stable and will cool down until a new equilibrium is reached. This is the basis of prominence-like condensation.

Now we will see how the filament exists under equilibrium of different forces. Let us begin with the MHD induction equation:

$$\frac{\partial \vec{B}}{\partial t} = \underbrace{\boldsymbol{\nabla} \times (\vec{v} \times \vec{B})}_{\text{advection}} + \underbrace{\eta \nabla^2 \vec{B}}_{\text{diffusion}} \tag{1.11}$$

where $\vec{v}$ is a velocity field, $\eta = \frac{1}{\mu\sigma}$ is the magnetic diffusivity, μ is the permeability, and σ is the conductivity. The first term of Equation 1.11 describes the inducing effect of the material motion upon the magnetic field, while the second term describes the diffusion process of the magnetic field, due to the diffusivity of the plasma. If we consider the ratio between time scale where advection dominates, $\tau_{\text{ad}} = l/v$, and the time scale where diffusion dominates, $\tau_\sigma = l^2/\eta$, we obtain the magnetic Reynolds number

$$R_m \equiv \frac{\tau_{\text{ad}}}{\tau_\sigma} = vl/\eta \tag{1.12}$$

where l and v are the characteristic length and velocity scales of the system.

- If $R_m \gg 1$ advection dominates and the magnetic field is "frozen" (moves) to (with) the plasma.
- If $R_m \ll 1$ then the diffusion will dictate the evolution of the magnetic field.

The Lorentz force is:

$$\vec{j} \times \vec{B} = \frac{(\vec{B} \cdot \nabla)\vec{B}}{\mu} - \nabla\left(\frac{B^2}{2\mu}\right) \tag{1.13}$$

where the first term is the magnetic tension force and the second term represents the force created due to magnetic pressure.

We can relate the hydrostatic pressure and the magnetic pressure using the parameter β, which is defined as:

$$\beta \equiv \frac{p}{\vec{B}^2/(2\mu)} \tag{1.14}$$

If $\beta \gg 1$, then the hydrostatic pressure dominates, while if $\beta \ll 1$, then the magnetic pressure dominates.

Another MHD equation is the equation of motion,

$$\rho\frac{\mathrm{d}v}{\mathrm{d}t} = -\nabla p + \vec{j} \times \vec{B} + \rho\vec{g} \tag{1.15}$$

which describes how the pressure gradient, magnetic field, and gravity govern the motion of the plasma. As mentioned before, filaments exist in a complex equilibrium under the effect of the mentioned forces.

The left-hand side of Equation 1.15 is negligible in the case where plasma flow speed is much smaller than the speed of sound, $v_s = \left(\frac{\gamma p}{\rho}\right)^{1/2}$, the Alfvén speed, $v_A = \frac{B}{(\mu\rho)^(1/2)}$, and the free-fall speed, $(2gL)^{1/2}$.

Therefore, in this situation, Equation 1.15 becomes:

$$0 = -\nabla p + \vec{j} \times \vec{B} + \rho\vec{g} \tag{1.16}$$

Consider the z component of this equation (the axial direction), when the field is purely axial. Then $\vec{j} \times \vec{B}$ vanishes, and $\vec{g}_z = -g$, so we have

$$0 = -\nabla p - \rho g \tag{1.17}$$

Once again, assuming the perfect gas law (Equation 1.7), we eliminate ρ and take the integral of Equation 1.17

$$p = p_0 e^{-\int_0^z \frac{\mathrm{d}z}{\mathrm{d}\Lambda(z)}} \tag{1.18}$$

where $\Lambda(z) = \frac{k_B T(z)}{mg}$ is the pressure scale-height and is about 10^5 km in the corona.

Assuming uniform temperature, Equation 1.18 becomes

$$p = p_0 e^{\left(\frac{-z}{\gamma}\right)} \tag{1.19}$$

that is, along each magnetic field line the pressure decreases exponentially with height.

The equilibrium of the filament is maintained as the plasma cools, becomes denser and reaches a lower height. This will curve the magnetic field lines, which will the force the first term of Equation 1.13 to increase, causing the filament to remain suspended against gravity.

Chapter 2

GONG Catalog of Solar Filaments

According to Moreton and Ramsey [MR60] and Dodson [Dod49], filament oscillations have been observed after the onset of eruptive events such as flares. However, proving a correlation between filament parameters such as dimensions, period, amplitude velocity, or damping time (and a few others that we will discuss later), and the occurrence of flares (and other eruptive events) is a more complex task, since, until recently, the studies of filament oscillations have focused on a very small number of episodes.

In the paper Luna et al. [Lun+18b], 196 filament oscillations have been catalogued, along with many parameters, enabling a statistical search for that possible correlation. This will be the main focus of our work.

In the next section, we will provide a summary of the aforementioned paper.

2.1 Introduction

Luna et al. [Lun+18b] catalogued 196 filaments oscillations from the Global Oscillation Network Group (GONG) Hα network data [Lun+18a] throughout several months near the maximum of solar cycle 24 (January–June 2014).

Filament oscillations were categorized with respect to their velocity amplitude of oscillation: small amplitude oscillations (SAOs) with peak amplitude velocity $V < 10\,\mathrm{km\,s^{-1}}$, and large amplitude oscillations (LAOs) with $V > 10\,\mathrm{km\,s^{-1}}$. Both SAOs and LAOs frequently happen in the visible part

of the Sun, with approximately one occurrence of each type every two days.

SAOs are usually local and linear, since their velocity amplitudes are of the order of the speed of sound $\sim 10\,\mathrm{km\,s^{-1}}$. On the other hand, LAOs exceed the speed of sound and are usually associated with very energetic events like flares.

Luna et al. [Lun+18b] used videos from GONG Hα observations [Lun+18a], and made the selection by identifying filaments with parts which were displaced. Filaments close to the edge of the solar disk, also known as prominences, were not included.

The properties of filaments studied in the article include: filament type (according to position in the Sun), filament length and width, period of oscillation, damping time, apparent triggers, peak velocity amplitude, the directionality of oscillations with respect to the filament spine, maximum displacement amplitude, and position in the Sun.[1]

In order to be able to follow the behaviour of the filament oscillations, various telescopes were selected in order to follow the motion of the Sun in the sky, allowing a full day coverage. The telescopes used were: Learmonth (L), Udaipur (U), El Teide (T), Cerro Tololo (C), Big Bear (B), and Mauna Loa (M).

In the following sections, we will discuss in detail the filaments and their properties.

Filament Types

As discussed in the introduction, filaments were classified according to their position in the Sun (Figure 2.1), following Vial and Engvold [VE15] scheme:

- Active region (AR) filament if they are close to plages and sunspots, with a well defined spine and few or no barbs;
- Intermediate (IT) filament if they have an end close to an active region and the other end close to a quiet region in the sun, and they have a spine and barbs;
- Quiescent (QS) filament if they are far from any active region, and do not have a clear spine.

[1] The 196 events which were catalogued are available online at [Lun+18a].

In the cases where a visual classification was not possible, the authors used SDO HMI magnetograms [NAS22] to obtain a classification.

We note that the catalogue included 41 AR, 124 IT and 31 QS filaments, however the authors in Luna et al. [Lun+18b] indicated that there existed 45 AR, 99 IT and 52 QS filaments. The reason for this discrepancy is unknown. We will discuss whether this difference provides significantly different conclusions from the ones that the authors reached.

Triggering events

In order to identify the most likely triggers responsible for the filament oscillations, the authors studied videos of the region of interest (close to the filaments). When a sudden Hα brightening happened nearby, and before an oscillation onset, they marked it as FLARE, when a prominence eruption occurred close to the filament they marked it as PE, when a jet of plasma hit the filament JET, and when the trigger was a Moreton wave they marked it as MW.

From the total 196 events, the triggering agent of the oscillation was identified in about 43% of them. In this catalog, 72 filament oscillation events

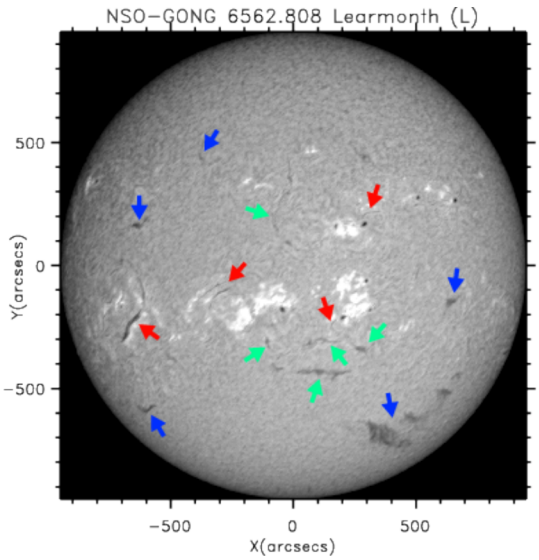

Figure 2.1: GONG Hα image from the Learmonth telescope illustrating the 3 types of filaments (dark structures). Red arrows indicate AR filaments, green arrows indicate IT filaments and blue arrows point to QS filaments.

were triggered by flares, 11 by prominence eruptions, 1 by a jet of plasma and 1 by a Moreton wave. In the remaining 111 cases, the triggering agent was not identified.

Position and dimensions

In order to determine the length L and width W of the filament, the authors used an averaged picture made up of 10 equally time-spaced observations from the same telescope. By visual inspection, the length of the spine was measured, and the average width computed as the mean of the widths at 5 equidistant points along the spine.

The position of the filament on the solar disk was taken to be the average position of the spine.

Time-distance diagrams and direction of the motion

To measure the oscillation parameters of the filaments, the authors needed to develop another technique which could be applied to curved filaments,[2] since the straight filament approach described in Luna et al. [Lun+14] could not be applied in many cases.

To accomplish this, in Hα images for each event, the path of the oscillations was tracked by visual inspection. Then the motion of the segment of the filament which displayed the clearest and largest displacement was traced. A slit, of some length l and width w, was then placed lengthwise along the curved path of that motion, and by doing so an intensity distribution along l was obtained.

Note that there was an effort to minimize the loss of resolution when generating the slits, since that the GONG data itself already had relatively low resolution.

For example, in Figure 2.2 we can see the time-distance diagram of event 1, including (in red) the slit matching the trajectory of the filament plasma [Lun+18a].

According to the authors, distances in were measured in the plane of the sky using x–y Heliocentric-Cartesian coordinates. Given that some discrepancies were found in this part of the data treatment, further investigation should be performed in close contact with the author of the original manuscript.

[2] For full details see Appendix B of Luna et al. [Lun+18b].

The angle α measures the direction between filament spine and the oscillation motion. This quantity was measured as the angle of intersection between the filament spine curve and the aforementioned slit.

Due to the difficulties in measuring α, due to the low resolution in the data, and also in the subjectiveness in generating the slit (a more complete discussion of the difficulties of this step can be found in Luna et al. [Lun+18b]), the authors have suggested automated techniques to track the motion of the filament, which they are currently developing, which will better quantify and reduce the errors in the measurement of displacement and α. Of course, since the observed displacements and velocities are projections in the plane of the sky, a dimension is missing, which could result in the real values being higher than the authors actually measured.

Oscillation Analysis

Luna et al. [Lun+14] plotted the intensity along the slit and fitted a Gaussian function to that value,[3] for each image of the observing sequence, which was done in order to obtain the central position of each filament as a function of time. The function had the form:

$$I(s) = g_0.e^{-\frac{1}{2}\left(\frac{s-s_0}{g_1}\right)^2} + g_2 + g_3 s + g_4 s^2 \tag{2.1}$$

where $g_0 < 0$ is the intensity amplitude, s is the coordinate along the slit, s_0 is the central position of the Gaussian, $g_1 = \sigma_G$ is the standard deviation, and the remaining terms are related to the background chromospheric emission. The filament motion was always taken in relation to its central position $s_0(t)$, the velocity was taken to be the numerical derivative of $s_0(t)$. Then, knowing the central position of each filament and its velocity, a function was needed to fit to the filament oscillation, a sinusoid with exponential decay, plus a third-order polynomial, of the form:

$$\begin{aligned} y(t) = A_0 e^{-A_1(t-t_0)} \cos[A_2(t-t_0) + A_3] + A_4 \\ + A_5(t-t_0) + A_6(t-t_0)^2 + A_7(t-t_0)^3 \end{aligned} \tag{2.2}$$

where A_0 to A_7 are the coefficients of the fit and t_0 is the initial time of the fitted function.

[3] Using the `gaussfit.pro` IDL routine.

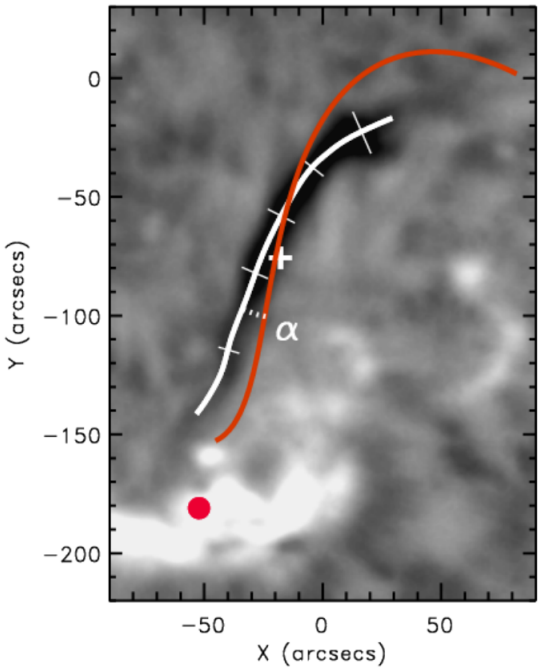

Figure 2.2: The Hα image corresponding to event 1 in the dataset. The image is the average obtained from 10 equally spaced images during the observation period. The spine path is represented by the white line, whose length is L. The red line is the slit used to follow the motion of the filament and to construct the time-distance diagrams, and the 5 thin line segments are the 5 widths measured at equidistant intervals along the spine, used to measure the average filament width, W. α (the white dotted arc) measures the angle between the direction of motion (i.e. the slit) and the filament spine. In this example, $\alpha = 16°$, $L = 260\,\mathrm{Mm}$, and $W = 15\,\mathrm{Mm}$. The white cross marks the averaged filament position on the solar disk, and the red dot marks the averaged flare position.

The parameters are extracted as follows: A_0 is the fitted displacement amplitude, $\tau = \frac{1}{A_1}$ is the damping time, and $A_2 = \frac{2\pi}{P}$ where P is the period. Of the remaining terms, A_3 is the initial phase, and the rest are related to the filaments' background motion. Long periods were filtered and not considered in this approach, since they were not present in the data.

Summary of filament parameters

Firstly we will focus on the angle α that was measured at the intersection between the direction of the oscillatory motion of the filament spine and the slit (event 1 example in Figure 2.2). The authors classified each oscillation as longitudinal for $\alpha < 40°$, or transverse, for $\alpha > 40°$. A better discussion on why this separation was made will be given in page 44.

The dynamic nature of filaments causes their shapes to change during the time interval of an observation, so this required averages of a number of images (in [Lun+14] 10 equally spaced images during a day from the same telescope were needed) of the same zone of interest of a filament in order to correctly obtain the averaged position of the filament spine, and calculate other parameters like the length, L (Mm), and average width of the filament, W (Mm)

The filament oscillation period, P (min), reflects the forces that the filaments are subjected to and how long they take to restore the equilibrium position (the position before the filament was perturbed).

The damping time, τ (min), and the number of oscillations within the characteristic damping time are given by, $|\tau/P|$. According to the article, the absolute value was considered because, in some cases, when the oscillations are amplified with time τ is negative. A small τ/P implies strong damping and vice-versa.

Maximum displacement with respect to equilibrium, A (Mm), was obtained by fitting the movement of each filament, during the fitted oscillation, with $A = \max(|A_0 e^{-A_1(t-t_0)} \cos[A_2(t - t_0) + A_3])$ (Mm) which was derived from Equation 2.2.

Lastly, the maximum velocity amplitude of each event is represented by V ($\mathrm{km\,s^{-1}}$).

All of the calculated parameters can be found in Appendix A.

Error estimation

The sources of uncertainty identified by the authors are related to the difficulties found by the lack of spatial resolution of the images, which include: difficulties in aligning the slits with the motion of the cool plasma, jitter, and exposure times, so it was assumed that the uncertainty of the oscillation parameters was directly related to the errors determining the filament position

along the slit. The choice for the uncertainty was $\sigma = 0.5\sigma_G \gtrsim \sigma_{\text{noise}}$. The authors warn that this choice of uncertainty of the filament position was somewhat arbitrary and results in an uncertainty greater than σ_{noise}, and that this will be the only source of uncertainty in the estimated oscillation parameters.

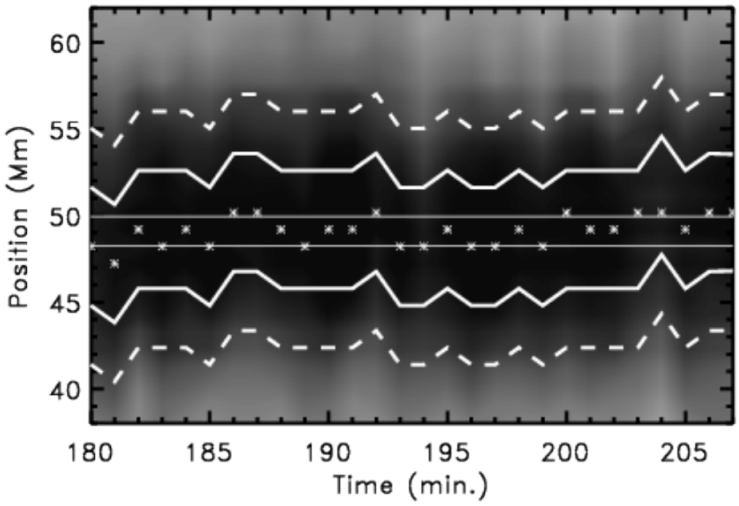

Figure 2.3: In this figure we have the time-distance diagram of an interval with no clear oscillations. The asterisks mark the central positions of the Gaussian fit, $g_1(t)$, of Equation 2.1. The standard deviation of these points is σ_{noise}; the two thin horizontal lines correspond to $\pm\sigma_{\text{noise}}$, with respect to the mean value of these positions. The two dashed curves are at $g_1 \pm \sigma_G$, containing the dark region in the diagram. The authors used $\sigma = 0.5\sigma_G$ as the uncertainty in the filament position. Here, the uncertainty region $g_1 \pm \sigma$ is delimited by two solid lines.

2.2 Results and Discussion

Histograms of events based on region type

In this section, we will analyse the histograms of the filament oscillations that were obtained from the data in Luna et al. [Lun+18b] (in the tables in Appendix A).

In Figures 2.4, 2.5, 2.6, and 2.7, we have histograms of events with respect to each oscillation parameter. On the top row of each figure, bins are separated according to velocity amplitude: LAOs in dark grey bins and SAOs in striped bins, while in the bottom row events are separated according to their location

in the Sun: active region (AR) in red, intermediate (IT) in green and quiescent (QS) in blue.

Velocity and Period

Looking at Figure 2.4a, we see that peak velocity amplitudes were detected within the range 0 to 55 $\mathrm{km\,s^{-1}}$, where only a minority of events has oscillations with peak velocity amplitude greater than 30 $\mathrm{km\,s^{-1}}$. The vertical black dashed line represents the threshold between SAOs ($V < 10\,\mathrm{km\,s^{-1}}$) and LAOs ($V > 10\,\mathrm{km\,s^{-1}}$). The number of events is smaller for higher velocity amplitudes, since very energetic events are less common.

In Figure 2.4c, we see that all three types of filaments (AR, IT, QS) follow the same decreasing tendency as total events, while also showing that all types of filaments can have SAOs and LAOs.

In Luna et al. [Lun+14] the distribution of velocity amplitudes of AR events is slightly different, with an increase of AR events between 5 and 10 $\mathrm{km\,s^{-1}}$. The reason for this discrepancy is unknown, but given that for events with peak velocity amplitude above 10 $\mathrm{km\,s^{-1}}$ the distribution is very similar to the one obtained by the authors, the conclusions do not seem to be significantly affected.

In Figure 2.4b, we see that periods vary between 30 and 110 min, with a clear maximum between 50 and 60 min. The mean value of the total population was 55.6 min with a standard deviation of 13.67 min.

For IT filaments, the average period was (56.80 ± 11.96) min, for AR filaments the average period was (49.53 ± 11.71) min, and for QS the values were a mean of (61.30 ± 19.16) min. For LAOs and SAOs the average period was (55.8 ± 13.8) min and (55.2 ± 13.4) min, respectively. The mean values and standard deviation we obtained, although using the same data, are not exactly the same obtained by Luna et al. [Lun+14], differing for example by a maximum of 4 min in AR events.

The mean values and standard deviations of LAOs and SAOs are very similar between them and also compared to the total population. This shows that the velocity amplitude of the filaments does not seem to make a significant difference to their period of oscillation.

The fact that AR type filament oscillations have a much smaller mean period than QS type filaments makes physical sense, since in quiescent zones

of the Sun there is less activity and less energetic events, and so the filament oscillations that occur in those zones will have longer periods. Also, the difference in size between AR and QS filaments types also has an effect on the normal modes of oscillation. A better understanding of the physical reason behind this will be given in section 2.2, in the discussion of the scatter plots that relate the period and width of the filaments.

Amplitude and α

In Figure 2.5a, we see that SAOs are concentrated at maximum displacement amplitudes from equilibrium between 0 and 5 Mm, with no SAOs events with $A > 9$ Mm.

LAOs have a broader distribution, peaking between 5 and 10 Mm, with almost no occurrences for $A < 5$ Mm and $A > 35$ Mm.

The progressively smaller number of LAOs with higher maximum displacement amplitudes is explained by the fact that LAOs are associated with larger filaments, which are subjected to stronger net forces and restoring forces, which then limits the maximum displacement that these filaments can have [Zur+21].

It is possible to see that the three types of filaments in Figure 2.5c are concentrated in the region $A < 10$ Mm, with fewer events with increasing A.

Although the distribution follows the same trend as in Luna et al. [Lun+14], a few more discrepancies can be observed. For example, in the amplitude histograms of Luna et al. [Lun+14] the IT events are more numerous than AR events, while in these histograms we observe the opposite.

In Figure 2.5b we see that $0 \leq \alpha \leq 90°$, and that the majority of oscillations (164/196) have $\alpha \leq 40°$, while only 32 have $\alpha > 40°$. In all detected events no LAOs have $\alpha > 65$, while a few SAOs do. The mean value for all events is $(27.00 \pm 18.14)°$, for LAOs it is $(24.50 \pm 13.93)°$ and for SAOs $(29.30 \pm 20.81)°$. For AR, IT, and QS-type filaments the mean values are $(25.10 \pm 13.07)°$, $(29.20 \pm 18.71)°$, and $(21.00 \pm 19.84)°$, respectively.

The mean values obtained for α for the different types of filaments, as seen in Figure 2.5b and d, indicate that most oscillations are aligned with the magnetic field, i.e longitudinal, since they are consistent with direct measurements of the angle between magnetic field and its spine ($\sim 25°$) [LBS83; Tan95].

In Luna et al. [Lun+14] the authors separate filaments with $\alpha < 40°$ (longitudinal) and $\alpha > 40°$ (transversal). The separation of these two populations

was done with the purpose of further studying the relation between the oscillations and the magnetic field. Although interesting, these aspects are out of the scope of this thesis, so we will not cover them.

Length and Width

In Figure 2.6a, we observe that the majority of total events have $L < 400\,\text{Mm}$, with LAOs and SAOs having a similar distribution, with mean values of $L = (275.30 \pm 191.82)\,\text{Mm}$ and $L = (209.40 \pm 156.89)\,\text{Mm}$ respectively. The mean obtained for all events was $L = (239.70 \pm 176.87)\,\text{Mm}$.

Looking at the distinction between regions, in Figure 2.6c, we that no AR type filaments have a length greater than 350 Mm. For AR we have a mean of $L = (185.80 \pm 68.82)\,\text{Mm}$, for IT we have $L = (267.30 \pm 195.16)\,\text{Mm}$ and for QS the mean is $L = (200.50 \pm 175.39)\,\text{Mm}$. As we see, the standard deviations are very large, which arise due to the low resolution when measuring these quantities. Taking this into account, we can still see that QS and IT type filaments show lengths typically longer than AR filaments, which is expected given their nature.

With respect to Figure 2.6b, we see that the majority of events have $W < 15\,\text{Mm}$. For those with $W > 15\,\text{Mm}$ SAOs are slightly more numerous than LAOs. For the set of all events, the mean obtained was $W = (11.80 \pm 4.55)\,\text{Mm}$, for LAOs it was $W = (11.30 \pm 4.11)\,\text{Mm}$ and for SAOs it was $W = (12.20 \pm 4.85)\,\text{Mm}$, showing that there is no significant difference between these two populations.

In terms of region classification, in Figure 2.6d we see that the number of AR and IT filaments decrease with increasing width. QS filaments also follow this trend for widths greater than 10 Mm, since almost no QS events were found for $W < 10\,\text{Mm}$. The mean width for AR was $W = (9.60 \pm 2.51)\,\text{Mm}$, for IT $W = (11.40 \pm 3.51)\,\text{Mm}$, and for QS $W = (16.20 \pm 6.86)\,\text{Mm}$.

In terms of both L and W the values obtained are in accordance with the typical reference length and width values found in the literature, which are 200 Mm and 5 Mm respectively [Sti02]. The fact that QS filaments are slightly thicker than the other types is also mentioned in [Ber13, p. 18].

$|\tau/P|$ and Latitude

From Figure 2.7a we see that the majority of events have $|\tau/P| < 2.5$, which means they are strongly damped, and a considerable number of filaments are

very strongly damped with $|\tau/P| < 1$. According to Luna et al. [Lun+14], $|\tau/P| \geq 10$ means that the oscillation suffers virtually no damping. LAOs (striped bins) make up the majority of events below this threshold, peaking at about $|\tau/P| = 2.25$, with virtually no occurrences above it.

SAOs show a greater dispersion, with values ranging from 0.5 to 9 and peaking at about $|\tau/P| = 2.25$.

In terms of region, we see in Figure 2.7c that all three types of filaments show the same decreasing frequency with greater $|\tau/P|$, and the majority of events in each category are also below the mentioned threshold. More considerations will be made about τ and τ/P in relation to different velocity amplitudes regimes (SAOs and LAOs) in the section 2.2.

This strong damping of oscillations, especially in filaments with great length, velocity, and mass, i.e. the ones capable of having large amplitude oscillations, implies that mechanisms for the dispersion of energy are very strong and efficient when acting upon these oscillations. Mechanisms like radiative cooling and mass accretion are proposed as probable causes in Luna et al. [Lun+14].

Finally, we will examine the distribution of latitudes. In Figure 2.7b, we see that the events are confined mainly between $\pm 40°$ as expected, since most filaments in this catalog are related to active regions, and they appear in the Sun according to Maunder's Butterfly diagram and that, regardless of SAOs or LAOs, there is a clear peak of events around $-15°$.

In Figure 2.7d the distribution of filaments over latitude simply reflects the expected relation between active and quiet zones and latitude. One of the aspects of this distribution was that the majority of IT filaments occurred between 0 and $-30°$, which coincides with histogram for latitude in Luna et al. [Lun+18b], although clear discrepancies can be detected.

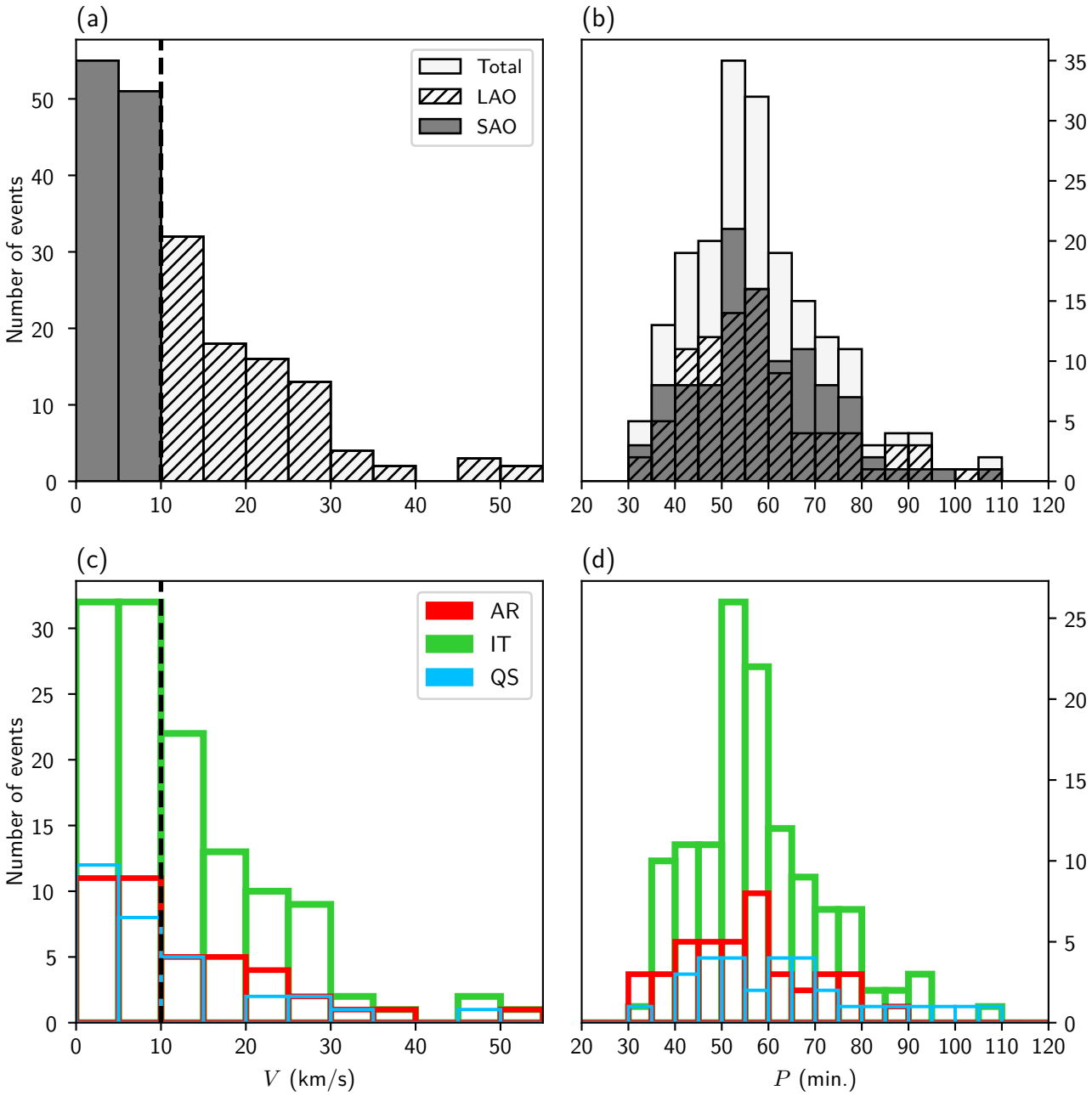

Figure 2.4: Histograms of the number of events binned by V (first column), and P (second column). In the top row the dark grey bins are SAOs, the striped bins are LAOs and the light gray area corresponds to total events. In the bottom rows the green bins correspond to IT, the red to AR and blue to QS filaments. In (a) and (c) the vertical black dashed line separates SAOs and LAOS at $V = 10\,\mathrm{km\,s^{-1}}$.

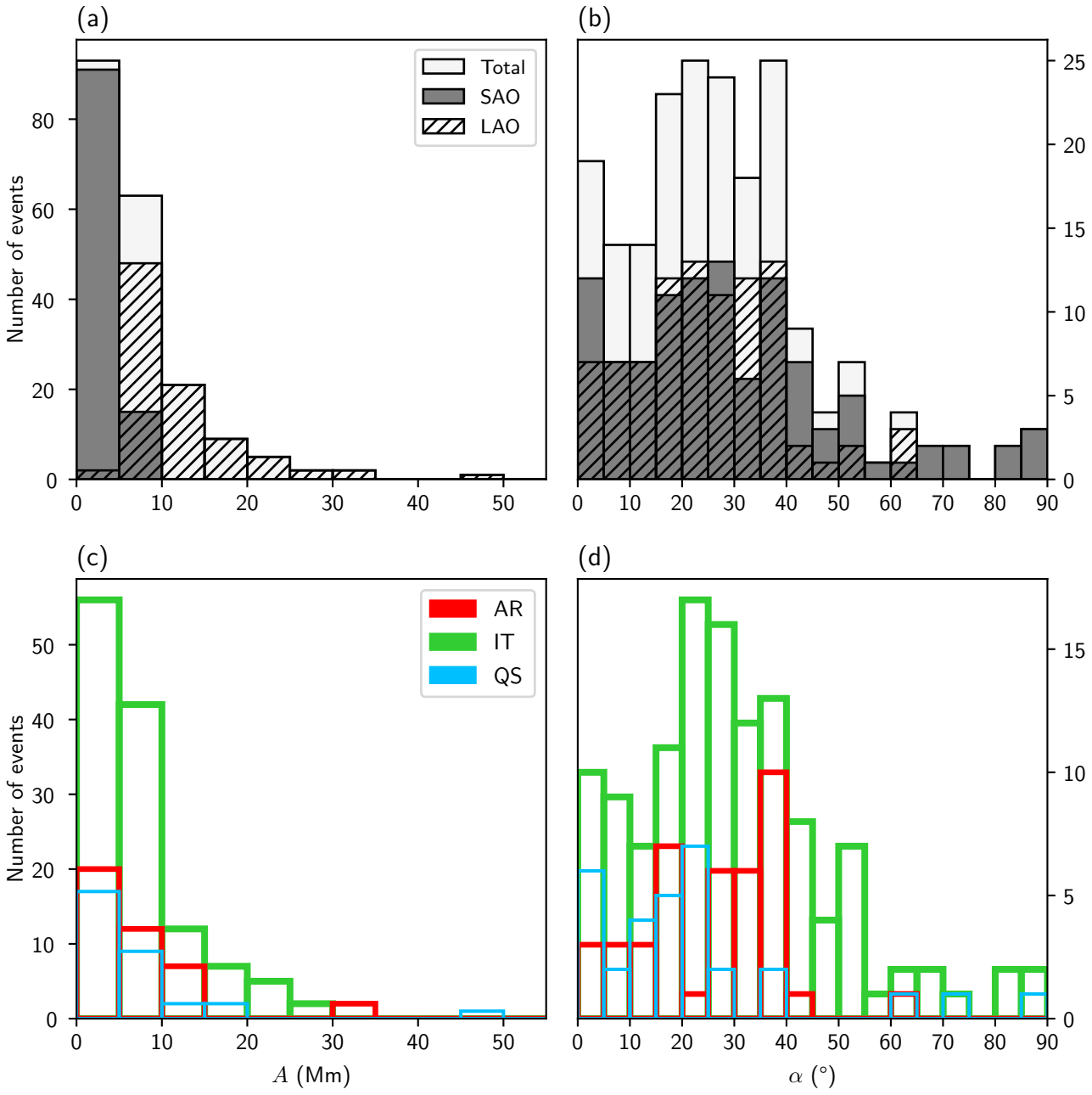

Figure 2.5: Histograms of the number of events binned by A (first column), and α (second column). In the top row the dark grey bins are SAOs, the striped bins are LAOs and the light gray area corresponds to total events. In the bottom rows the green bins correspond to IT, the red to AR and blue to QS filaments.

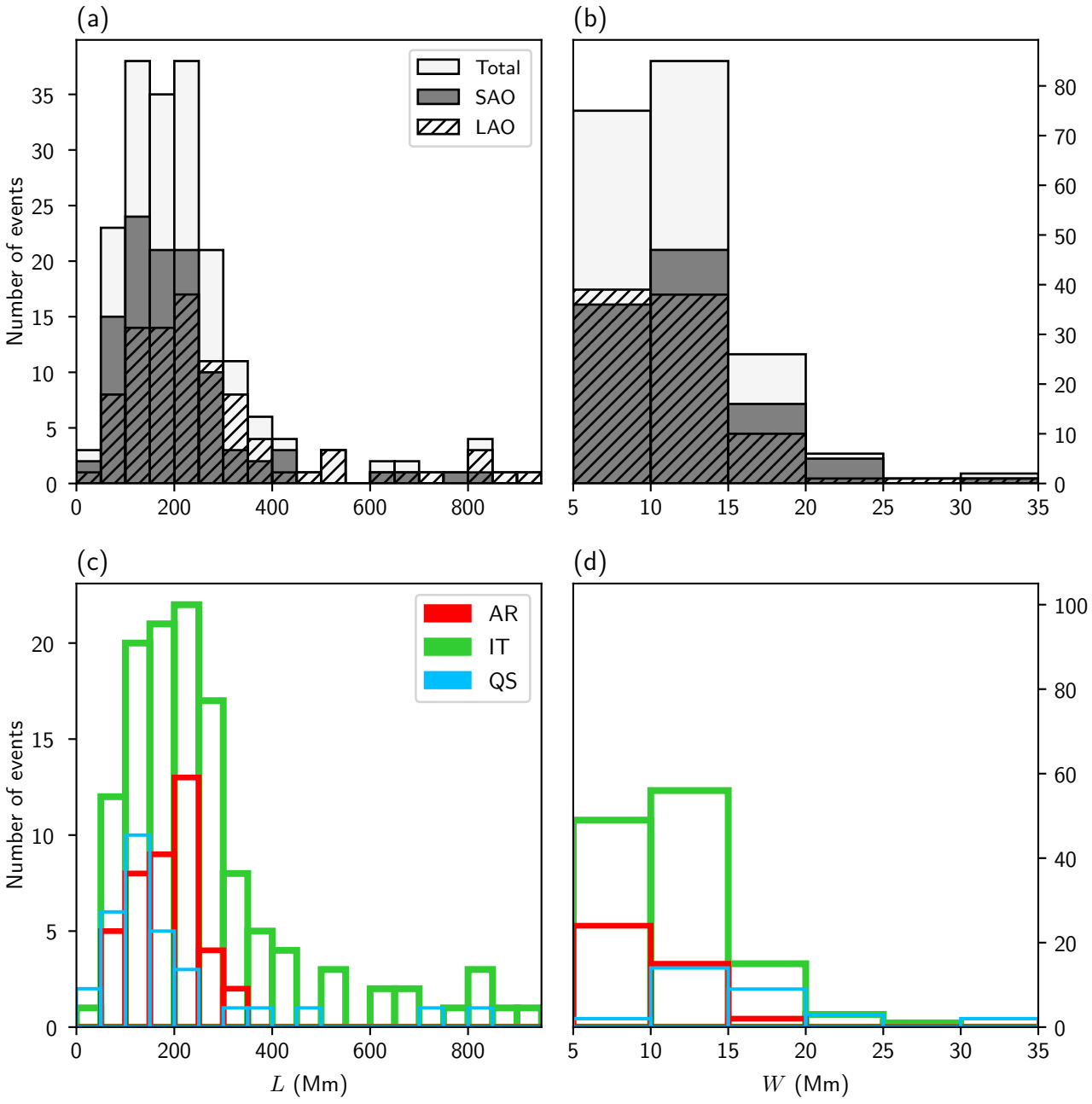

Figure 2.6: Histograms of the number of events binned by L (first column), and W (second column). In the top row the dark grey bins are SAOs, the striped bins are LAOs and the light gray area corresponds to total events. In the bottom rows the green bins correspond to IT, the red to AR and blue to QS filaments.

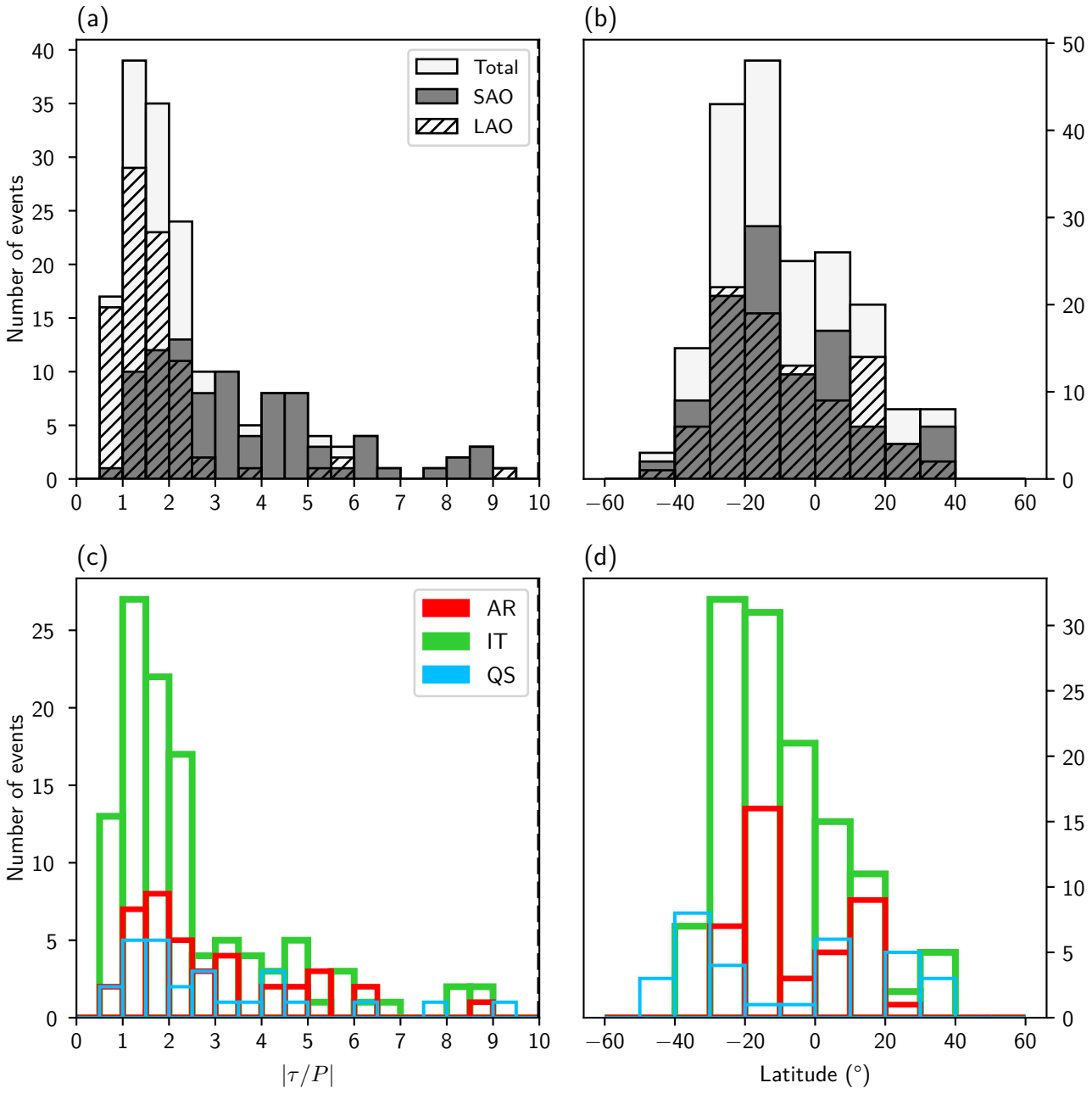

Figure 2.7: Histogram of the number of events binned by $|\tau/P|$ (first column) and Latitude (second column). In the top row the dark grey bins are SAOs, the striped bins are LAOs and the light gray area corresponds to total events. In the bottom rows the green bins correspond to IT, the red to AR and blue to QS filaments.

Histograms of events triggered by eruptive events

Over the next histograms (Figures 2.8, 2.9, 2.10, 2.11) we will examine the distribution of the oscillation parameters of filaments that have occurred after the onset of various eruptive events, like flares (violet areas), prominence eruptions (blue areas), jets of plasma (yellow areas) and Moreton waves (red areas). The total number of oscillation events is represented by the grey bars.

As mentioned before, for about 43% of the 196 total events the apparent trigger of the oscillation was identified. In total, 72 events were triggered by flares, 11 by prominence eruptions, 1 by a jet and 1 by a Moreton wave. In the remaining 111 oscillation events, the triggering agent was not identified.

In these figures, the bars display the number of events with that trigger in the specified interval (left axis), while the points display the percentage of events with the given trigger in that interval, in relation to all events with that trigger (right axis). Note that for the percentage display, we omitted the event related with a Moreton wave and the one related to the jet.

Velocity and Period

Let us start with Figure 2.8a. We see that the majority of oscillations triggered by flares and prominence eruptions have periods between 30 to 80 min, which also follows the trend of all events where the triggering event was not found.

For events triggered by flares, the mean period obtained was $P = (57.00 \pm 14.41)$ min, by PE was $P = (53.00 \pm 7.85)$ min while for all events the value was $P = (55.60 \pm 13.67)$ min. Despite the fact that these means are very similar, we do observe that while no events triggered by prominence eruptions have periods greater than 70 min, there are several events triggered by flares with greater periods.

Focusing on Figure 2.8b, we see that the range of velocity of events related to flares is mainly between 0 to 30 $\mathrm{km\,s^{-1}}$, which is also consistent with the trend for all events. For prominence eruptions, no cases were found for velocities greater than 40 $\mathrm{km\,s^{-1}}$.

The mean velocity for all events is $V = (15.00 \pm 10.80)\,\mathrm{km\,s^{-1}}$, for events triggered by flare the value is $V = (18.90 \pm 12.58)\,\mathrm{km\,s^{-1}}$, and for prominence eruption related events it reaches $V = (17.40 \pm 9.45)\,\mathrm{km\,s^{-1}}$, which suggests that events known to have been triggered by very energetic events show a higher velocity amplitude.

Length and Width

In Figure 2.9a, the majority of events triggered by prominence eruptions have lengths between 0 and 350 Mm, with 18.2% having lengths above that (between 800 and 831 Mm), while in events related to flares, most events have lengths between 0 and 450 Mm, with 12.5% having lengths above that. In terms of mean values, for total events we calculated $L = (239.70 \pm 176.87)$ Mm, for events triggered by flares $L = (264.50 \pm 189.47)$ Mm, and for events triggered by prominence eruptions $L = (305.80 \pm 251.24)$ Mm.

Looking at Figure 2.9b, we see that almost no events, of any triggering agent, were found with width greater or equal to 20 Mm. One event triggered by a flare had a width of 20 Mm and another of 33 Mm. The mean values obtained for the width flare and prominence eruption related events are (10.600 ± 3.976) Mm and (11.70 ± 3.01) Mm, respectively, while the mean width of all events is (11.80 ± 4.55) Mm. As such, there is no significant difference between widths of flare or prominence eruption related events and the average width of all events.

Amplitude and α

From Figure 2.10a, we observe that the majority (in this case 84.7%) of events triggered by flares have amplitudes shorter than 15 Mm. In regard to PE-related events, none were found with displacement amplitudes greater than 15 Mm. In fact, above this threshold, all events were caused by flares.

In terms of mean amplitude displacements, for all events the value was (4.80 ± 4.51) Mm, for prominence eruption-related events it was (5.70 ± 4.20) Mm, and for flare-related ones the value was (6.40 ± 6.07) Mm.

We conclude from these results that oscillation events that were triggered by very energetic phenomena have greater amplitudes than in the cases were no triggering was found, as we expected.

As seen in Figure 2.10b, most oscillations, regardless of trigger, have $\alpha < 40°$. While a few events occurred for $\alpha > 40°$, only 11% of events related to flares, and 18% of events related to prominence eruptions occurred above this threshold. In terms of mean values for α, globally the result was $(27.10 \pm 18.14)°$, for flare related events it was $(25.40 \pm 13.54)°$ and for prominence eruption related events the value was $(28.80 \pm 20.98)°$. From this graph we can conclude

that the separation between longitudinal ($\alpha < 40°$) and transversal ($\alpha > 40°$) oscillations (discussed in section 2.2) also applies when the triggering agent is identified as a flare or a prominence eruption.

τ/P and Latitude

By looking at Figure 2.11a, we see that most events caused by flares have τ/P smaller than 3.5, while the ones caused by prominence eruptions are mostly concentrated in the region $\tau/P \leq 2$. This shows that most events caused by very energetic phenomena were strongly damped, which can be explained by the fact that, as discussed in section 2.2, strong damping might be related to mass accretion associated with thermal nonequilibrium [Lun+18b]. Events associated with violent triggers display higher V, which leads to increased evaporation and stronger damping. The mean value of τ/P was 1.20 ± 0.32 for all events, 1.20 ± 0.20 for events triggered by flares and 1.40 ± 0.35 for events triggered by PEs.

And finally, Figure 2.11b shows that all events related to eruptive phenomena take place in the region between $\pm 40°$ latitude. The mean latitude for all events was $(-8.60 \pm 18.20)°$, for flare-related events was $(-7.30 \pm 17.30)°$, and for prominence eruption-related events was $(-21.50 \pm 14.81)°$. The fact that flare-related events are within the Maunder's belt is again expected, as it is where most eruptive events occur.

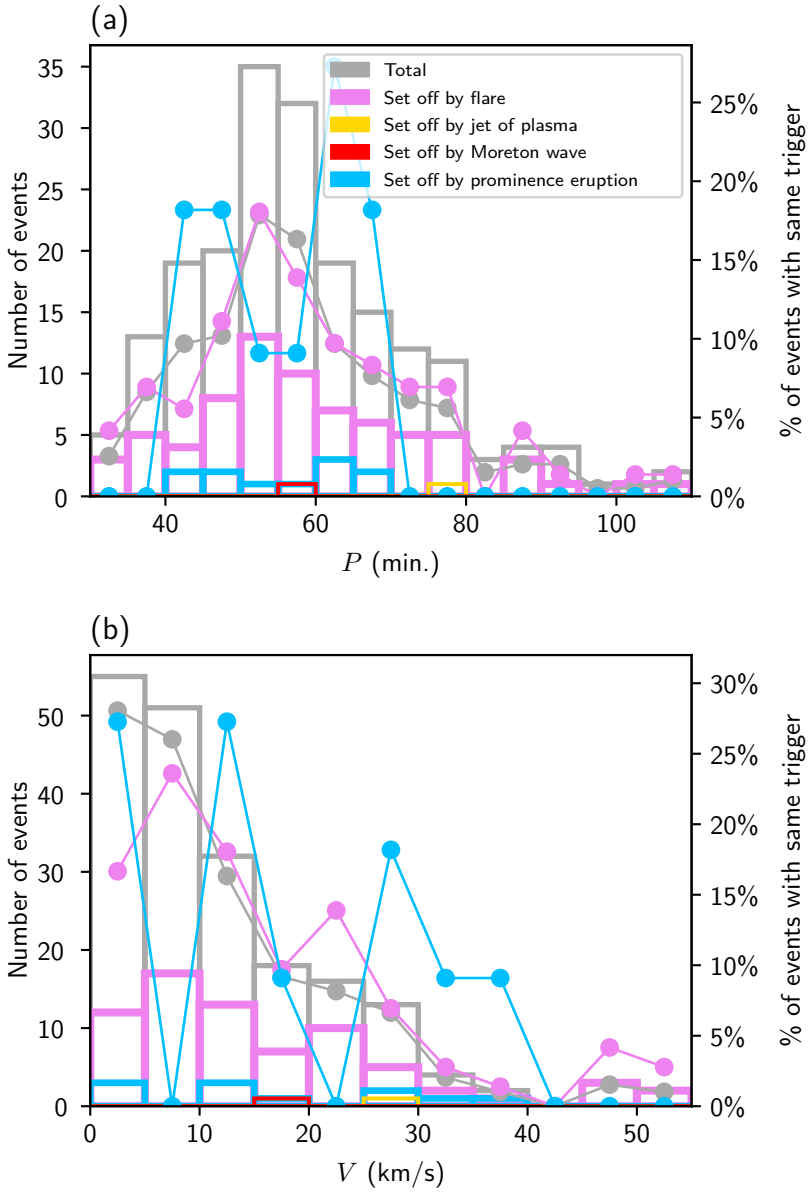

Figure 2.8: Histogram and scatter plot of P (a) and V (b). Bins: number of cases in interval (left axis). Points: the percentage of events with that trigger in that interval, over total number of events with same trigger (right axis). Grey markers represent the total cases, while coloured ones represent the cases where the trigger for the filament oscillation was identified (see legend).

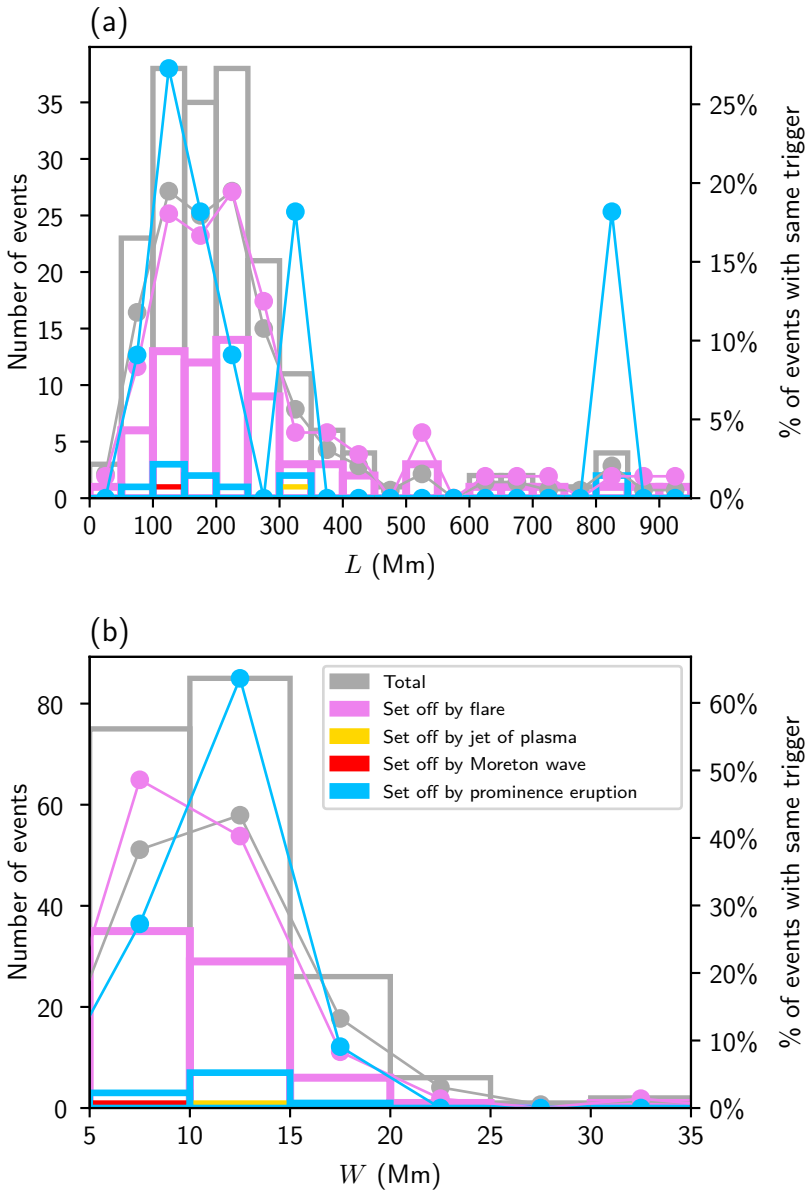

Figure 2.9: Histogram and scatter plot of L (a) and W (b). Bins: number of cases in interval (left axis). Points: the percentage of events with that trigger in that interval, over total number of events with same trigger (right axis). Grey markers represent the total cases, while coloured ones represent the cases where the trigger for the filament oscillation was identified (see legend).

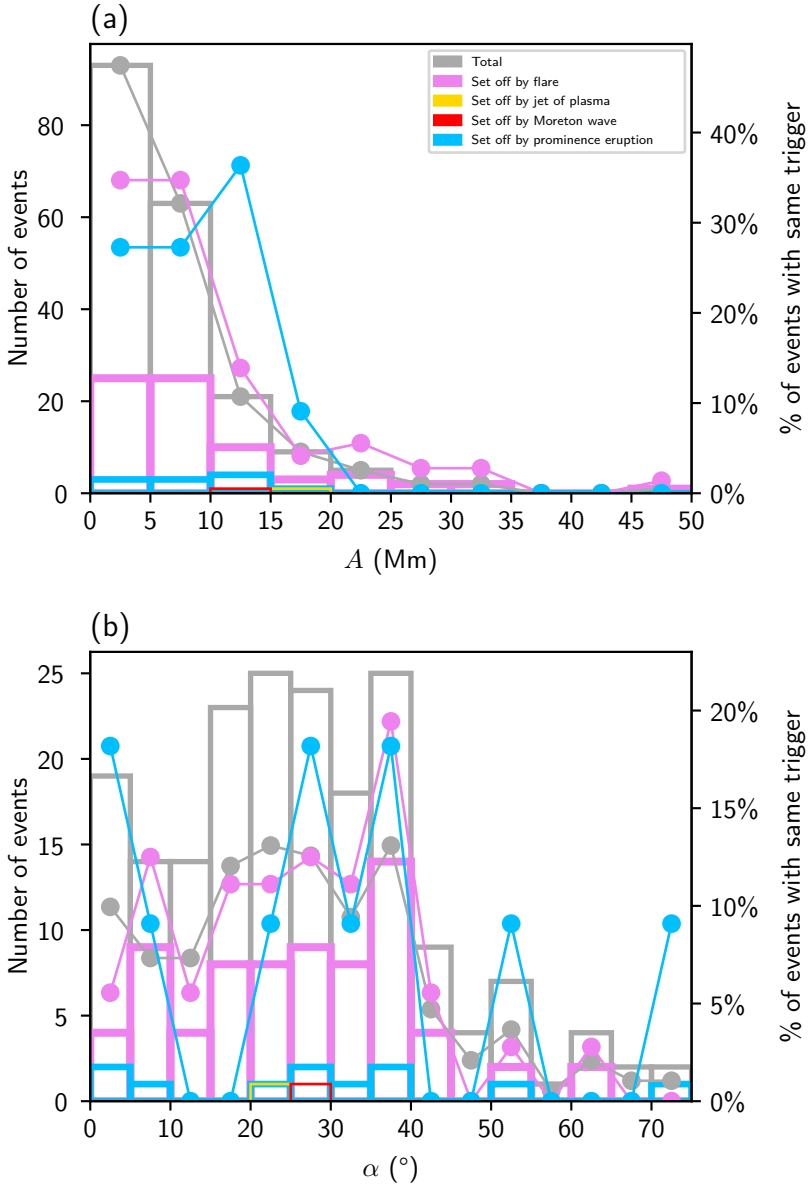

Figure 2.10: Histogram and scatter plot of A (a) and α (b). Bins: number of cases in interval (left axis). Points: the percentage of events with that trigger in that interval, over total number of events with same trigger (right axis). Grey markers represent the total cases, while coloured ones represent the cases where the trigger for the filament oscillation was identified (see legend).

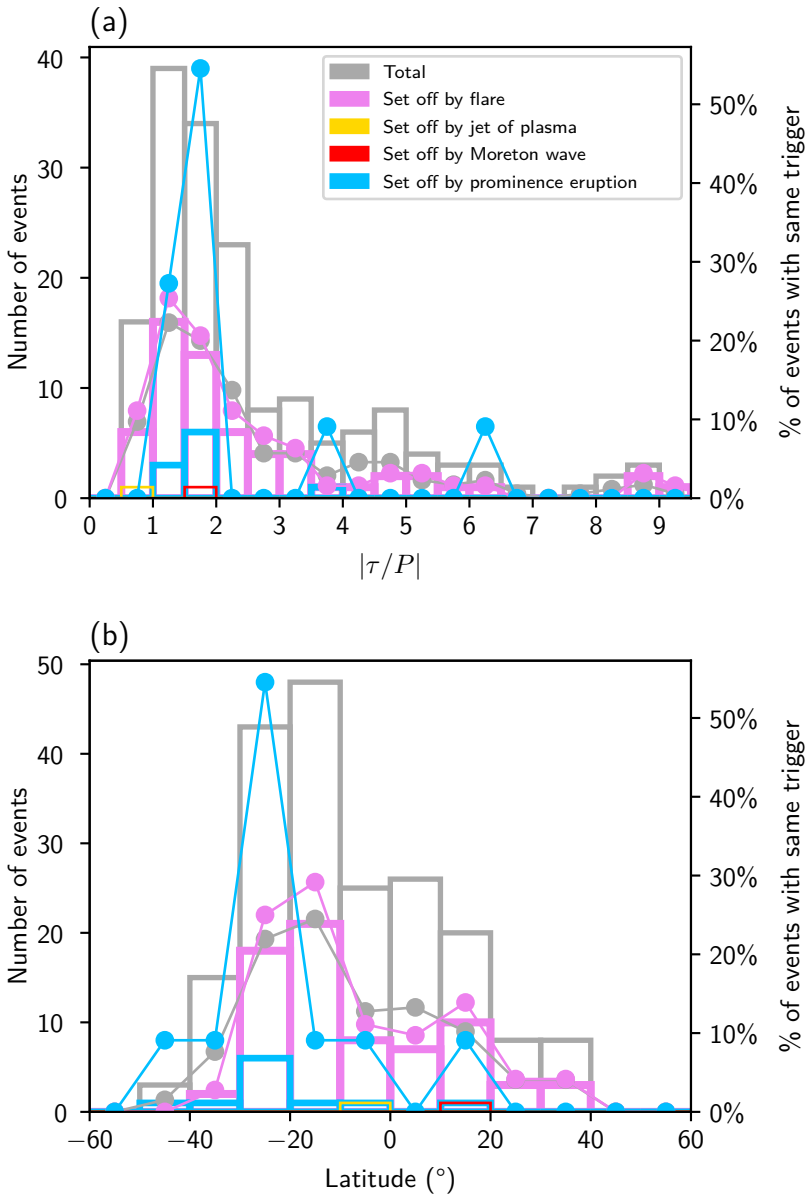

Figure 2.11: Histogram and scatter plot of $|\tau/P|$ (a). Bins: number of cases in interval (left axis). Points: the percentage of events with that trigger in that interval, over total number of events with same trigger (right axis). Grey markers represent the total cases, while coloured ones represent the cases where the trigger for the filament oscillation was identified (see legend).

Relations between parameters based on region type

In this section (Figures 2.12, 2.13 2.14, 2.15), we will focus on studying the relations between different pairs of parameters of the oscillation events, examining correlations with the filament region type (AR, IT, QS) and velocity amplitude of oscillation (SAO, LAO).

In these scatter plots, filament region type is distinguished by colour (AR in red, IT in green, QS in blue), and velocity amplitude is distingushed by marker shape (SAO in diamond, LAO in circle).

Period, Velocity, Amplitude and $|\tau|$ vs α

In Figure 2.12a, the region $\alpha < 20°$ is where the dispersion of periods is wider, going from 30 to 110 min. From there, the range of periods becomes progressively narrower: from $20° < \alpha < 40°$ periods vary from 30 to 95 min and for $40° < \alpha < 60°$ the maximum they reach is 75 min. Clearly, the period maximum decreases with increasing α, until $\alpha > 70°$ where the range of periods appears to widen again (with one event reaching almost 100 min), although only very few events exist in that region. The behaviour of period with α seems to be the same for all three types of filaments.

In Figure 2.12b, where we observe the relation with V, there is a clear threshold at $\alpha = 40°$, where above this value the majority of events reach only much lower velocities, and are mostly of intermediate (IT) regions. No LAOs were detected with $\alpha > 65°$.

The trend of decreasing periods with α, and the decrease of velocities for $\alpha > 40°$, shows a dependency of these parameters on the polarization of the oscillations. According to Wang et al. [Wan+16] and Zhou et al. [Zho+17], oscillations aligned with the magnetic field, i.e. $\alpha < 40°$ (longitudinal) tend to have larger periods than oscillations with $\alpha < 40°$ (transverse oscillations).

In many cases the filament does not oscillate as a whole, only parts of it. Also, because filaments are structures that display narrow threads that are aligned with the magnetic field, while also existing at an angle with the spine, this causes the spine to not be a magnetically coherent structure throughout its whole length. According to Luna et al. [Lun+14], while transverse oscillations are related to a coherent motion of the whole magnetic structure of the filament, in the longitudinal cases the oscillations are mostly from individual threads.

In Figure 2.12, we see that while AR and QS events are mainly concentrated between amplitudes 0 and 15 Mm for AR, and 20 Mm for QS, with α between 0 and 40°, IT type events have a wider dispersion.

Looking at Figure 2.12d, we see again that AR and QS type filaments occur mainly in events with $0 < \alpha < 40°$ and for $|\tau|$ lower than ≈ 300 min; note that some events of both types also reach higher values. IT type filaments have a broader distribution in terms of α, and we see that for $\alpha > 42°$ all events have $|\tau| < 300$ min, with all but 4 being of other types.

Period vs Amplitude, Velocity, Length and Width

Let us now focus on Figure 2.13a, where we see that the majority of AR and QS-type filaments have amplitudes below 14 Mm, and cover a large range of periods (although AR filaments do not surpass 80 minutes). For higher amplitudes, the events have higher periods as well. As expected, there are no events which display low P and large A, since $V \sim A/P$, and therefore events in the region of low P and large A would imply very large V, but events with that feature were not detected.

In Figure 2.13b, it is clear that AR-type events exist inside a belt with $V < 26\,\mathrm{km\,s^{-1}}$ and $P < 80$ min. No significant correlation between P and A or P and V, occurred, and for this reason the hypothesis that LAOs were non-linear does not hold, since non-linear oscillations have a period dependency on V or A.

In Figure 2.13c, it can be seen that for $L > 337$ Mm no AR type events are found, and that for lengths lower than this value their typical periods are lower than 80 minutes. The majority of QS events also lie in that region, with only three events detected with a higher length. Unlike AR filaments, however, they reach longer periods.

According to Luna et al. [Lun+18b], many theoretical models of MHD predict a relation between period and length and width. Although for P and L no correlation was found, between P and W there is, as we will see below.

In Figure 2.13d, for QS filaments, we were able to identify that periods tend to increase linearly with width, with a correlation coefficient of ~ 0.75, therefore, we conclude that wider QS filaments tend to oscillate with longer period than

narrower ones.[4] We also see that AR events do not have widths greater than $W = 17\,\text{Mm}$, nor periods lower than 80 min.

Period vs $|\tau/P|$, $|\tau|$ vs Velocity, $|\tau/P|$ vs α

In Figure 2.14a, we see that for $|\tau/P| < 3$ the events show a high dispersion of periods, with P varying between 0 and 110 min. After that threshold, the events are rarer, and never surpass $P = 76\,\text{min}$. We can conclude that, as expected, strongly damped oscillations have longer periods.

In Figure 2.14b, we see a non-linear correlation of $|\tau|$ with V, as $|\tau|$ decreases with increasing V. In Zhang et al. [Zha+13], this relation is found to obey roughly a power law with $\tau \propto V^{-0.3}$. With our data, we have found a relation of $\tau \propto V^{-k}$ with $k = 0.326 \pm 0.059$, consistent with the previously mentioned literature. According to Luna et al. [Lun+18b], this relationship might be explained by a combination of mechanisms of mass accretion and radiative cooling.

In short, looking at Figure 2.14c, we see that the majority of events have $\alpha < 40°$ in that range they have a wide dispersion of $|\tau/P|$, and beyond that value of α the number of events diminishes, as we observed in the V–α and A–α plots.

As for the oscillations with negative τ (represented by the black-border points), i.e., the oscillations that were amplified in time instead of damped, a more detailed explanation of their nature is out of the scope of this discussion.

Velocity vs Latitude, Period vs Latitude, Amplitude vs Latitude, α vs Latitude

In Figure 2.15a, we see that the majority of AR filaments are located within a band of approximately $-21°$ and $+21°$ latitude, reaching high velocity amplitude in this zone, which is expected since most solar activity happens in this zone, and thus more energetic events cause these events to reach higher V. QS type filaments, of course, exist on higher latitudes. Observing those in the south hemisphere, we see that in some cases they reach high velocity as well.

In Figure 2.15b, again, we clearly see that AR filaments are located within the expected latitudes, and we see that the range of periods is quite large,

[4] As also concluded in Luna et al. [Lun+18b].

although no AR events have $P > 87\,\mathrm{min}$, while other types of filaments, like IT and QS, do reach higher values of P.

From Figure 2.15c, we see that, for almost all events regardless their latitude, they have $A < 20\,\mathrm{Mm}$.

Finally, from Figure 2.15d we see that only one AR event has $\alpha > 41°$, while the other types have a non-negligible amount of events which are transverse.

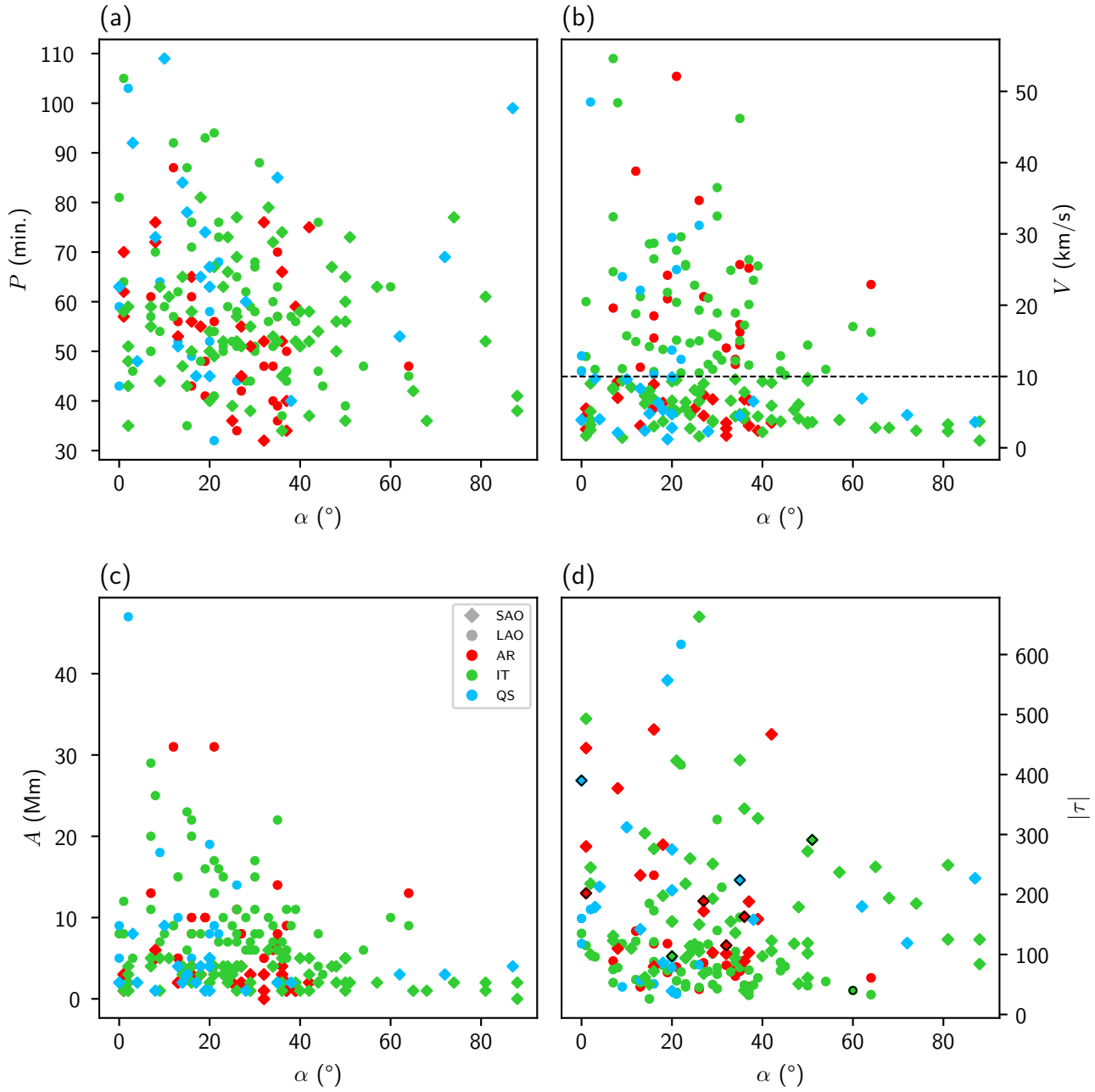

Figure 2.12: Scatter plots of (a) P vs α, (b) V vs α, (c) A vs α, and (d) $|\tau|$ vs α. Filament position type is distinguished by colour, while velocity amplitude category is distinguished by shape (see legend).

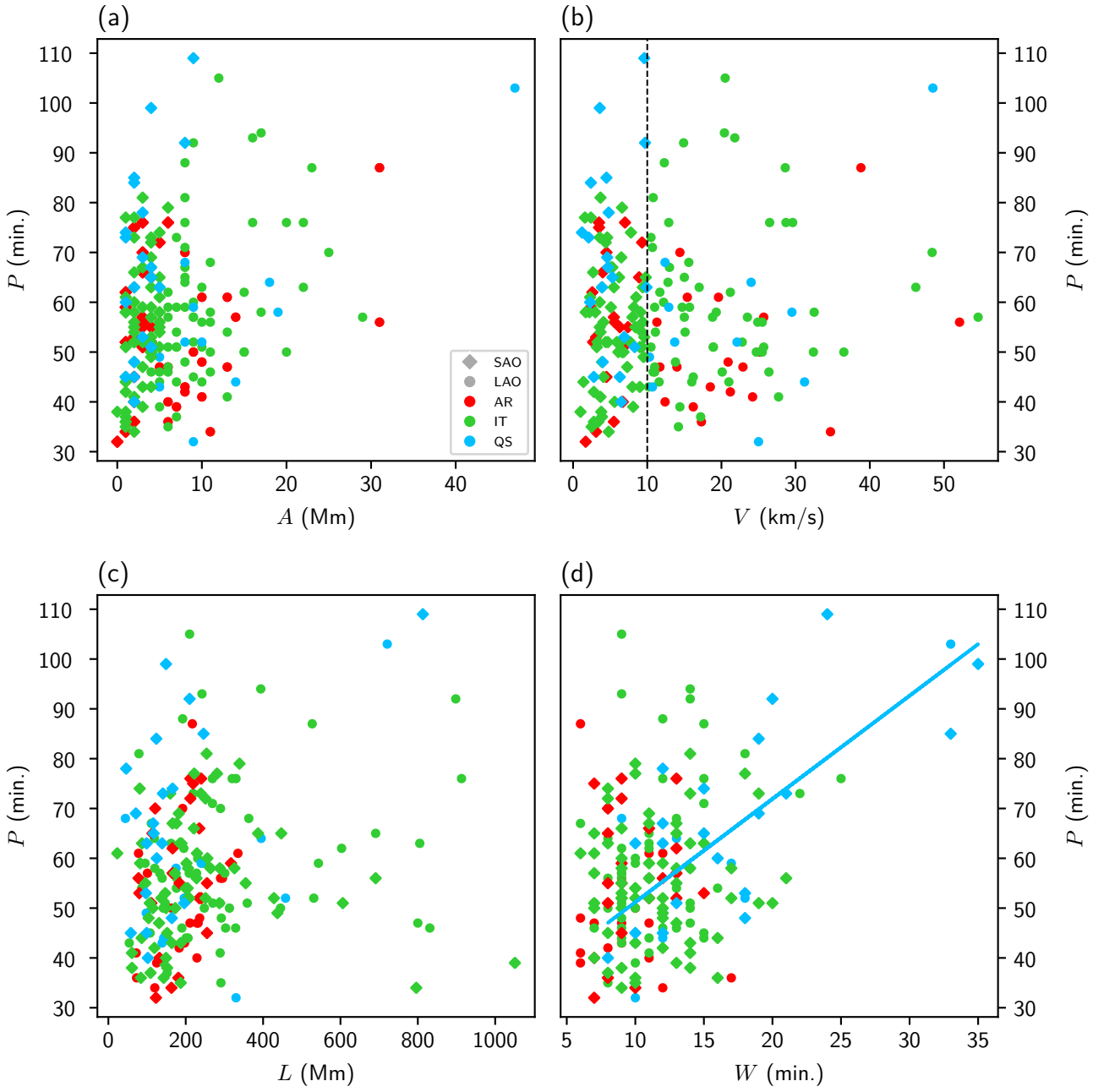

Figure 2.13: Scatter plots of (a) P vs A, (b) P vs V, (c) P vs L, and (d) P vs W. Filament position type is distinguished by colour, while velocity amplitude category is distinguished by shape (see legend).

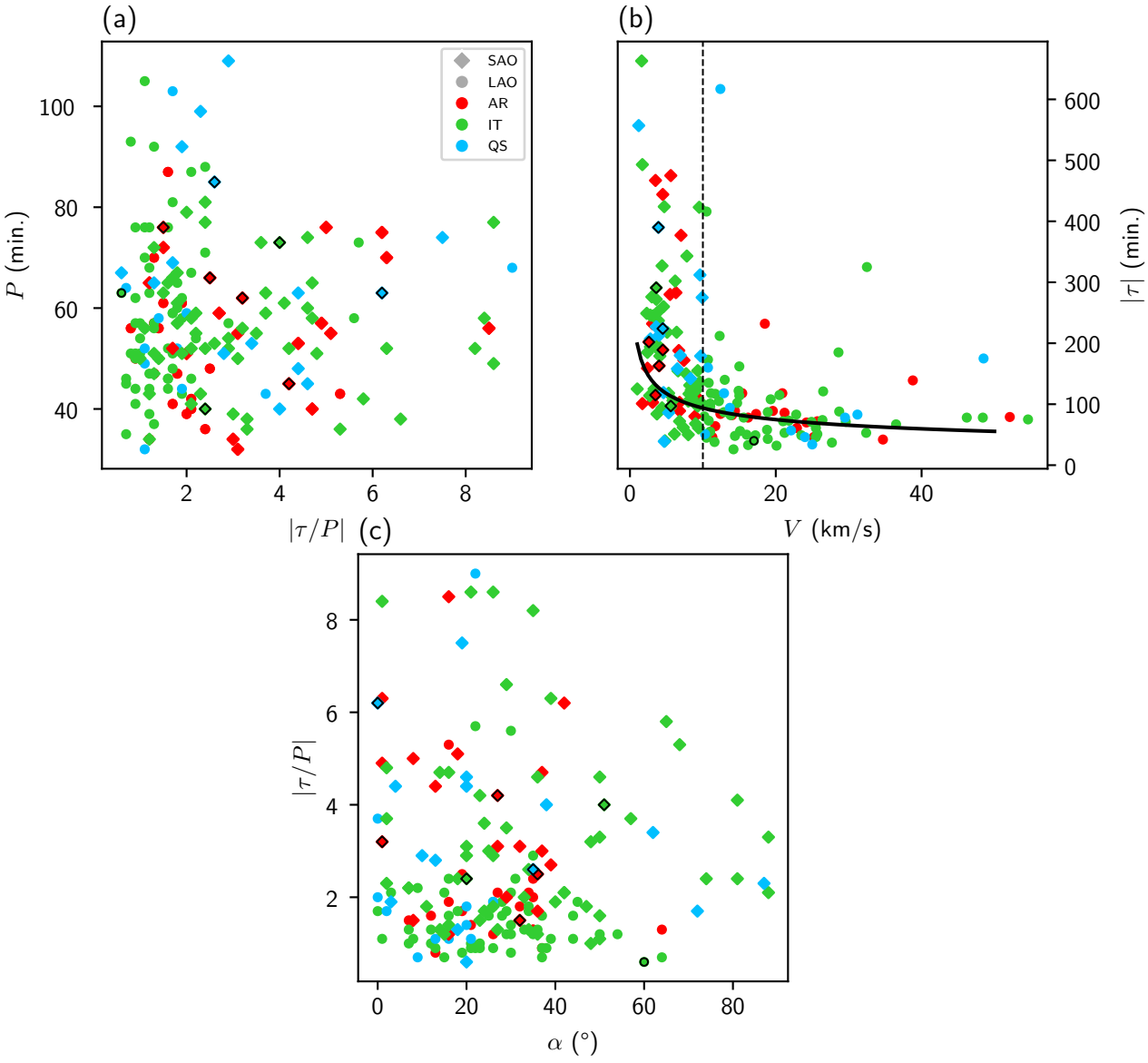

Figure 2.14: Scatter plots of (a) P vs $|\tau/P|$, (b) $|\tau|$ vs V, and (c) $|\tau/P|$ vs α. Filament position type is distinguished by colour, while velocity amplitude category is distinguished by shape (see legend).

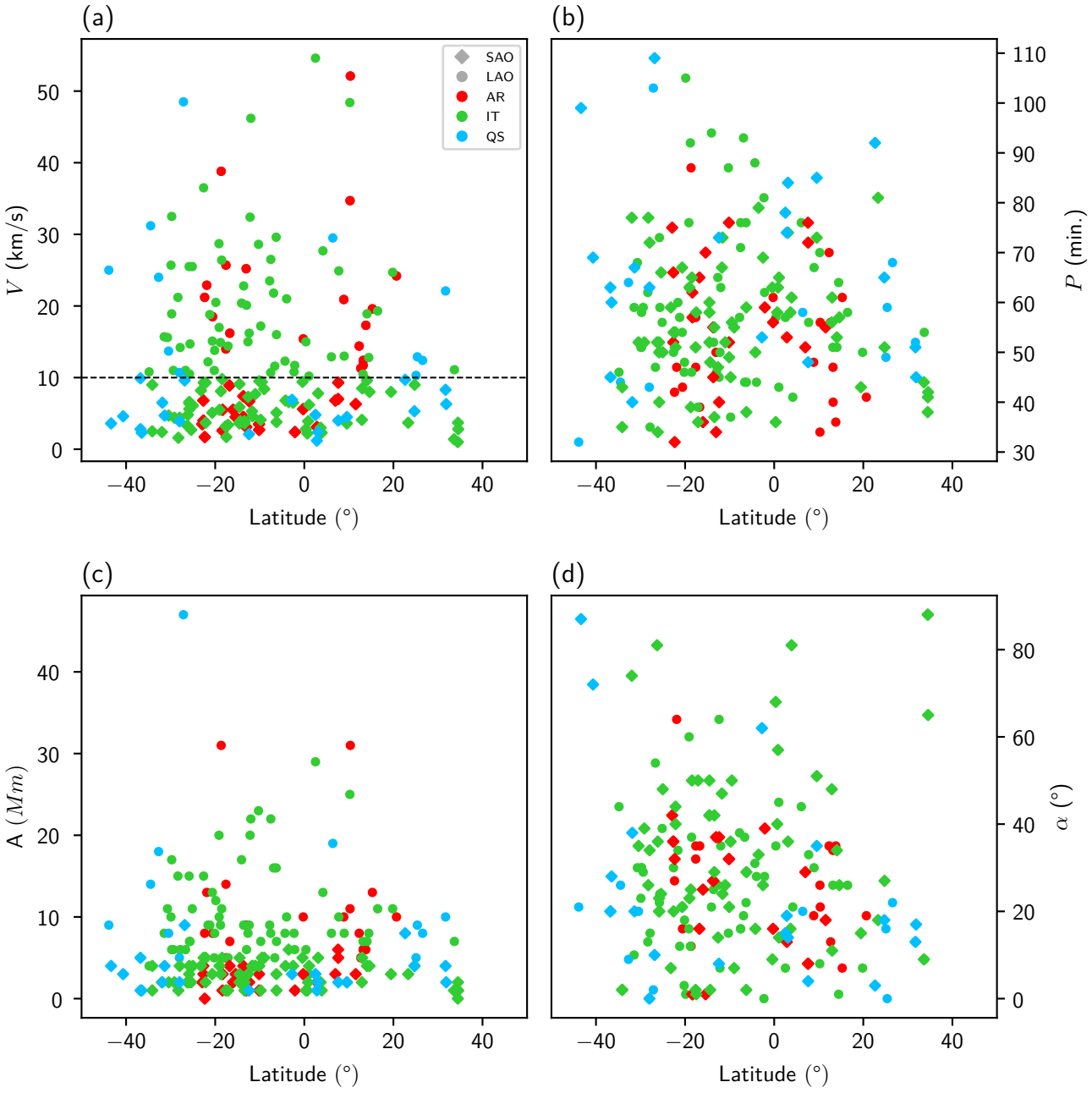

Figure 2.15: Scatter plots of (a) V vs Latitude, (b) P vs Latitude, (c) A vs Latitude, and (d) α vs Latitude. Filament position type is distinguished by colour, while velocity amplitude category is distinguished by shape (see legend).

Relations between parameters and triggering events

We will now focus on Figures 2.16, 2.17, 2.18, and 2.19 to see if any thresholds are present that could indicate preferential regimes in which a higher correlation exists between the onset of oscillations and triggering events.

Period, Velocity, Amplitude and $|\tau|$ vs α

Looking at Figure 2.16a, we see that, for all ranges of α, no prominence eruption events were found with oscillation period greater than 72 min. The majority of total events are located between period ranges of 0 to about 80 min, and below $\alpha = 50°$. For the majority of events above $\alpha = 50°$ the triggering agent was not found. Unlike prominence eruption-related events, for flares the events reached longer periods, especially when considering the regime $\alpha < 50°$. The calculation of correlation coefficients shows that there is no linear correlation between P and α for events set off by flares or prominence eruptions.

Looking at Figure 2.16b, we see that for $\alpha < 40°$, and above $V = 30\,\mathrm{km\,s^{-1}}$, all events except one were related to eruptive events, especially flares. For $\alpha > 60°$ the number of events related to eruptive events is much smaller than when considering smaller values of α. Again, no linear correlation was found between these two parameters, regarding the origin of oscillations being flares or prominence eruptions.

In Figure 2.16c, we see that no events caused by prominence eruptions, for any value of α, have amplitude displacement greater than 15 Mm. For amplitudes greater than 20 Mm, all events were caused by flares, and all had $\alpha < 40°$.

By looking at this graph, and also at Figure 2.16b, it seems that events related with eruptive triggers tend to happen if they have very long A or high V and are longitudinal (i.e. have $\alpha < 40°$). In chapter 3 we will discuss this observation in more detail.

In the case of Figure 2.16d, the distribution seems more disperse, although we see that above the traced grey line no prominence eruption caused oscillation events. It is also clear that the majority of events related to eruptive triggers are below this line.

Period vs Amplitude, Velocity, Length and Width

Considering Figure 2.17a, we see that for amplitudes smaller than 15 Mm, no events caused by prominence eruptions had periods greater than 70 min. Also, for amplitudes greater than 17 Mm all events (apart from 2 cases) were caused by flares. The linear correlation coefficients were 0.49 and -0.52 for events related to flare and to prominence eruptions respectively. Therefore we conclude that there is a moderate positive association, and a negative one, between P and A regarding the origin of the oscillations being flares or prominence eruptions, respectively.

In Figure 2.17b, similar tendencies can be seen, as the prominence eruption events are confined to maximum period of about 70 min for velocities between 0 and 37 $\mathrm{km\,s^{-1}}$. We also see that the majority of prominence eruption events occur for velocities greater than 10 $\mathrm{km\,s^{-1}}$. We can also see that for higher V and longer P, the majority of events are related to flares, so this regime seems to be somewhat preferential.

Looking at Figure 2.17c, events related to prominence eruptions are mostly confined to a belt with maximum length $L = 336$ Mm and maximum period of about $P = 70$ min. Above $L = 500$ Mm and periods greater than 56 min, the majority of events have been caused by flares. For events set off by flares, the linear correlation coefficient was 0.49, which means a moderate positive association between these two parameters.

In Figure 2.17d, we see another interesting zone when considering widths between 8 and 19 Mm and periods between 42 and 69 min, where events caused by prominence eruptions exist. Also flare-related events seem to only happen for a narrow range of widths, mainly for $W < 17$ Mm, but display a wide range of periods in that zone. Above this threshold of $W = 17$ Mm and $P = 50$ min, only one event was set off by a flare, and none was triggered by prominence eruptions.

Period vs $|\tau/P|$, $|\tau|$ vs Velocity, $|\tau/P|$ vs α

Looking at Figure 2.18a, we also observe that prominence eruption events happened mainly for $|\tau/P| < 2$ and for periods shorter than 70 minutes. Two events have $|\tau/P| > 2$ and are also under the same threshold in terms of

period. In terms of flare-related events, most are concentrated at $|\tau/P| < 3.5$, and in that region their period values cover all the possible range. No linear correlation has been found between P vs $|\tau/P|$ and the triggering agents of the oscillations.

In Figure 2.18b, we see that eruptive events with $V > 10\,\mathrm{km\,s^{-1}}$ (LAOs) have short damping times, generally less than 210 min, with only one event reaching $\tau = 324\,\mathrm{min}$, while those with $V < 10\,\mathrm{km\,s^{-1}}$ (SAOs) have a markedly broader distribution of damping times. We also see that for $V > 32.7\,\mathrm{km\,s^{-1}}$ all events were triggered by eruptive triggers, as discussed in the corresponding part of the previous section (2.2)

From Figure 2.18c, we conclude that the majority of eruptive events occur for oscillations with $\alpha < 40°$ (longitudinal), and in the region of $0.5 < |\tau/P| < 5.5$. No linear correlation has been found in this case, with respect to the occurrence of eruptive events.

V vs Latitude, P vs Latitude, A vs Latitude, α vs Latitude

In Figure 2.19a we see that prominence eruption-related events happened mostly for $V > 10\,\mathrm{km\,s^{-1}}$ and in the south hemisphere, at latitudes between $-18°$ and $-40°$. Above $V = 32\,\mathrm{km\,s^{-1}}$ and at latitudes between $-30°$ and $10°$, all events were related to eruptive events.

In Figure 2.19b the dispersion of the points does not seem to indicate a specific preferential zone, apart from the aforementioned concentration of prominence eruption events for latitudes between $-18°$ and $-40°$

In Figure 2.19c we see that for amplitudes greater than 19.5 Mm all events were triggered by flares, and all have latitudes between $-20°$ and $10°$. PE events seem to have a preference for negative latitudes and for small amplitudes, maxing at about 15 Mm.

Finally in Figure 2.19d, again a great dispersion is found, with no evident preferential zones, apart from the fact that for latitudes greater than $-15°$ and for $\alpha > 40°$ no eruptive events were found to be in the cause of oscillations.

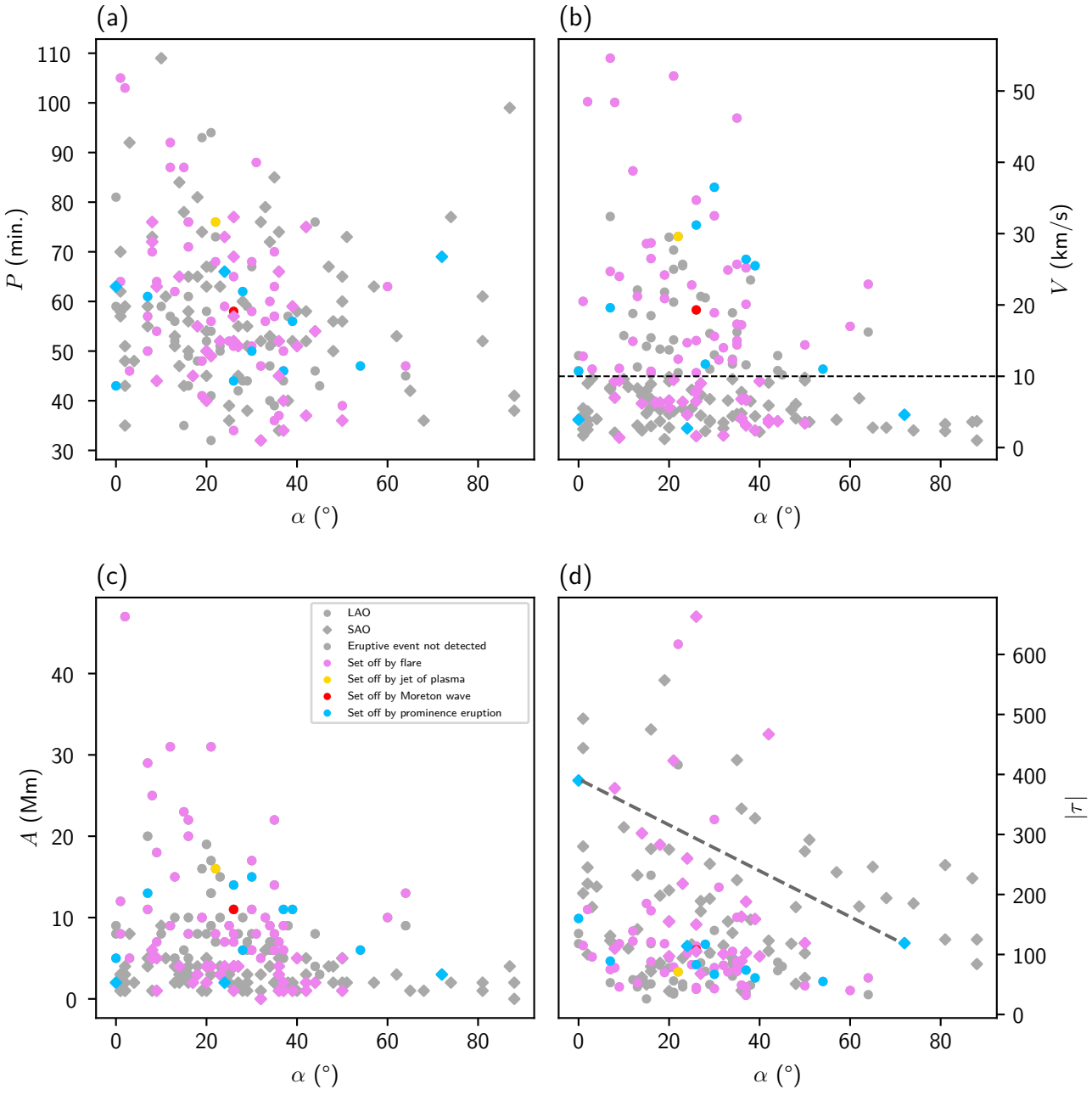

Figure 2.16: Scatter plots of (a) P vs α, (b) V vs α, (c) A vs α, and (d) $|\tau|$ vs α. Filament oscillation events where the trigger is not identified are represented by grey points, while events with associated trigger are represented by different colours (see legend).

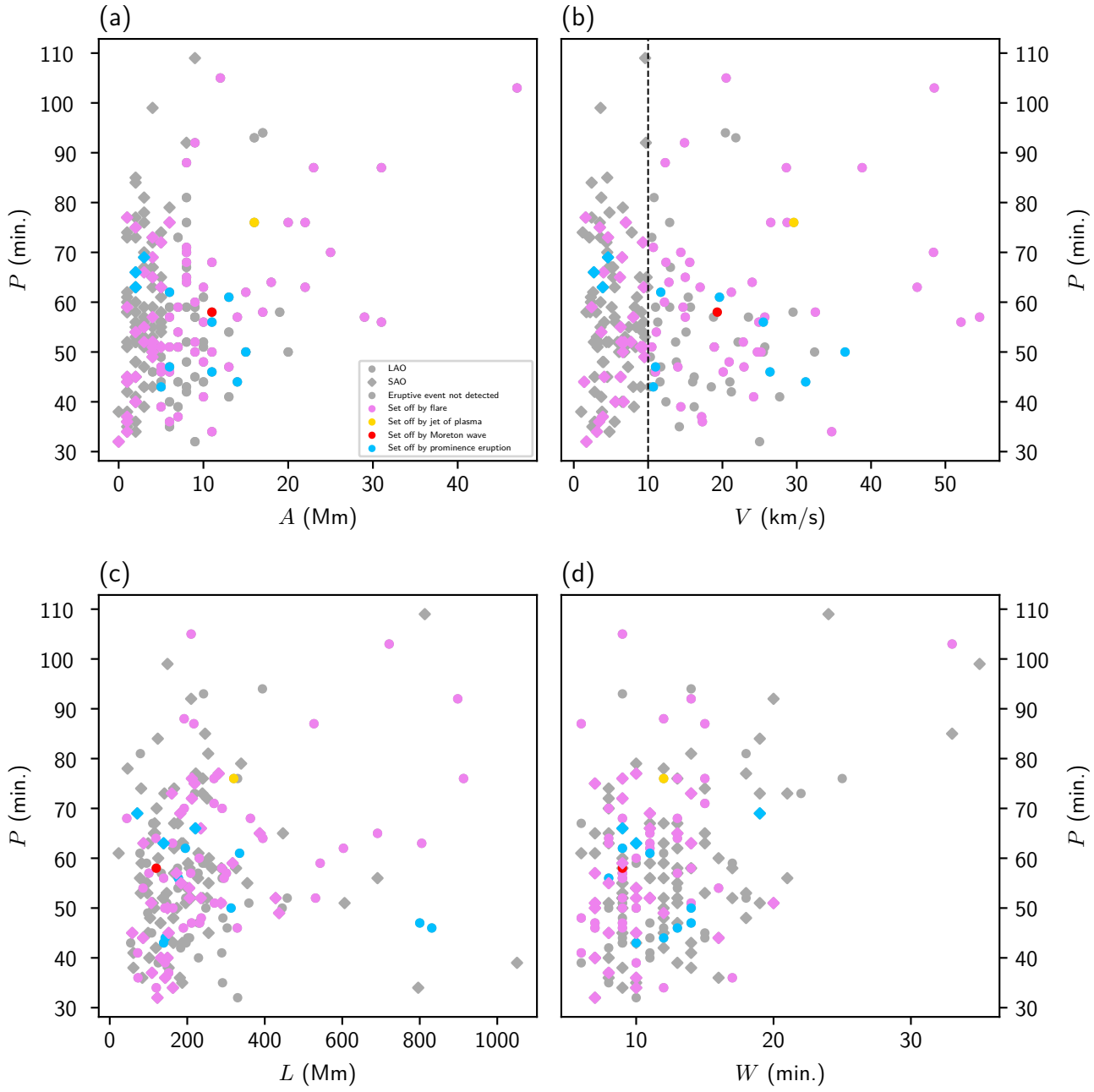

Figure 2.17: Scatter plots of (a) P vs A, (b) P vs V, (c) P vs L, and (d) P vs W. Filament oscillation events where the trigger is not identified are represented by grey points, while events with associated trigger are represented by different colours (see legend).

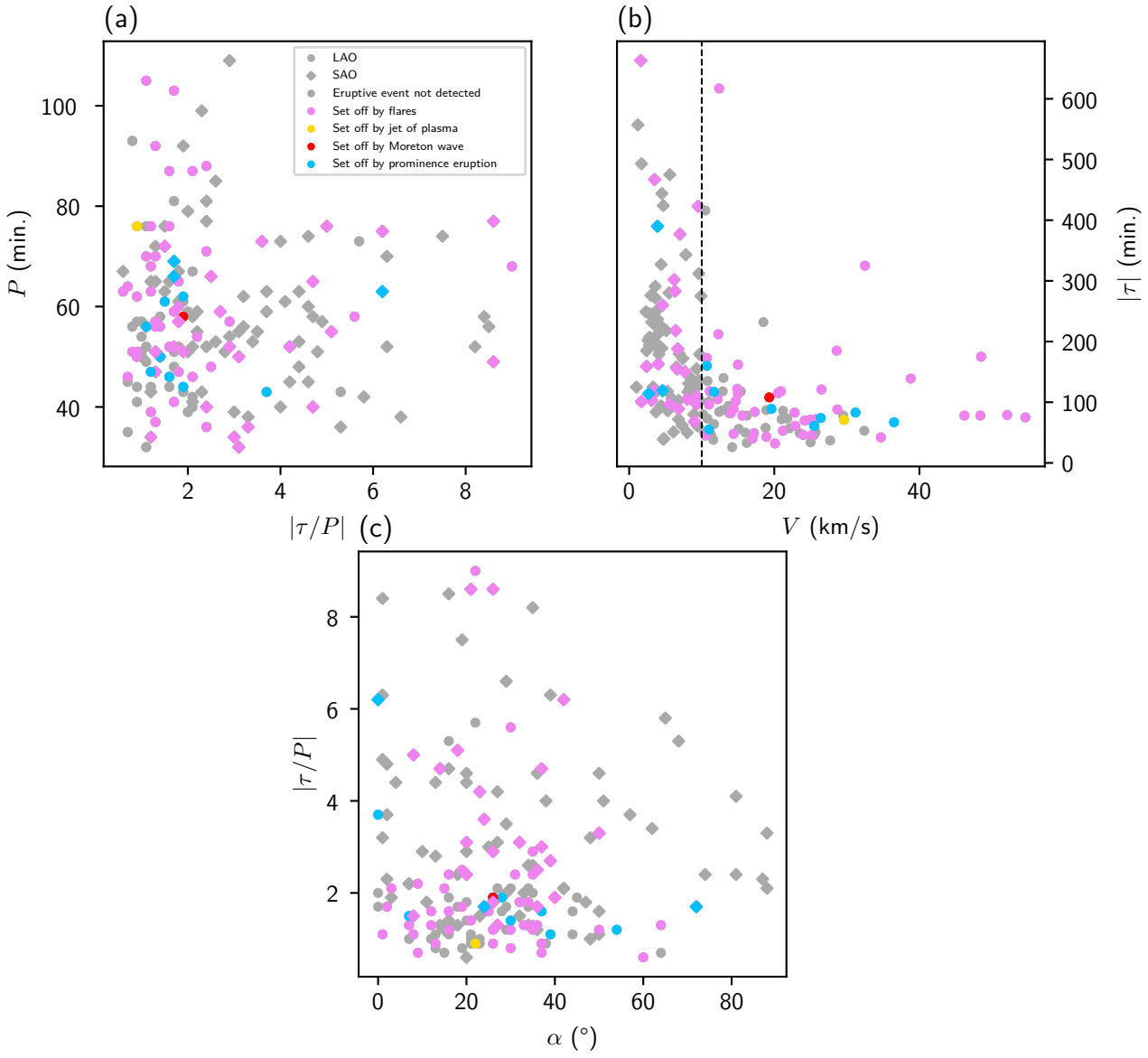

Figure 2.18: Scatter plots of (a) P vs $|\tau/P|$, (b) $|\tau|$ vs V, and (c) $|\tau/P|$ vs α. Filament oscillation events where the trigger is not identified are represented by grey points, while events with associated trigger are represented by different colours (see legend).

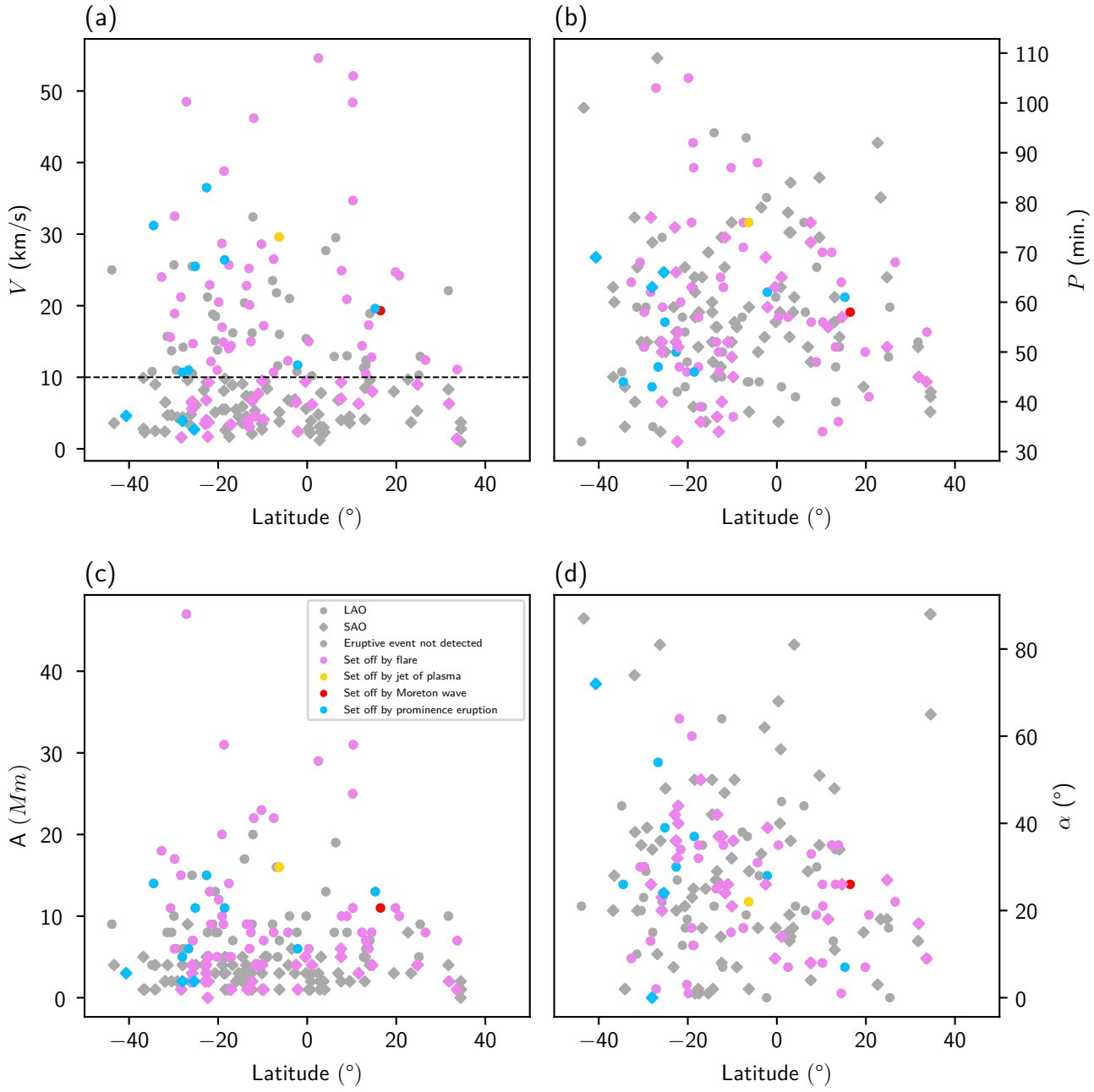

Figure 2.19: Scatter plots of (a) V vs Latitude, (b) P vs Latitude, (c) A vs Latitude, and (d) α vs Latitude. Filament oscillation events where the trigger is not identified are represented by grey points, while events with associated trigger are represented by different colours (see legend).

Chapter 3

Searching for correlation using k-means clustering

Given the nature of this work, it would be interesting to find another way to analyse the filament oscillation events in an attempt to find a possible correlation between their physical properties and the occurrence of highly energetic events.

In this chapter, we explore an approach where we divide the total data in separate clusters, and for each one calculate the percentage of oscillation events that are associated with the eruptive events mentioned previously, to see if a particular set of parameter values would indicate a higher correlation between filament oscillation and eruptive events.

Clustering Method

k-means is an algorithm used to partition data by trying to separate it in k different clusters, such that each data point belongs to the cluster that minimizes the squared Euclidean distance between the data point and the cluster centre, i.e., the centroid. To find the centroid of each cluster it will be necessary to minimize the within-cluster sum-of-squares (SSE):

$$\text{SSE} = \sum_i (\|x_i - \bar{x}\|)^2 \tag{3.1}$$

where x_i are the data points within a cluster, $\bar{x}$ is the centroid (the average point of a cluster).

The k-means algorithm requires the number of clusters, k, to be given *a priori*, so that the algorithm can then choose the ideal centroid positions.

To determine the optimal number of clusters to feed to the algorithm, we used an heuristic called "elbow method" [Tho53]. The elbow method calculates the total SSE, which is the sum of each cluster's SSE, for each $k = 1, 2, 3, \ldots$. Then, these values are plotted. The optimal k number will correspond to the point where the SSE reaches the maximum curvature, after which it will tend to decrease linearly. This is the eponymous "elbow" in the graph.

To determine the number of clusters for the figures in this chapter, we therefore plotted the total SSE vs the number of clusters k, which decrease with increasing k, as expected. Before all this, it was also necessary to scale the data, as a preprocessing step, to guarantee that the performance of the k-means was optimal. Using the package `kneed`, we used the `KneeLocator` algorithm [Sat+11] to identify the elbow point. The code was written in Python 3.

Ideally, the elbow point would be the point after which the plot SSE(k) decreases linearly. However, we noticed that the point suggested by the algorithm was often smaller than the point where this happens. An example of this is given in Figure 3.1, in which we can see that the point suggested by the algorithm, $k = 4$, is smaller than the point where SSE starts to decrease linearly, $k = 6$. Therefore, we manually examined the results for each data set, and adjusted our choice of k accordingly.

After determining k, we run the k-means algorithm, summarised as follows:

Input Input: number of clusters, k.

Step 1 Randomly initialize k centroids from the data points and:

- Assign each data point (from the total data set) to its closest centroid;
- Compute the new centroids given by the mean position of each cluster.

Step 2 Repeat step 1 until the centroid positions stop changing, that is, until convergence.

Output : Centroid positions, i.e. labelled data points according to which cluster they belong to.

The parameters of k-means used in our code are:

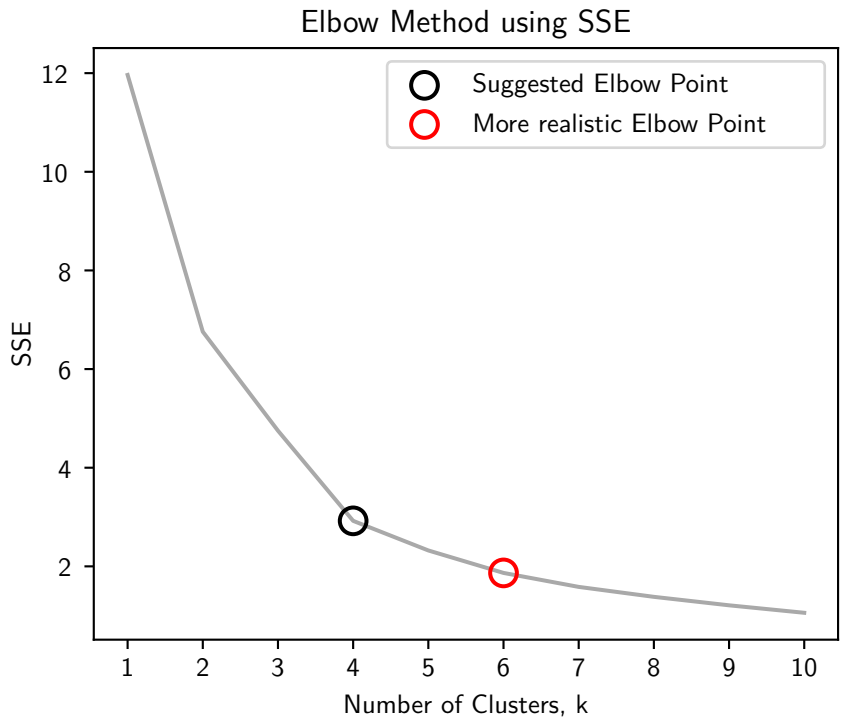

Figure 3.1: Example of usage of elbow method for determining the optimal number of clusters to feed to the k-means algorithm. The black circle indicates the "elbow" suggested by the kneed library (in this case $k = 4$). In this example, the plot does not follow a linear path already after this point, therefore we decided to use $k = 6$ (indicated by the red circle), as a more realistic elbow point in this case.

- `n_clusters`: the number of clusters to generate.
- `init`: the centres of the clusters are randomly chosen from the data set.
- `n_init`: number of times the k-means will run with different centroid seeds.
- `max_iter`: maximum number of iterations of the k-means algorithm for a single run.
- `random_state`: determines random number generation for centroid initialization.

3.1 Results and Discussion

In this final section (Figures 3.2, 3.3, 3.4 and 3.5) we will discuss the results obtained by applying the k-means algorithm to the data obtained by Luna et al. [Lun+14].

We will be focusing on the above figures and also on Table 3.1, which summarises, for each scatter plot, the total number of events in each cluster, the total number of oscillation events that were onset after an eruptive event was detected, and the percentage of oscillations in each cluster that were triggered by the eruptive agents.

In this section, all triggering sources (flares, prominence eruptions, Moreton waves and jets of plasma) were globally designated as eruptive events. The oscillations triggered by eruptive events are represented by a circle with a white cross, while the events where no triggering cause was identified are represented by a full circle. The different clusters are distinguished via different colours.

Period, Velocity, Amplitude and $|\tau|$ vs α

Regarding Figure 3.2a, the obtained values show that no cluster appears to have a preferable set of parameters for the occurrence of eruptive events. We also note that, in the particular case of the red cluster, only 21.43% of events in that cluster were triggered by eruptive events. We conclude that the region of high α and a wide range of periods, represented by the red cluster is, in comparison to the others, particularly unfavourable for the occurrence of events triggered by eruptive agents.

Looking at Figure 3.2b, we see that in the green cluster 88.89% of oscillations were onset by an eruptive event. This green cluster is in a region of high peak velocity amplitude $V > 30\,\mathrm{km\,s^{-1}}$ and of longitudinal oscillations $\alpha < 40°$. The orange cluster, with slightly lower V, also shows a good number of events with eruptive origin, 62.79%, while the remaining clusters have smaller percentages. These results confirm that, as discussed before (see section 2.2), filaments with higher V and lower α seem to have a stronger association with eruptive events.

In Figure 3.2c, we see that 100% of cases in the brown cluster, and 66.67% in the violet cluster, were triggered by eruptive events (although the brown cluster contains only a very small number of events). These clusters exist in a region of high A and small α. This confirms the observations made in

chapter 2. In the remaining clusters the percentages are much smaller than in these two (see Table 3.1).

In Figure 3.2d, we see that in the blue cluster only 23.53% of oscillations were caused by eruptive events, indicating that transversal and non-damped oscillations are less likely to be caused by eruptive events.

Period vs Amplitude, Velocity, Length and Width

In Figure 3.3a, we see that 100% of cases in the violet cluster were onset by eruptive events. In the remaining clusters, the percentages do not surpass 40% in any cluster. This graph indicates that oscillations with periods greater than 55 min and with amplitudes of maximum displacement greater than 23 Mm are more likely to have been caused by eruptive events.

In Figure 3.3b, we observe that in the red cluster all oscillations were caused by eruptive events, corresponding to a region of high peak velocity amplitude and a wide range of periods.

In Figure 3.3c, we see that the orange cluster holds the highest percentage of oscillations onset by eruptive events, 61.54%, which is a region of long filaments with long periods. The lowest percentage is found in the violet cluster, with 35.48%. The variation between clusters is not very significant.

In Figure 3.3d, we see that two clusters, orange and violet, characterized by higher width in comparison to the rest, are the ones with lowest percentage of events unset by eruptive events, with 25.53% and 15.38% respectively.

Period vs $|\tau/P|$, $|\tau|$ vs Velocity, $|\tau/P|$ vs α

From Figure 3.4a, no significant differences were observed between the clusters.

In Figure 3.4b, we see that 100% and 60% of events in the red and green clusters, respectively (in the LAO regime), were triggered by eruptive events, while in the clusters located to their left (in the SAO regime) display lower percentages. This seems to indicate that there is a tendency for events with greater V and lower $|\tau|$ to be associated with eruptive events.

In Figure 3.4c, again no major differences were found between the clusters.

Velocity vs Latitude, Period vs Latitude, Amplitude vs Latitude, α vs Latitude

In Figure 3.5a, we observed that in the orange cluster 72.73% of events were caused by eruptive events, while in the rest of the clusters no percentage is greater than 45%. The orange cluster occupies the zone of highest V, in a narrow band of latitudes. This is exactly the region where most active regions are located, thus where most eruptive events like flares and CMEs occur and disturb structures such as filaments.

In Figure 3.5b, we observe that no group seems to be particularly favourable for the occurrence of oscillations triggered by eruptive events, since the maximum percentage occurs in the red cluster with 55%.

In Figure 3.5c, we see that in the orange cluster 75% of oscillations were triggered by an eruptive event, while the percentages in the remaining clusters reach a maximum of 46.43% in the blue cluster. The orange cluster is the cluster of oscillations with largest amplitudes, and is once again restricted to a narrow band of latitudes, around the equator.

In Figure 3.5d, we that the percentages are generally close to 50%, being the smallest one 38.89%. Therefore, we cannot discern any significant result.

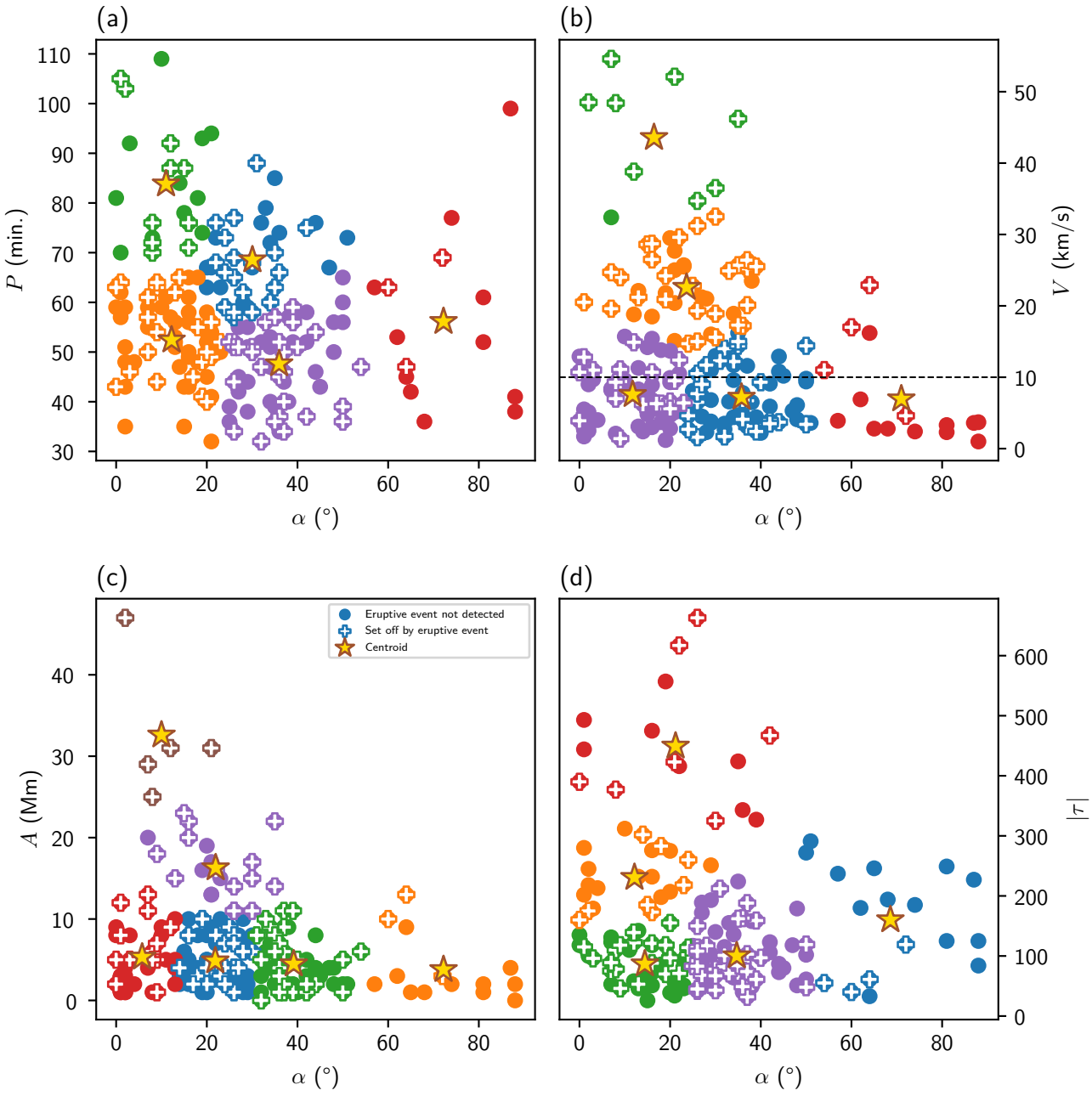

Figure 3.2: Scatter plots of (a) P vs α, (b) V vs α, (c) A vs α, and (d) $|\tau|$ vs α. Each different colour illustrates a different k-means cluster. Filled points are oscillation events where no eruptive event was identified, and points with a white cross are events where the probable triggering agent was identified as an eruptive event. For each cluster, the centroid is pictured with a star.

		Total / total eruptive / % eruptive		
		Green	Red	Blue
Fig 3.2	(a) P vs α	22 / 11 / 50.00%	14 / 3 / 21.43%	35 / 19 / 54.29%
	(b) V vs α	9 / 8 / 88.89%	15 / 4 / 26.67%	65 / 27 / 41.54%
	(c) A vs α	56 / 26 / 46.43%	37 / 13 / 35.14%	63 / 24 / 38.10%
	(d) $\lvert\tau\rvert$ vs α	52 / 21 / 40.38%	15 / 7 / 46.67%	17 / 4 / 23.53%
Fig 3.3	(a) P vs A	38 / 22 / 57.89%	10 / 4 / 40.00%	79 / 28 / 35.44%
	(b) P vs V	43 / 24 / 55.81%	11 / 11 / 100.00%	74 / 26 / 35.14%
	(c) P vs L	35 / 18 / 51.43%	54 / 23 / 42.49%	32 / 14 / 43.75%
	(d) P vs W	60 / 32 / 53.33%	55 / 26 / 47.27%	21 / 13 / 61.90%
Fig 3.4	(a) P vs $\lvert\tau/P\rvert$	60 / 25 / 41.67%	37 / 12 / 32.43%	13 / 5 / 38.46%
	(b) $\lvert\tau\rvert$ vs V	40 / 24 / 60.00%	9 / 9 / 100.00%	76 / 29 / 38.16%
	(c) $\lvert\tau/P\rvert$ vs α	10 / 3 / 30.00%	21 / 8 / 38.10%	8 / 3 / 37.50%
Fig 3.5	(a) V vs Latitude	46 / 18 / 39.13%	52 / 18 / 34.62%	58 / 26 / 44.83%
	(b) P vs Latitude	18 / 7 / 38.89%	20 / 11 / 55.00%	57 / 21 / 36.84%
	(c) A vs Latitude	50 / 20 / 40.00%	60 / 23 / 38.33%	56 / 26 / 46.43%
	(d) α vs Latitude	18 / 7 / 38.89%	46 / 19 / 41.30%	21 / 9 / 42.86%

		Total / total eruptive / % eruptive		
		Violet	Orange	Brown
Fig 3.2	(a) P vs α	62 / 30 / 48.39%	63 / 22 / 34.92%	—
	(b) V vs α	64 / 19 / 29.69%	43 / 27 / 62.79%	—
	(c) A vs α	21 / 14 / 66.67%	14 / 3 / 21.43%	5 / 5 / 100.00%
	(d) $\lvert\tau\rvert$ vs α	69 / 36 / 52.17%	22 / 8 / 36.36%	—
Fig 3.3	(a) P vs A	9 / 9 / 100.00%	60 / 22 / 36.67%	—
	(b) P vs V	62 / 30 / 48.39%	59 / 21 / 35.59%	—
	(c) P vs L	62 / 22 / 35.48%	13 / 8 / 61.54%	—
	(d) P vs W	13 / 2 / 15.38%	47 / 12 / 25.53%	—
Fig 3.4	(a) P vs $\lvert\tau/P\rvert$	15 / 6 / 40.00%	50 / 28 / 56.00%	—
	(b) $\lvert\tau\rvert$ vs V	13 / 8 / 21.05%	12 / 6 / 50.00%	—
	(c) $\lvert\tau/P\rvert$ vs α	13 / 3 / 23.08%	56 / 22 / 39.29%	67 / 37 / 55.22%
Fig 3.5	(a) V vs Latitude	18 / 7 / 38.89%	22 / 16 / 72.73%	—
	(b) P vs Latitude	50 / 24 / 48.00%	51 / 22 / 43.14%	—
	(c) A vs Latitude	18 / 7 / 38.89%	12 / 9 / 75.00%	—
	(d) α vs Latitude	50 / 24 / 48.00%	61 / 26 / 42.62%	—

Table 3.1: Table with total events, total events related to eruptive events and respective percentage that occur in each cluster.

Figure 3.3: Scatter plots of (a) P vs A, (b) P vs V, (c) P vs L, and (d) P vs W. Each different colour illustrates a different k-means cluster. Filled points are oscillation events where no eruptive event was identified, and points with a white cross are events where the probable triggering agent was identified as an eruptive event. For each cluster, the centroid is pictured with a star.

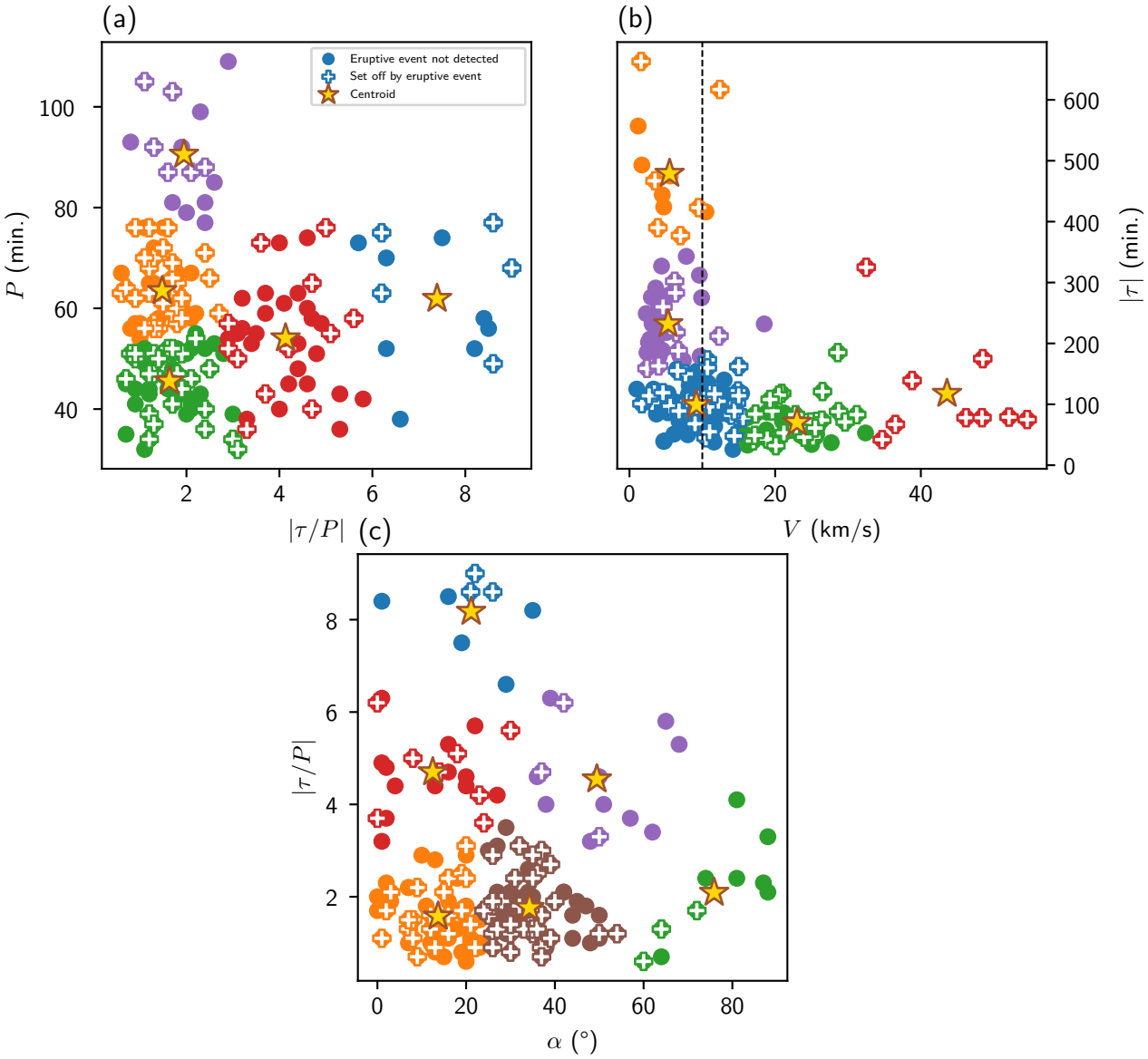

Figure 3.4: Scatter plots of (a) P vs $|\tau/P|$, (b) $|\tau|$ vs V, and (c) $|\tau/P|$ vs α. Each different colour illustrates a different k-means cluster. Filled points are oscillation events where no eruptive event was identified, and points with a white cross are events where the probable triggering agent was identified as an eruptive event. For each cluster, the centroid is pictured with a star.

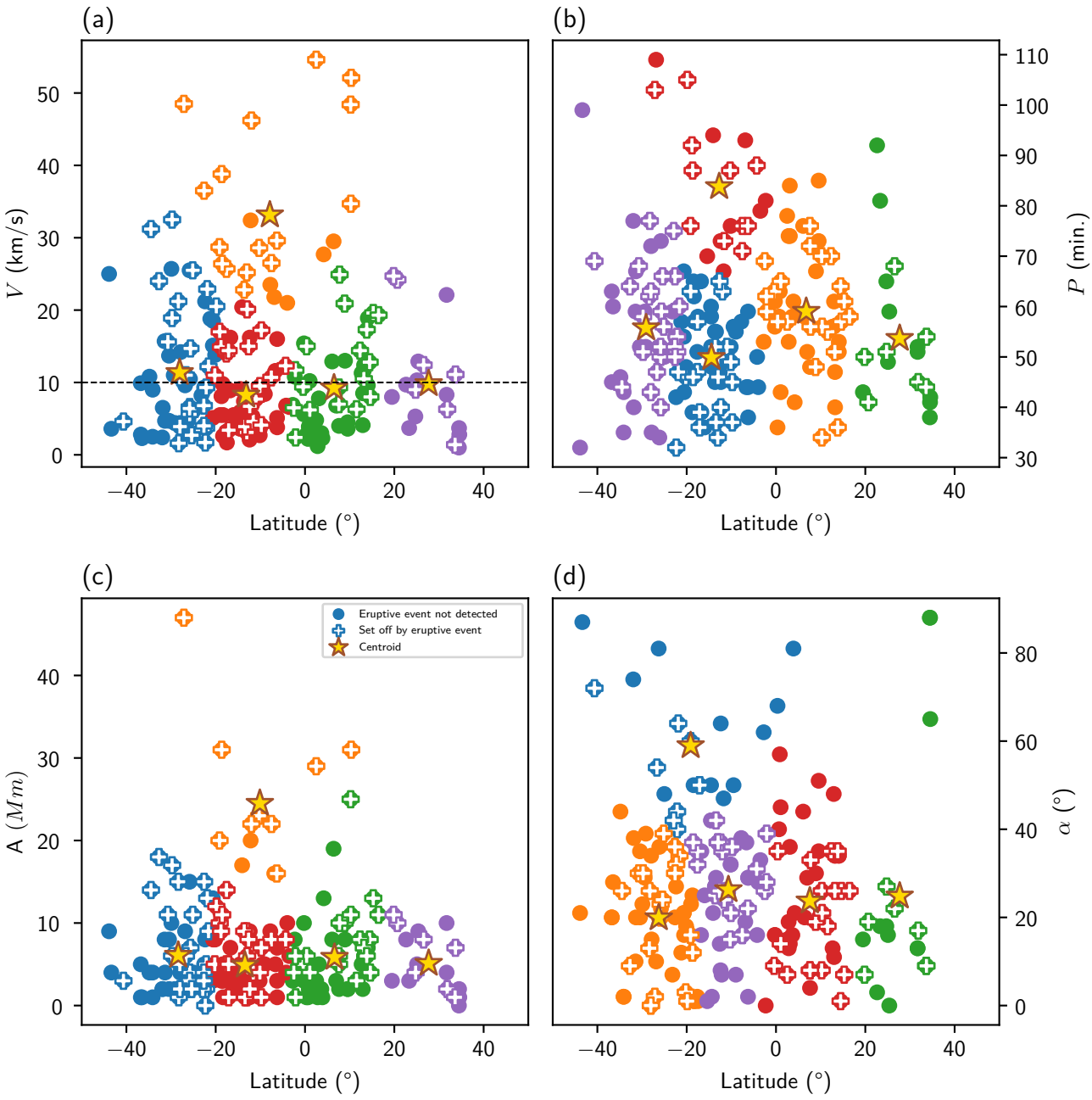

Figure 3.5: Scatter plots of (a) V vs Latitude, (b) P vs Latitude, (c) A vs Latitude, and (d) α vs Latitude. Each different colour illustrates a different k-means cluster. Filled points are oscillation events where no eruptive event was identified, and points with a white cross are events where the probable triggering agent was identified as an eruptive event. For each cluster, the centroid is pictured with a star.

Chapter 4

Conclusion and future work

During this work we have studied the various relations between the parameters of 196 events of filament oscillations, obtained by Luna et al. [Lun+18b] between 1 January 2014 and 30 June 2014, during the solar 24-cycle.

We observed that period maximums tend to decrease with increasing α, and this trend is shared by all types of events, with respect to the position in the Sun where filament oscillations occur.

Relating the peak velocity amplitudes, V, the maximum displacement amplitudes, A, and the period of oscillation, P, with the angle α, we identified a clear threshold given by $\alpha \approx 40°$, which motivated a separation between filament oscillations with $\alpha < 40°$ (longitudinal), in which the motion is directed along the local magnetic field, and another group with $\alpha > 40°$ (transverse). We confirmed that these observations are in agreement with the literature and concluded that longitudinal oscillations tend to have longer periods than transversal. As expected, taking into account that events with very large V were not detected, we confirmed that events with small P and large A did not occur, respecting the relation $V \propto A/P$.

No correlation between P and L was found, in contrary to some other observations in the literature, but we did find a positive linear correlation between P and W. We were also able to confirm that $|\tau|$ and V follow a power law with exponent ≈ 0.31.

Regarding the relationship between the filaments' properties and their latitudes, we confirmed that events that typically occur in active regions, that is, closer to the equator, display greater peak velocity amplitudes and greater maximum amplitude displacements.

Regarding the study of the relation between the filament parameters and eruptive events using k-means clustering, presented in chapter 3, we were able to identify some common features.

Namely, we have observed that those oscillations which were triggered by energetic eruptive events are mainly associated with filaments that show: long displacement amplitudes A, high velocity amplitude V and are longitudinal ($\alpha < 40°$). Filaments with both long periods, and high oscillation amplitudes, or long periods and high peak velocity amplitudes, are also more likely to have been triggered by eruptive events. Long filaments with long periods, seem to have a slightly bigger chance to have been set off by eruptive events, while very thick filaments with long periods show the opposite trend.

We also noted that filament oscillations displaying strong damping and high V were noted to have been triggered by eruptive events. In chapter 2, we discussed the mechanisms which were most likely responsible for this.

We have seen that non-damped or weakly damped oscillations, which have $\alpha > 40°$, must often be caused by other mechanisms, other than energetic eruptive events.

The trends between the physical properties of filaments and their latitudes in the Sun, with respect to their trigger agent, were also as expected, noting that these events occur mainly in Maunder's belt, where the majority of the solar activity occurs, i.e., their triggering agents. One interesting find was how oscillation events caused by prominence eruptions were mostly contained in the southern hemishere, between $-18°$ and $-40°$. The physical explanation behind this observation was not yet found, although we must say it makes for a good mistery.

Regarding future work, it would be interesting to explore more aspects of filament oscillations that would allow further comprehension of their nature and their relationship with eruptive events.

The first would be to gather, for instance through Doppler shift data, information about the line of sight velocity component of the oscillation, not only the transversal component, as the one estimated in the original manuscript. This additional information might impact the correlation between that parameter and the eruptive events in unforeseen ways.

Secondly, given that the catalogue in which we based our discussion corresponds to part of the cycle (only six months) rather than of one complete

solar cycle, the conclusions reached regarding the filaments' latitudes do not take into account their migration of appearance along the cycle. An even more complete catalogue would allow us to understand better how much these conclusions are a consequence of the filaments' nature, and how much is solely a consequence of their migration.

Appendix A

Data tables

The data-set parameters by Luna et al. [Lun+18b] can be found in the following pages. The notation used is summarised in the following table:

Time_{obs}	Observation time
Tel.	Telescope: Learmonth (L), Udaipur (U), El Teide (T), Cerro Tololo (C), Big Bear (B), or Mauna Loa (M)
Pos_x	x-coordinate in the Heliocentric-Cartesian system
Pos_y	y-coordinate in the Heliocentric-Cartesian system
Type	Vial and Engvold filament position type: active region (AR), intermediate (IT), or quiescent (QS)
L	Filament length
W	Filament width
Trigger	Likely trigger event: nearby intense $H\alpha$ brightening (Flare), nearby prominence eruption (PE), hit by jet of plasma (Jet), or Moreton wave (MW)
Erupts	Whether the filament erupts or not
$\text{Time}_{\text{start}}$	Fit start time
α	Angle between oscillation direction and filament spine
P	Period of oscillation
τ	Damping time
τ/P	Period/damping time ratio
A	Displacement amplitude
V	Maximum velocity amplitude

We note that there are two distinct timestamps for each filament. Time_{obs} is the time when the telescope detected an oscillation of the filament, however

this does not necessarily mean that that was the time when the oscillation started. $\text{Time}_{\text{start}}$, is the time when the fit for the oscillation parameters begins (as mentioned in page 24, this was the time when the filament was stable enough to make the slit coincide with its spine). For example, in event 1, the fit starts at 1-Jan-2014 13:50, but the telescope only detected the oscillation at 16:50.

Note also that in the first column, the asterisk denotes an oscillation that occurs on the same filament as the previous event.

Event #	Time_{obs}	Tel.	Pos_x	Pos_y	Type	L (Mm)	W (Mm)	Trigger	Erupts
1	1-Jan-2014 16:50	C	−18	−76	IP	269	15	Flare	—
2*	1-Jan-2014 16:50	C	−18	−76	IP	269	15	Flare	—
3	4-Jan-2014 22:04	B	−251	302	IP	172	7	Flare	—
4	5-Jan-2014 17:03	C	−399	48	IP	87	14	Flare	—
5	5-Jan-2014 17:03	C	−308	−116	AR	240	13	—	—
6*	5-Jan-2014 17:03	C	−308	−116	AR	240	13	—	—
7	5-Jan-2014 17:03	C	730	−430	QS	139	10	PE	—
8*	5-Jan-2014 17:03	C	730	−430	QS	139	10	PE	—
9	5-Jan-2014 22:11	B	806	−79	IP	206	11	—	—
10	6-Jan-2014 08:59	U	84	492	QS	44	9	Flare	—
11	6-Jan-2014 07:11	U	−132	−261	IP	185	8	—	—
12	6-Jan-2014 16:56	C	−268	−466	QS	102	8	—	—
13	6-Jan-2014 16:56	C	−184	57	AR	78	12	—	—
14*	6-Jan-2014 16:56	C	−184	57	AR	78	12	—	—
15	6-Jan-2014 08:59	U	57	304	IP	119	8	Flare	—
16	7-Jan-2014 09:13	U	−335	78	IP	387	13	Flare	—
17	7-Jan-2014 09:13	U	−325	−282	IP	190	7	Flare	—
18	7-Jan-2014 09:13	U	143	−370	IP	445	8	—	—
19	7-Jan-2014 16:58	C	−100	−501	QS	143	12	PE	—
20	8-Jan-2014 08:59	U	−139	−316	IP	313	14	PE	—
21	8-Jan-2014 08:59	U	8	−494	IP	187	10	—	—
22*	8-Jan-2014 08:59	U	8	−494	IP	187	10	—	—
23	8-Jan-2014 08:59	U	260	−367	IP	543	9	Flare	—
24	9-Jan-2014 17:10	C	155	−306	IP	287	20	Flare	—
25	9-Jan-2014 17:10	C	242	−505	IP	303	12	—	—
26	10-Jan-2014 14:03	T	433	80	IP	54	9	—	—
27	11-Jan-2014 16:43	C	815	−393	IP	221	9	PE	—
28	15-Jan-2014 20:00	B	502	−217	AR	125	6	—	—
29	16-Jan-2014 07:37	U	268	125	AR	80	15	—	—
30	16-Jan-2014 19:59	B	−624	−298	IP	228	9	—	—
31	24-Jan-2014 17:00	C	−311	−385	IP	281	10	Flare	—
32	24-Jan-2014 19:11	M	284	−151	IP	394	14	—	—
33	25-Jan-2014 07:40	U	−184	−376	IP	251	8	—	—
34	25-Jan-2014 16:41	C	−110	−129	AR	163	10	Flare	—
35*	25-Jan-2014 16:41	C	−110	−129	AR	163	10	Flare	—
36	25-Jan-2014 16:41	C	508	−95	IP	527	15	Flare	—
37	26-Jan-2014 08:27	U	850	99	IP	81	8	—	—
38	27-Jan-2014 16:41	C	335	−142	AR	255	9	—	—
39*	27-Jan-2014 16:41	C	335	−142	AR	255	9	—	—
40	27-Jan-2014 16:41	C	449	−402	IP	209	17	—	—
41	28-Jan-2014 20:23	B	635	−420	IP	247	9	—	—
42	29-Jan-2014 07:23	U	445	−304	IP	82	11	—	—

Event #	Time_{obs}	Tel.	Pos_x	Pos_y	Type	L (Mm)	W (Mm)	Trigger	Erupts
43	29-Jan-2014 16:49	C	556	−428	IP	251	9	—	—
44	29-Jan-2014 19:59	B	−822	11	IP	182	11	Flare	—
45	30-Jan-2014 07:23	U	702	33	IP	195	9	PE	—
46	31-Jan-2014 15:20	C	−557	16	IP	201	15	—	—
47	1-Feb-2014 07:17	U	−404	58	AR	317	9	Flare	—
48	5-Feb-2014 17:07	C	−812	−129	IP	206	10	Flare	Y
49	5-Feb-2014 17:07	C	−212	−269	IP	205	10	Flare	—
50	6-Feb-2014 17:05	C	−626	−433	IP	363	13	Flare	—
51	6-Feb-2014 17:05	C	−388	−266	IP	231	10	Flare	—
52	7-Feb-2014 13:24	T	−506	243	IP	111	6	—	—
53	8-Feb-2014 20:10	B	428	−271	AR	211	9	Flare	—
54	8-Feb-2014 13:24	T	−193	114	IP	84	16	—	—
55	8-Feb-2014 13:24	T	−122	−162	AR	181	8	—	—
56	9-Feb-2014 16:52	C	−82	−93	IP	162	11	Flare	—
57	9-Feb-2014 16:52	C	−192	−119	IP	109	8	Flare	—
58	9-Feb-2014 16:52	C	−390	−197	AR	232	7	Flare	—
59	11-Feb-2014 17:39	C	517	−203	AR	101	9	Flare	—
60	12-Feb-2014 13:28	T	368	297	AR	184	8	Flare	—
61	12-Feb-2014 19:42	B	571	−105	IP	160	14	Flare	—
62	13-Feb-2014 17:05	C	601	238	AR	236	6	Flare	—
63	13-Feb-2014 20:04	B	708	−382	QS	721	33	Flare	—
64	14-Feb-2014 13:27	T	723	248	AR	295	9	Flare	—
65	14-Feb-2014 19:34	B	−592	−233	IP	805	8	Flare	—
66	16-Feb-2014 19:51	B	−17	−93	AR	132	7	Flare	—
67	17-Feb-2014 07:28	U	−110	−202	IP	898	14	Flare	—
68	17-Feb-2014 18:52	B	3	−199	IP	1051	13	—	—
69	19-Feb-2014 19:47	B	380	−215	IP	913	13	Flare	—
70	22-Feb-2014 07:28	U	−16	−378	IP	359	9	—	—
71	23-Feb-2014 16:55	C	−448	277	AR	120	12	Flare	—
72	24-Feb-2014 16:59	C	44	−311	IP	219	22	—	—
73	24-Feb-2014 16:59	C	330	−267	IP	200	10	—	—
74	25-Feb-2014 16:38	C	548	−213	IP	447	7	—	—
75	25-Feb-2014 16:38	C	366	−172	AR	114	8	—	—
76	25-Feb-2014 16:38	C	526	144	QS	46	12	—	Y
77	27-Feb-2014 13:22	T	−1	164	IP	209	9	Flare	—
78	27-Feb-2014 16:57	C	−203	350	IP	147	9	—	—
79*	27-Feb-2014 16:57	C	−203	350	IP	147	9	—	—
80	28-Feb-2014 13:22	T	125	−328	QS	813	24	—	—
81	7-Mar-2014 17:16	C	590	−74	IP	437	12	Flare	—
82	12-Mar-2014 07:29	U	−567	−237	IP	210	9	Flare	—
83	14-Mar-2014 16:58	C	−812	265	AR	192	8	Flare	—
84	16-Mar-2014 07:22	U	−539	−213	IP	831	13	PE	—

Event #	Time_{obs}	Tel.	Pos_x	Pos_y	Type	L (Mm)	W (Mm)	Trigger	Erupts
85	20-Mar-2014 16:59	C	−315	−4	IP	242	9	—	—
86	21-Mar-2014 19:21	B	521	347	AR	335	11	PE	—
87	23-Mar-2014 16:54	C	398	0	IP	320	12	Jet	—
88	24-Mar-2014 18:57	B	586	−13	IP	152	9	—	—
89*	24-Mar-2014 18:57	B	586	−13	IP	152	9	—	—
90	28-Mar-2014 18:09	B	683	41	IP	79	18	—	—
91	29-Mar-2014 16:57	C	329	372	IP	120	9	MW	—
92	29-Mar-2014 16:57	C	99	−201	AR	217	6	Flare	—
93	30-Mar-2014 07:10	U	83	−405	IP	95	10	—	—
94	31-Mar-2014 18:49	B	379	−390	IP	289	14	Flare	—
95*	31-Mar-2014 18:49	B	379	−390	IP	289	14	Flare	—
96	7-Apr-2014 18:33	B	522	416	AR	72	6	Flare	—
97	9-Apr-2014 12:42	T	469	216	IP	139	9	Flare	—
98	9-Apr-2014 18:30	M	520	200	AR	111	8	—	Y
99	10-Apr-2014 05:07	L	653	−431	QS	458	18	—	—
100	14-Apr-2014 16:44	C	146	−110	IP	248	10	—	Y
101	17-Apr-2014 05:01	L	−648	−161	IP	531	9	Flare	—
102	17-Apr-2014 05:01	L	297	447	QS	210	20	—	—
103	17-Apr-2014 16:52	C	5	−324	IP	177	8	PE	—
104	17-Apr-2014 16:52	C	731	−150	QS	141	21	—	—
105	19-Apr-2014 04:48	L	602	466	QS	240	17	—	—
106	19-Apr-2014 16:47	C	−185	−125	IP	691	11	Flare	—
107	21-Apr-2014 18:20	B	701	−371	IP	149	7	Flare	Y
108*	21-Apr-2014 18:20	B	701	−371	IP	149	7	Flare	Y
109	22-Apr-2014 16:41	C	61	296	IP	229	6	—	—
110	23-Apr-2014 16:49	C	264	294	IP	270	7	Flare	—
111	24-Apr-2014 07:05	U	−262	−263	AR	197	9	—	—
112	24-Apr-2014 07:05	U	205	148	IP	289	11	—	—
113	25-Apr-2014 07:10	U	424	132	IP	264	14	—	—
114	26-Apr-2014 13:27	T	465	−370	IP	800	14	PE	—
115	1-May-2014 18:11	B	−380	231	IP	290	8	Flare	—
116	1-May-2014 18:11	B	753	−385	IP	428	11	Flare	—
117	1-May-2014 07:10	U	−625	−379	IP	137	12	—	—
118	2-May-2014 07:04	U	−296	190	AR	212	9	Flare	—
119*	2-May-2014 07:04	U	−296	190	AR	212	9	Flare	—
120	2-May-2014 13:42	T	36	−342	IP	173	12	—	—
121	5-May-2014 17:22	B	92	−391	IP	291	8	—	—
122	10-May-2014 06:31	U	−499	417	IP	254	14	—	—
123	10-May-2014 13:07	T	−181	−581	QS	71	19	PE	—
124	11-May-2014 18:06	B	−610	−486	QS	395	13	Flare	—
125	12-May-2014 04:11	L	−142	443	QS	117	15	—	—
126	12-May-2014 04:11	L	77	−22	IP	192	12	Flare	—

Event #	Time_{obs}	Tel.	Pos_x	Pos_y	Type	L (Mm)	W (Mm)	Trigger	Erupts
127	12-May-2014 04:11	L	−494	−634	QS	330	10	—	—
128	12-May-2014 07:21	U	281	−102	IP	96	9	—	—
129	12-May-2014 18:01	M	−346	361	IP	164	14	—	—
130	13-May-2014 18:07	B	323	−26	IP	115	9	—	—
131	13-May-2014 18:07	B	−86	−464	IP	222	18	—	—
132	14-May-2014 07:22	U	413	−626	QS	149	35	—	—
133	15-May-2014 16:43	C	285	142	IP	330	25	—	—
134	16-May-2014 06:47	U	354	197	QS	246	33	—	—
135	16-May-2014 13:07	T	−514	355	IP	142	9	Flare	—
136	17-May-2014 04:54	L	521	−70	IP	202	12	—	—
137	17-May-2014 13:07	T	649	135	QS	175	14	—	—
138	18-May-2014 19:54	B	455	−96	IP	133	13	—	—
139	23-May-2014 12:58	T	−101	240	IP	228	11	—	—
140	23-May-2014 13:07	T	269	−302	IP	292	9	—	—
141	23-May-2014 19:27	B	658	146	QS	164	18	—	—
142	23-May-2014 18:10	B	−577	−192	IP	329	9	Flare	—
143	26-May-2014 03:39	L	243	−432	IP	603	11	Flare	—
144	26-May-2014 17:08	C	743	−32	QS	97	18	—	—
145	26-May-2014 16:45	C	−348	−260	IP	143	10	Flare	—
146*	26-May-2014 16:45	C	−348	−260	IP	143	10	Flare	—
147	27-May-2014 04:26	L	280	−233	AR	121	8	—	—
148	27-May-2014 11:24	T	552	−404	IP	796	9	—	—
149	28-May-2014 04:21	L	−26	−352	AR	219	7	Flare	—
150	29-May-2014 04:37	L	184	−346	AR	183	8	—	—
151	30-May-2014 05:31	L	371	−353	AR	235	11	Flare	—
152*	30-May-2014 05:31	L	371	−353	AR	235	11	Flare	—
153	30-May-2014 11:42	T	765	−153	IP	152	8	Flare	—
154*	30-May-2014 11:42	T	765	−153	IP	152	8	Flare	—
155	1-Jun-2014 04:36	L	692	−354	AR	123	7	Flare	Y
156	2-Jun-2014 13:25	T	291	166	IP	239	19	—	—
157	2-Jun-2014 17:45	B	−203	59	QS	124	19	—	—
158	3-Jun-2014 04:32	L	−85	54	QS	166	15	—	—
159	4-Jun-2014 17:42	B	−628	−55	IP	339	10	—	—
160	5-Jun-2014 13:09	T	97	−236	IP	256	9	—	—
161	5-Jun-2014 19:42	M	−174	404	QS	98	12	—	—
162	6-Jun-2014 13:14	T	323	−235	IP	104	12	—	Y
163	7-Jun-2014 04:45	L	23	−204	IP	108	15	—	—
164	7-Jun-2014 13:09	T	−592	−239	IP	206	9	—	—
165*	7-Jun-2014 13:09	T	−592	−239	IP	206	9	—	—
166	8-Jun-2014 13:09	T	3	205	AR	290	11	—	—
167	8-Jun-2014 17:56	B	−345	−224	IP	355	13	—	—
168	9-Jun-2014 13:11	T	242	212	AR	229	11	—	—

Event #	Time_{obs}	Tel.	Pos_x	Pos_y	Type	L (Mm)	W (Mm)	Trigger	Erupts
169*	9-Jun-2014 13:11	T	242	212	AR	229	11	—	—
170	9-Jun-2014 13:11	T	379	6	IP	326	17	—	—
171	9-Jun-2014 13:11	T	45	−304	AR	166	13	—	—
172*	9-Jun-2014 13:11	T	45	−304	AR	166	13	—	—
173	10-Jun-2014 18:52	M	499	220	AR	73	17	Flare	Y
174	12-Jun-2014 04:33	L	−328	−575	QS	99	12	—	—
175*	12-Jun-2014 04:33	L	−328	−575	QS	99	12	—	—
176	12-Jun-2014 04:46	U	289	−344	IP	176	13	—	—
177*	12-Jun-2014 04:46	U	289	−344	IP	176	13	—	—
178	12-Jun-2014 04:33	L	438	−202	IP	166	11	—	—
179	12-Jun-2014 12:51	T	469	490	QS	196	13	—	—
180*	12-Jun-2014 12:51	T	469	490	QS	196	13	—	—
181	13-Jun-2014 04:30	L	−163	−574	QS	125	16	—	—
182	13-Jun-2014 13:11	T	599	−297	IP	606	19	—	—
183	14-Jun-2014 04:40	L	672	−294	IP	288	13	—	—
184	14-Jun-2014 13:10	T	745	55	IP	23	7	—	—
185	14-Jun-2014 13:10	T	−527	490	QS	58	10	Flare	—
186	15-Jun-2014 17:51	M	−345	512	IP	86	16	Flare	—
187*	15-Jun-2014 17:51	M	−345	512	IP	86	16	Flare	—
188	16-Jun-2014 13:11	T	−836	5	IP	189	15	—	—
189	16-Jun-2014 13:11	T	−214	521	IP	61	14	—	—
190*	16-Jun-2014 13:11	T	−214	521	IP	61	14	—	—
191	17-Jun-2014 17:56	B	−334	−510	QS	116	12	—	—
192	17-Jun-2014 13:12	T	−757	−7	IP	301	13	Flare	—
193	17-Jun-2014 13:12	T	−39	520	IP	119	12	—	—
194	17-Jun-2014 13:12	T	695	385	IP	107	7	Flare	—
195	19-Jun-2014 18:44	M	241	−231	IP	131	13	—	—
196	29-Jun-2014 16:50	C	130	−200	IP	691	21	—	—

Event #	$\text{Time}_{\text{start}}$	α (°)	P (min)	τ (min)	τ/P	A (Mm)	V ($\mathrm{km\,s^{-1}}$)
1	1-Jan-2014 13:50	16	76 ± 2	121 ± 15	1.6 ± 0.2	22 ± 2	26.5 ± 3.6
2*	1-Jan-2014 18:56	16	71 ± 3	173 ± 107	2.4 ± 2.0	8 ± 3	10.7 ± 7.0
3	4-Jan-2014 20:30	26	57 ± 2	105 ± 33	1.8 ± 0.6	4 ± 1	8.0 ± 3.5
4	5-Jan-2014 11:43	9	63 ± 4	—	—	5 ± 3	9.4 ± 9.2
5	5-Jan-2014 12:01	32	52 ± 1	—	—	1 ± 1	2.7 ± 6.0
6*	5-Jan-2014 17:05	32	76 ± 3	-115 ± 38	-1.5 ± 0.6	3 ± 1	3.5 ± 6.0
7	5-Jan-2014 10:44	0	63 ± 3	-390 ± 545	-6.2 ± 9.0	2 ± 1	3.9 ± 6.7
8*	5-Jan-2014 21:31	0	43 ± 3	160 ± 329	3.7 ± 8.0	5 ± 3	10.7 ± 11.1
9	5-Jan-2014 20:13	37	44 ± 2	38 ± 9	0.9 ± 0.2	5 ± 2	11.6 ± 6.2
10	6-Jan-2014 06:58	22	68 ± 1	617 ± 367	9.0 ± 5.0	8 ± 1	12.4 ± 1.9
11	6-Jan-2014 08:02	23	63 ± 2	94 ± 23	1.5 ± 0.4	4 ± 1	5.5 ± 3.8
12	6-Jan-2014 11:07	38	40 ± 3	158 ± 141	4.0 ± 4.0	2 ± 1	6.5 ± 7.9
13	6-Jan-2014 12:27	16	61 ± 1	118 ± 18	1.9 ± 0.3	10 ± 1	15.4 ± 2.1
14*	6-Jan-2014 16:26	16	56 ± 6	475 ± 1313	8.5 ± 20.0	3 ± 2	5.6 ± 11.5
15	6-Jan-2014 06:45	1	64 ± 1	—	—	8 ± 1	12.8 ± 1.7
16	7-Jan-2014 05:58	14	65 ± 2	302 ± 158	4.7 ± 3.0	4 ± 1	6.2 ± 3.6
17	7-Jan-2014 04:04	3	46 ± 1	96 ± 24	2.1 ± 0.5	5 ± 1	11.0 ± 4.3
18	7-Jan-2014 04:45	23	50 ± 1	46 ± 5	0.9 ± 0.1	15 ± 2	25.5 ± 4.7
19	7-Jan-2014 14:16	26	44 ± 1	83 ± 8	1.9 ± 0.2	14 ± 2	31.2 ± 4.5
20	8-Jan-2014 05:47	30	50 ± 2	67 ± 15	1.4 ± 0.3	15 ± 3	36.5 ± 8.8
21	8-Jan-2014 04:49	2	43 ± 2	100 ± 45	2.3 ± 1.0	4 ± 1	9.0 ± 4.7
22*	8-Jan-2014 08:18	2	35 ± 2	—	—	1 ± 1	2.5 ± 9.3
23	8-Jan-2014 03:28	24	59 ± 1	102 ± 14	1.7 ± 0.2	7 ± 1	14.7 ± 2.9
24	9-Jan-2014 16:56	40	51 ± 2	97 ± 29	1.9 ± 0.6	5 ± 2	9.3 ± 5.7
25	9-Jan-2014 12:31	44	46 ± 3	73 ± 33	1.6 ± 0.8	4 ± 2	10.8 ± 7.5
26	10-Jan-2014 11:23	45	43 ± 2	80 ± 26	1.9 ± 0.7	3 ± 1	10.2 ± 5.5
27	11-Jan-2014 12:37	24	66 ± 3	114 ± 51	1.7 ± 0.8	2 ± 1	2.7 ± 7.5
28	15-Jan-2014 17:38	35	39 ± 1	78 ± 13	2.0 ± 0.3	7 ± 2	16.2 ± 5.8
29	16-Jan-2014 08:29	13	53 ± 2	232 ± 168	4.4 ± 3.0	2 ± 1	3.1 ± 5.4
30	16-Jan-2014 20:46	12	57 ± 2	58 ± 10	1.0 ± 0.2	9 ± 2	18.8 ± 6.1
31	24-Jan-2014 17:17	26	77 ± 4	663 ± 1546	8.6 ± 20.0	1 ± 1	1.6 ± 9.5
32	24-Jan-2014 21:00	21	94 ± 2	—	—	17 ± 2	20.4 ± 3.5
33	25-Jan-2014 07:16	34	72 ± 2	94 ± 20	1.3 ± 0.3	4 ± 1	4.4 ± 3.0
34	25-Jan-2014 12:19	37	34 ± 3	103 ± 185	3.0 ± 6.0	1 ± 1	3.1 ± 12.9
35*	25-Jan-2014 14:47	37	50 ± 2	46 ± 6	0.9 ± 0.1	9 ± 2	25.2 ± 6.5
36	25-Jan-2014 16:06	15	87 ± 1	185 ± 26	2.1 ± 0.3	23 ± 2	28.6 ± 3.1
37	26-Jan-2014 08:09	36	74 ± 1	343 ± 117	4.6 ± 2.0	5 ± 1	7.8 ± 2.7
38	27-Jan-2014 14:28	27	45 ± 3	-189 ± 216	-4.2 ± 5.0	2 ± 1	4.5 ± 10.7
39*	27-Jan-2014 20:02	27	55 ± 2	172 ± 112	3.1 ± 2.0	4 ± 1	7.4 ± 5.2
40	27-Jan-2014 16:04	39	52 ± 1	327 ± 154	6.3 ± 3.0	2 ± 1	4.4 ± 3.8
41	28-Jan-2014 20:14	29	59 ± 3	101 ± 35	1.7 ± 0.6	6 ± 2	11.0 ± 5.1
42	29-Jan-2014 08:23	7	59 ± 2	131 ± 34	2.2 ± 0.6	4 ± 1	8.2 ± 3.2

Event #	$\text{Time}_{\text{start}}$	α (°)	P (min)	τ (min)	τ/P	A (Mm)	V ($\text{km}\,\text{s}^{-1}$)
43	29-Jan-2014 19:36	35	52 ± 2	424 ± 617	8.2 ± 10.0	2 ± 1	4.7 ± 8.1
44	29-Jan-2014 18:35	26	69 ± 2	—	—	4 ± 1	6.5 ± 4.2
45	30-Jan-2014 05:20	28	62 ± 1	117 ± 14	1.9 ± 0.2	6 ± 1	11.7 ± 2.6
46	31-Jan-2014 13:40	28	44 ± 1	72 ± 10	1.6 ± 0.2	10 ± 2	21.0 ± 3.7
47	1-Feb-2014 07:55	39	59 ± 10	159 ± 264	2.7 ± 5.0	1 ± 1	2.4 ± 15.4
48	5-Feb-2014 13:53	26	52 ± 2	150 ± 58	2.9 ± 1.0	4 ± 2	7.7 ± 6.4
49	5-Feb-2014 20:03	44	54 ± 3	—	—	2 ± 1	3.7 ± 8.7
50	6-Feb-2014 16:45	30	68 ± 2	78 ± 13	1.2 ± 0.2	11 ± 2	15.6 ± 4.5
51	6-Feb-2014 17:26	34	60 ± 2	105 ± 20	1.8 ± 0.4	9 ± 2	12.2 ± 4.2
52	7-Feb-2014 09:44	30	67 ± 2	140 ± 29	2.1 ± 0.5	8 ± 2	13.0 ± 3.5
53	8-Feb-2014 21:28	64	47 ± 1	61 ± 5	1.30 ± 0.01	13 ± 1	22.9 ± 2.5
54	8-Feb-2014 10:57	68	36 ± 1	194 ± 140	5.3 ± 4.0	1 ± 1	2.8 ± 5.9
55	8-Feb-2014 10:34	25	36 ± 1	—	—	2 ± 1	5.5 ± 7.0
56	9-Feb-2014 14:10	35	63 ± 1	78 ± 8	1.2 ± 0.1	22 ± 3	46.2 ± 5.0
57	9-Feb-2014 15:04	42	37 ± 1	—	—	1 ± 1	3.9 ± 7.0
58	9-Feb-2014 11:48	32	47 ± 1	82 ± 20	1.8 ± 0.4	5 ± 2	14.0 ± 5.0
59	11-Feb-2014 17:13	35	57 ± 1	72 ± 6	1.30 ± 0.01	14 ± 2	25.7 ± 3.3
60	12-Feb-2014 14:19	18	55 ± 1	283 ± 170	5.1 ± 3.0	3 ± 1	6.3 ± 4.7
61	12-Feb-2014 17:45	24	73 ± 3	260 ± 144	3.6 ± 2.0	4 ± 1	4.6 ± 3.9
62	13-Feb-2014 18:05	19	48 ± 1	118 ± 24	2.5 ± 0.5	10 ± 2	20.9 ± 4.2
63	13-Feb-2014 20:39	2	103 ± 1	175 ± 12	1.7 ± 0.1	47 ± 2	48.5 ± 2.4
64	14-Feb-2014 08:38	21	56 ± 1	79 ± 6	1.4 ± 0.1	31 ± 2	52.1 ± 3.7
65	14-Feb-2014 20:06	60	63 ± 3	-40 ± 7	-0.6 ± 0.1	10 ± 1	17.0 ± 11.5
66	16-Feb-2014 17:26	37	40 ± 2	188 ± 255	4.7 ± 7.0	2 ± 2	6.7 ± 11.9
67	17-Feb-2014 02:42	12	92 ± 3	122 ± 18	1.3 ± 0.2	9 ± 1	14.9 ± 3.1
68	17-Feb-2014 19:59	25	39 ± 3	117 ± 149	3.0 ± 4.0	3 ± 2	8.1 ± 11.6
69	19-Feb-2014 15:38	16	76 ± 2	88 ± 13	1.2 ± 0.2	20 ± 3	28.7 ± 6.1
70	22-Feb-2014 09:04	23	51 ± 2	51 ± 13	1.0 ± 0.3	10 ± 3	25.7 ± 8.2
71	23-Feb-2014 16:04	26	34 ± 1	42 ± 8	1.2 ± 0.2	11 ± 2	34.7 ± 6.1
72	24-Feb-2014 15:03	22	73 ± 1	416 ± 127	5.7 ± 2.0	7 ± 1	10.5 ± 2.9
73	24-Feb-2014 19:13	20	54 ± 2	155 ± 81	2.9 ± 2.0	5 ± 2	9.3 ± 7.9
74	25-Feb-2014 15:23	50	65 ± 2	102 ± 21	1.6 ± 0.3	5 ± 1	9.8 ± 3.5
75	25-Feb-2014 15:28	16	65 ± 3	80 ± 27	1.2 ± 0.5	4 ± 2	8.9 ± 6.5
76	25-Feb-2014 12:37	15	78 ± 2	—	—	3 ± 1	4.8 ± 3.3
77	27-Feb-2014 09:48	7	57 ± 1	75 ± 8	1.3 ± 0.2	29 ± 3	54.6 ± 6.3
78	27-Feb-2014 15:59	34	53 ± 2	136 ± 90	2.6 ± 2.0	4 ± 2	9.6 ± 6.2
79*	27-Feb-2014 19:41	34	51 ± 1	87 ± 20	1.7 ± 0.4	7 ± 2	18.9 ± 5.9
80	28-Feb-2014 12:08	10	109 ± 2	312 ± 106	2.9 ± 1.0	9 ± 2	9.6 ± 2.8
81	7-Mar-2014 16:44	21	49 ± 1	423 ± 345	8.6 ± 7.0	4 ± 1	9.5 ± 3.7
82	12-Mar-2014 09:02	1	105 ± 10	115 ± 52	1.1 ± 0.6	12 ± 3	20.5 ± 11.1
83	14-Mar-2014 13:31	35	70 ± 2	89 ± 14	1.3 ± 0.2	8 ± 2	14.4 ± 3.0
84	16-Mar-2014 03:31	37	46 ± 1	74 ± 15	1.6 ± 0.4	11 ± 2	26.4 ± 5.9

Event #	$\text{Time}_{\text{start}}$	α (°)	P (min)	τ (min)	τ/P	A (Mm)	V ($\text{km}\,\text{s}^{-1}$)
85	20-Mar-2014 16:02	19	93 ± 2	73 ± 8	0.80 ± 0.09	16 ± 2	21.8 ± 3.8
86	21-Mar-2014 17:23	7	61 ± 2	89 ± 25	1.5 ± 0.4	13 ± 2	19.6 ± 5.1
87	23-Mar-2014 16:05	22	76 ± 1	71 ± 5	0.90 ± 0.07	16 ± 2	29.6 ± 3.5
88	24-Mar-2014 19:17	29	44 ± 2	50 ± 8	1.2 ± 0.2	7 ± 1	16.0 ± 4.0
89*	24-Mar-2014 20:57	29	38 ± 2	251 ± 269	6.6 ± 7.0	1 ± 1	3.8 ± 6.5
90	28-Mar-2014 17:52	0	81 ± 3	135 ± 32	1.7 ± 0.4	8 ± 2	10.8 ± 3.9
91	29-Mar-2014 18:23	26	58 ± 1	108 ± 12	1.9 ± 0.2	11 ± 1	19.3 ± 2.3
92	29-Mar-2014 15:50	12	87 ± 2	139 ± 20	1.6 ± 0.3	31 ± 3	38.8 ± 4.4
93	30-Mar-2014 03:53	10	59 ± 5	—	—	8 ± 2	15.7 ± 9.2
94	31-Mar-2014 16:11	30	51 ± 2	43 ± 11	0.8 ± 0.2	6 ± 2	18.9 ± 7.0
95*	31-Mar-2014 19:38	30	58 ± 1	325 ± 62	5.6 ± 1.0	17 ± 2	32.5 ± 2.5
96	7-Apr-2014 21:46	19	41 ± 1	70 ± 9	1.7 ± 0.2	10 ± 1	24.2 ± 2.8
97	9-Apr-2014 11:21	33	56 ± 1	71 ± 11	1.3 ± 0.2	10 ± 2	24.9 ± 4.5
98	9-Apr-2014 18:19	29	51 ± 4	103 ± 110	2.0 ± 2.0	3 ± 2	6.8 ± 10.6
99	10-Apr-2014 06:14	20	52 ± 1	94 ± 13	1.8 ± 0.3	8 ± 1	13.7 ± 2.9
100	14-Apr-2014 12:16	7	50 ± 1	53 ± 4	1.00 ± 0.09	20 ± 2	32.4 ± 2.7
101	17-Apr-2014 05:20	25	52 ± 1	83 ± 8	1.6 ± 0.2	9 ± 1	22.8 ± 2.8
102	17-Apr-2014 02:21	3	92 ± 2	179 ± 35	1.9 ± 0.4	8 ± 1	9.7 ± 2.4
103	17-Apr-2014 17:41	39	56 ± 1	61 ± 7	1.1 ± 0.1	11 ± 2	25.5 ± 3.7
104	17-Apr-2014 18:38	8	73 ± 4	—	—	1 ± 1	2.1 ± 7.4
105	19-Apr-2014 02:57	0	59 ± 2	118 ± 34	2.0 ± 0.6	9 ± 2	12.9 ± 4.4
106	19-Apr-2014 12:44	26	65 ± 1	114 ± 20	1.8 ± 0.3	8 ± 2	15.0 ± 4.3
107	21-Apr-2014 18:20	20	50 ± 1	155 ± 34	3.1 ± 0.7	4 ± 1	6.6 ± 2.2
108*	21-Apr-2014 21:29	20	40 ± 3	-97 ± 70	-2.4 ± 2.0	2 ± 1	5.6 ± 9.3
109	22-Apr-2014 12:17	11	61 ± 1	110 ± 19	1.8 ± 0.3	5 ± 1	8.5 ± 3.4
110	23-Apr-2014 14:32	26	51 ± 4	45 ± 15	0.9 ± 0.3	7 ± 2	10.5 ± 7.4
111	24-Apr-2014 04:04	16	43 ± 1	232 ± 42	5.3 ± 0.1	8 ± 1	18.5 ± 3.3
112	24-Apr-2014 10:53	21	41 ± 2	37 ± 6	0.9 ± 0.1	13 ± 2	27.7 ± 6.2
113	25-Apr-2014 03:17	16	58 ± 2	276 ± 189	4.7 ± 3.0	2 ± 1	3.0 ± 6.4
114	26-Apr-2014 12:40	54	47 ± 3	55 ± 21	1.2 ± 0.5	6 ± 2	11.0 ± 8.7
115	1-May-2014 17:40	8	70 ± 1	78 ± 4	1.10 ± 0.06	25 ± 2	48.4 ± 2.8
116	1-May-2014 16:17	23	52 ± 1	218 ± 103	4.2 ± 2.0	3 ± 1	6.4 ± 4.9
117	1-May-2014 03:08	81	52 ± 2	125 ± 44	2.4 ± 0.9	2 ± 1	3.3 ± 4.8
118	2-May-2014 02:17	8	76 ± 1	377 ± 144	5.0 ± 2.0	6 ± 1	7.0 ± 2.4
119*	2-May-2014 09:08	8	72 ± 5	110 ± 89	1.5 ± 1.0	5 ± 3	9.3 ± 9.8
120	2-May-2014 11:04	48	50 ± 4	51 ± 19	1.0 ± 0.4	4 ± 2	6.1 ± 8.6
121	5-May-2014 16:13	15	35 ± 3	26 ± 8	0.7 ± 0.3	6 ± 2	14.2 ± 9.1
122	10-May-2014 08:01	18	81 ± 3	198 ± 104	2.4 ± 1.0	3 ± 1	3.7 ± 5.8
123	10-May-2014 09:14	72	69 ± 3	119 ± 58	1.7 ± 0.9	3 ± 2	4.6 ± 6.5
124	11-May-2014 18:47	9	64 ± 3	46 ± 8	0.7 ± 0.2	18 ± 3	24.0 ± 5.8
125	12-May-2014 02:40	18	65 ± 6	86 ± 52	1.3 ± 0.9	4 ± 2	5.3 ± 9.1
126	12-May-2014 01:19	31	88 ± 2	212 ± 55	2.4 ± 0.7	8 ± 2	12.3 ± 3.3

Event #	$\text{Time}_{\text{start}}$	α (°)	P (min)	τ (min)	τ/P	A (Mm)	V ($\text{km}\,\text{s}^{-1}$)
127	12-May-2014 06:20	21	32 ± 2	34 ± 9	1.1 ± 0.3	9 ± 3	25.0 ± 9.1
128	12-May-2014 08:22	7	55 ± 2	123 ± 35	2.2 ± 0.7	5 ± 1	8.4 ± 4.0
129	12-May-2014 01:26	15	43 ± 2	50 ± 16	1.2 ± 0.4	3 ± 1	8.0 ± 5.8
130	13-May-2014 18:26	16	50 ± 3	72 ± 25	1.4 ± 0.5	4 ± 1	6.8 ± 5.6
131	13-May-2014 14:46	74	77 ± 2	185 ± 83	2.4 ± 1.0	2 ± 1	2.4 ± 3.5
132	14-May-2014 07:13	87	99 ± 5	227 ± 138	2.3 ± 1.0	4 ± 2	3.6 ± 5.6
133	15-May-2014 18:25	44	76 ± 2	87 ± 12	1.1 ± 0.2	8 ± 1	12.9 ± 2.7
134	16-May-2014 02:25	35	85 ± 5	-224 ± 195	-2.6 ± 2.0	2 ± 1	4.5 ± 9.0
135	16-May-2014 11:49	7	50 ± 1	—	—	11 ± 1	24.7 ± 3.2
136	17-May-2014 02:37	2	59 ± 3	218 ± 219	3.7 ± 4.0	3 ± 2	5.1 ± 7.4
137	17-May-2014 10:35	20	58 ± 2	78 ± 12	1.4 ± 0.2	19 ± 2	29.5 ± 5.1
138	18-May-2014 18:22	38	57 ± 1	49 ± 6	0.9 ± 0.1	9 ± 2	23.5 ± 4.3
139	23-May-2014 15:06	48	56 ± 2	179 ± 111	3.2 ± 2.0	2 ± 1	4.1 ± 5.4
140	23-May-2014 14:58	18	48 ± 2	82 ± 20	1.7 ± 0.4	8 ± 2	13.8 ± 5.2
141	23-May-2014 14:14	4	48 ± 3	213 ± 216	4.4 ± 5.0	2 ± 1	4.0 ± 8.5
142	23-May-2014 18:01	37	46 ± 2	32 ± 7	0.7 ± 0.2	6 ± 2	20.1 ± 7.2
143	26-May-2014 02:38	13	62 ± 2	53 ± 6	0.90 ± 0.01	15 ± 2	21.2 ± 2.8
144	26-May-2014 17:52	62	53 ± 2	180 ± 145	3.4 ± 3.0	3 ± 1	6.9 ± 6.2
145	26-May-2014 13:31	50	39 ± 2	48 ± 13	1.2 ± 0.4	5 ± 2	14.4 ± 6.1
146*	26-May-2014 17:38	50	36 ± 2	119 ± 146	3.3 ± 4.0	1 ± 1	3.4 ± 9.4
147	27-May-2014 03:16	1	70 ± 2	444 ± 385	6.3 ± 6.0	3 ± 1	4.5 ± 5.4
148	27-May-2014 09:16	36	34 ± 3	40 ± 22	1.2 ± 0.7	2 ± 1	4.8 ± 10.0
149	28-May-2014 00:34	42	75 ± 6	467 ± 1263	6.2 ± 20.0	2 ± 2	3.5 ± 9.2
150	29-May-2014 01:16	27	42 ± 1	86 ± 13	2.1 ± 0.3	8 ± 1	21.2 ± 4.3
151	30-May-2014 00:01	36	52 ± 2	89 ± 23	1.7 ± 0.5	4 ± 1	6.8 ± 5.1
152*	30-May-2014 05:37	36	66 ± 3	-163 ± 105	-2.5 ± 2.0	3 ± 1	4.0 ± 7.8
153	30-May-2014 11:43	36	45 ± 12	—	—	1 ± 3	4.1 ± 30.4
154*	30-May-2014 13:42	36	37 ± 3	49 ± 25	1.3 ± 0.7	7 ± 4	17.2 ± 15.4
155	1-Jun-2014 02:06	32	32 ± 13	101 ± 859	3.1 ± 30.0	0 ± 2	1.7 ± 52.6
156	2-Jun-2014 07:05	51	73 ± 3	-291 ± 236	-4.0 ± 3.0	2 ± 1	3.6 ± 5.9
157	2-Jun-2014 18:26	14	84 ± 2	—	—	2 ± 1	2.4 ± 3.9
158	3-Jun-2014 02:33	19	74 ± 7	557 ± 2260	7.5 ± 30.0	1 ± 1	1.2 ± 13.5
159	4-Jun-2014 17:30	33	79 ± 2	155 ± 29	2.0 ± 0.4	6 ± 1	6.6 ± 2.6
160	5-Jun-2014 10:20	50	60 ± 1	272 ± 73	4.6 ± 1.0	2 ± 1	3.6 ± 3.2
161	5-Jun-2014 19:57	16	49 ± 2	51 ± 13	1.1 ± 0.3	5 ± 2	10.3 ± 6.1
162	6-Jun-2014 10:46	2	48 ± 3	—	—	2 ± 1	3.9 ± 7.0
163	7-Jun-2014 00:36	64	45 ± 3	33 ± 9	0.7 ± 0.2	9 ± 3	16.2 ± 13.1
164	7-Jun-2014 07:26	42	52 ± 3	106 ± 62	2.1 ± 1.0	3 ± 1	5.9 ± 6.4
165*	7-Jun-2014 11:26	42	58 ± 2	123 ± 39	2.1 ± 0.7	5 ± 2	9.1 ± 4.9
166	8-Jun-2014 10:17	13	56 ± 5	46 ± 20	0.8 ± 0.4	5 ± 4	11.3 ± 11.9
167	8-Jun-2014 16:55	29	55 ± 3	193 ± 167	3.5 ± 3.0	2 ± 1	3.6 ± 8.0
168	9-Jun-2014 07:32	34	47 ± 2	64 ± 16	1.3 ± 0.4	6 ± 2	11.7 ± 5.2

Event #	$\text{Time}_{\text{start}}$	α (°)	P (min)	τ (min)	τ/P	A (Mm)	V ($\text{km}\,\text{s}^{-1}$)
169*	9-Jun-2014 11:55	34	40 ± 1	84 ± 21	2.1 ± 0.5	6 ± 1	12.4 ± 3.5
170	9-Jun-2014 14:46	40	58 ± 4	—	—	1 ± 1	2.2 ± 17.5
171	9-Jun-2014 09:34	1	62 ± 3	-202 ± 226	-3.2 ± 4.0	1 ± 1	2.6 ± 9.3
172*	9-Jun-2014 13:59	1	57 ± 2	280 ± 189	4.9 ± 3.0	3 ± 1	5.5 ± 5.3
173	10-Jun-2014 18:19	35	36 ± 1	84 ± 20	2.4 ± 0.6	6 ± 1	17.3 ± 4.8
174	12-Jun-2014 00:01	20	63 ± 1	275 ± 118	4.4 ± 2.0	5 ± 1	9.9 ± 3.3
175*	12-Jun-2014 04:31	20	45 ± 1	207 ± 134	4.6 ± 3.0	1 ± 1	2.8 ± 5.1
176	12-Jun-2014 01:50	21	67 ± 3	—	—	3 ± 1	5.1 ± 5.7
177*	12-Jun-2014 05:37	21	54 ± 3	56 ± 35	1.0 ± 0.7	13 ± 5	15.1 ± 9.5
178	12-Jun-2014 00:30	47	67 ± 2	118 ± 31	1.8 ± 0.5	4 ± 1	5.3 ± 5.1
179	12-Jun-2014 13:11	13	52 ± 1	57 ± 8	1.1 ± 0.2	10 ± 2	22.1 ± 5.0
180*	12-Jun-2014 14:10	13	51 ± 1	142 ± 48	2.8 ± 0.1	4 ± 1	8.3 ± 4.1
181	13-Jun-2014 05:38	28	60 ± 5	—	—	1 ± 1	2.3 ± 12.9
182	13-Jun-2014 16:37	2	51 ± 3	245 ± 353	4.8 ± 7.0	1 ± 1	3.2 ± 8.5
183	14-Jun-2014 01:44	1	58 ± 2	493 ± 673	8.4 ± 10.0	1 ± 1	1.7 ± 7.4
184	14-Jun-2014 11:38	81	61 ± 4	249 ± 313	4.1 ± 5.0	1 ± 1	2.3 ± 8.5
185	14-Jun-2014 09:46	17	45 ± 3	—	—	2 ± 2	6.3 ± 10.0
186	15-Jun-2014 02:37	9	44 ± 6	—	—	1 ± 1	1.4 ± 19.3
187*	15-Jun-2014 21:04	9	54 ± 1	118 ± 22	2.2 ± 0.4	7 ± 1	11.1 ± 2.6
188	16-Jun-2014 11:43	57	63 ± 8	237 ± 356	3.7 ± 6.0	2 ± 1	3.9 ± 12.6
189	16-Jun-2014 08:50	88	38 ± 9	125 ± 501	3.3 ± 10.0	0 ± 1	1.0 ± 28.2
190*	16-Jun-2014 15:59	88	41 ± 3	84 ± 67	2.1 ± 2.0	2 ± 1	3.7 ± 10.1
191	17-Jun-2014 21:14	20	67 ± 6	39 ± 9	0.6 ± 0.2	4 ± 2	4.7 ± 7.4
192	17-Jun-2014 15:50	35	57 ± 1	162 ± 51	2.9 ± 0.9	6 ± 2	15.0 ± 4.6
193	17-Jun-2014 09:50	65	42 ± 1	246 ± 166	5.8 ± 4.0	1 ± 1	2.8 ± 4.5
194	17-Jun-2014 12:36	27	51 ± 2	68 ± 16	1.3 ± 0.3	4 ± 1	9.0 ± 4.0
195	19-Jun-2014 18:10	14	47 ± 3	62 ± 21	1.3 ± 0.5	3 ± 1	7.3 ± 5.1
196	29-Jun-2014 16:21	50	56 ± 4	61 ± 28	1.1 ± 0.6	5 ± 3	9.4 ± 10.6

Bibliography

[Ber13] Thomas Berger. 'Solar Prominence Fine Structure and Dynamics'. In: *Proceedings of the International Astronomical Union* 8.S300 (June 2013), pp. 15–29. ISSN: 1743-9213, 1743-9221. DOI: 10.1017/S1743921313010697 (cit. on pp. 15, 31).

[BG10] Arnold O. Benz and Manuel Güdel. 'Physical Processes in Magnetically Driven Flares on the Sun, Stars, and Young Stellar Objects'. In: *Annual Review of Astronomy and Astrophysics* 48.1 (Aug. 2010), pp. 241–287. DOI: 10.1146/annurev-astro-082708-101757 (cit. on p. 1).

[Dod49] Helen W. Dodson. 'Position and Development of the Solar Flares of May 8 and 10, 1949'. In: *The Astrophysical Journal* 110 (Nov. 1949), p. 382. DOI: 10.1086/145214 (cit. on p. 21).

[Dud+08] Jaroslav Dudík et al. 'Topological Departures from Translational Invariance along a Filament Observed by THEMIS'. In: *Solar Physics* 248.1 (Mar. 2008), p. 33. DOI: 10.1007/s11207-008-9155-2 (cit. on p. 14).

[Gos93] John T. Gosling. 'The solar flare myth'. In: *Journal of Geophysical Research: Space Physics* 98.A11 (Nov. 1993), pp. 18937–18949. DOI: 10.1029/93ja01896 (cit. on p. 1).

[Hal+19] George E. Hale et al. 'The magnetic polarity of sun-spots'. In: *Astrophysical Journal* 49 (Apr. 1919), p. 153 (cit. on p. 11).

[KTd03] Therese Kucera, M. Tovar and Bart de Pontieu. 'Prominence Motions Observed at High Cadences in Temperatures from 10 000 to 250 000 K'. In: *Solar Physics* 212.1 (Jan. 2003), pp. 81–97. DOI: 10.1023/A:1022900604972 (cit. on p. 15).

[LBS83] J. L. Leroy, V. Bommier and S. Sahal-Brechot. 'The magnetic field in the prominences of the polar crown'. In: *Solar Physics* 83.1 (Feb. 1983), pp. 135–142. DOI: 10.1007/bf00148248 (cit. on p. 30).

[Lun+14] Manuel Luna et al. 'Observations and Implications of Large-amplitude Longitudinal Oscillations in a Solar Filament'. In: *Astrophysics Journal* 785.1 (Mar. 2014), p. 79 (cit. on pp. 24, 25, 27, 29, 30, 32, 44, 64).

[Lun+18a] Manuel Luna et al. *GONG Catalog of Solar Filament Oscillations Near Solar Maximum*. 2018. URL: http://solar1.uib.es/index.php/luna_catalog/ (cit. on pp. 21, 22, 24).

[Lun+18b] Manuel Luna et al. 'GONG Catalog of Solar Filament Oscillations Near Solar Maximum'. In: *The Astrophysical Journal Supplement Series* 236.2 (May 2018), p. 35. DOI: 10.3847/1538-4365/aabde7 (cit. on pp. 21–25, 28, 32, 39, 45, 46, 73, 77).

[Mac+10] Duncan H. Mackay et al. 'Physics of Solar Prominences: II - Magnetic Structure and Dynamics'. In: *Space Science Reviews* 151.4 (Apr. 2010), p. 337. ISSN: 0038-6308, 1572-9672. DOI: 10.1007/s11214-010-9628-0. arXiv: 1001.1635. (Visited on 21/09/2021) (cit. on pp. 15, 16).

[Mar98] Sara F. Martin. In: *Solar Physics* 182.1 (1998), pp. 107–137. DOI: 10.1023/a:1005026814076 (cit. on p. 13).

[MR60] G. E. Moreton and H. E. Ramsey. 'Recent Observations of Dynamical Phenomena Associated with Solar Flares'. In: *Publications of the Astronomical Society of the Pacific* 72.428 (Oct. 1960), p. 357. DOI: 10.1086/127549 (cit. on p. 21).

[NAS22] NASA/SDO/Goddard. *SDO HMI Magnetogram*. 2022. URL: https://www.nasa.gov/content/goddard/sdo-hmi-magnetogram/ (cit. on p. 23).

[Oka+07] Takenori J. Okamoto et al. 'Coronal Transverse Magnetohydrodynamic Waves in a Solar Prominence'. In: *Science* 318.5856 (Dec. 2007), pp. 1577–1580. DOI: 10.1126/science.1145447. arXiv: 0801.1958 [astro-ph] (cit. on pp. 15, 16).

[Par14] Susanna Parenti. 'Solar Prominences: Observations'. In: *Living Reviews in Solar Physics* 11 (2014). DOI: 10.12942/lrsp-2014-1 (cit. on p. 15).

[PBR03] Alexei A. Pevtsov, K. S. Balasubramaniam and Joey W. Rogers. 'Chirality of Chromospheric Filaments'. In: *The Astrophysical Journal* 595.1 (Sept. 2003), pp. 500–505. DOI: 10.1086/377339 (cit. on p. 13).

[PE00] Hans Pécseli and OddbjØrn Engvold. 'Modeling of prominence threads in magnetic fields: Levitation by incompressible MHD waves'. In: *Solar Physics* 194.1 (May 2000), pp. 73–86. DOI: 10.1023/A:1005242609261 (cit. on p. 16).

[Pri14] Eric Priest. *Magnetohydrodynamics of the Sun*. Cambridge University Press, Apr. 2014. ISBN: 9781139020732. DOI: 10.1017/cbo9781139020732 (cit. on p. 16).

[Rim+20] Thomas R. Rimmele et al. 'The Daniel K. Inouye Solar Telescope — Observatory Overview'. In: *Solar Physics* 295.12 (Dec. 2020). DOI: 10.1007/s11207-020-01736-7 (cit. on p. 6).

[Sat+11] Ville Satopaa et al. 'Finding a "Kneedle" in a Haystack: Detecting Knee Points in System Behavior'. In: *2011 31st International Conference on Distributed Computing Systems Workshops*. IEEE, June 2011. DOI: 10.1109/icdcsw.2011.20. URL: https://github.com/arvkevi/kneed/ (cit. on p. 62).

[SIS06] Sami K. Solanki, Bernd Inhester and Manfred Schüssler. 'The solar magnetic field'. In: *Reports on Progress in Physics* 69.3 (Feb. 2006), pp. 563–668. DOI: 10.1088/0034-4885/69/3/r02 (cit. on pp. 9, 12).

[Sti02] Michael Stix. *The Sun: An Introduction*. Astronomy and Astrophysics Library. Springer Berlin Heidelberg, 2002. ISBN: 9783540207412. DOI: 10.1007/978-3-642-56042-2 (cit. on pp. 5, 7, 8, 31).

[Tan95] Einar Tandberg-Hanssen. *The Nature of Solar Prominences*. Springer Netherlands, 1995. DOI: 10.1007/978-94-017-3396-0 (cit. on p. 30).

[Tho53] Robert L. Thorndike. 'Who belongs in the family?' In: *Psychometrika* 18.4 (Dec. 1953), pp. 267–276. DOI: 10.1007/bf02289263 (cit. on p. 62).

[VE15] Jean-Claude Vial and Oddbjørn Engvold, eds. *Solar Prominences*. Springer International Publishing, 2015. ISBN: 978-3-319-10415-7. DOI: 10.1007/978-3-319-10416-4 (cit. on pp. 15, 22).

[Wan+16] Bing Wang et al. 'Dynamics of a Prominence – Horn Structure during its Evaporation in the Solar Corona'. In: *The Astrophysical Journal Letters* 827.2 (Aug. 2016), p. L33. DOI: 10.3847/2041-8205/827/2/l33 (cit. on p. 44).

[Zha+13] Q. M. Zhang et al. 'Parametric survey of longitudinal prominence oscillation simulations'. In: *Astronomy and Astrophysics* 554 (June 2013), A124. DOI: 10.1051/0004-6361/201220705 (cit. on p. 46).

[Zho+17] Yu-Hao Zhou et al. 'Solar Filament Longitudinal Oscillations along a Magnetic Field Tube with Two Dips'. In: *The Astrophysical Journal Letters* 839.1 (Apr. 2017), p. 9. DOI: 10.3847/1538-4357/aa67de (cit. on p. 44).

[Zur+21] Ernesto Zurbriggen et al. 'An MHD Study of Large-Amplitude Oscillations in Solar Filaments'. In: *Solar Physics* 296.12 (Nov. 2021). DOI: 10.1007/s11207-021-01908-z (cit. on p. 30).

Figure sources

[BBS07] BBSO. *Filaments and Prominences observed in Halpha*. 2007. URL: https://www.researchgate.net/figure/4-Filaments-and-Prominences-observed-in-Ha-by-BBSO_fig3_234502854 (cit. on p. 13).

[GON13] GONG H-alpha Network and the Swedish 1-metre Solar Telescope. *Filaments and Prominences observed in Hα*. 2013. URL: https://www.stce.be/news/219/welcome.html (cit. on p. 14).

[Hat21] David J. Hathaway. *The Solar Cycle*. 2021. URL: https://www.researchgate.net/figure/A-Magnetic-Butterfly-Diagram-constructed-from-the-longitudinally-averaged-radial-magnetic_fig10_234373682 (cit. on p. 11).

[Hig89] High Altitude Telescope. *A Coronal Mass Ejection*. 1989. URL: https://www2.hao.ucar.edu/education/pictorial/coronal-mass-ejection (cit. on p. 8).

[Lan10] Kenneth R. Lang. *Transition Region*. 2010. URL: https://ase.tufts.edu/cosmos/view_picture.asp?id=174 (cit. on p. 7).

[NAS09] NASA. *Daily Sunspot Area Averaged over Individual Solar Rotations*. 2009. URL: https://commons.wikimedia.org/wiki/File:Sunspot_butterfly_with_graph.gif (cit. on p. 10).

[NAS12] NASA/Goddard Space Flight Center. *HD Close up of March 6th X5.4 Flare*. 2012. URL: https://svs.gsfc.nasa.gov/10925 (cit. on p. 8).

[NAS19] NASA/Goddard Space Flight Center. *Magnetic field of sunspot (left) splits absorption line according to Zeeman effect (right)*. 1919. URL: https://commons.wikimedia.org/wiki/File:Sunzeeman1919.png (cit. on p. 12).

[Wik12] Wikimedia Commons. *Diagram of the Sun*. 2012. URL: https://en.wikipedia.org/wiki/File:Sun_poster.svg (cit. on p. 3).

[Wik16] Wikimedia Commons. *Proton-proton chain reaction*. 2016. URL: https://commons.wikimedia.org/wiki/File:Proton-proton_reaction_chain.svg (cit. on p. 3).